Modeling and design of integrated optical spectrometers (IOS)

Original Citation:
Modeling and design of integrated optical spectrometers (IOS) / Coppola, Carla Maria. - ELETTRONICO. - (2026).

Politecnico
di Bari

Department of Electrical and Information Engineering
ELECTRICAL AND INFORMATION ENGINEERING
Ph.D. Program
SSD: ING-INF/01 ELETTRONICA

Final Dissertation

MODELING AND DESIGN OF INTEGRATED OPTICAL SPECTROMETERS (IOS)

---

by
COPPOLA CARLA MARIA Carla Maria Coppola

Supervisors:
Prof. Vittorio M. N. Passaro
Prof. Francesco De Leonardis

Reviewers:
Prof. Andrea Melloni
Prof. Richard Soref

Coordinator of Ph.D. Program:
Prof. Mario Carpentieri
Mario Carpentieri

Course XXXVIII, 01/11/2022–31/10/2025

Politecnico
di Bari

Department of Electrical and Information Engineering
ELECTRICAL AND INFORMATION ENGINEERING
Ph.D. Program
SSD: ING-INF/01 ELETTRONICA

Final Dissertation

MODELING AND DESIGN OF INTEGRATED OPTICAL SPECTROMETERS (IOS)

---

by

COPPOLA CARLA MARIA

Supervisors:

Prof. Vittorio M. N. Passaro

Prof. Francesco De Leonardis

Reviewers:

Prof. Andrea Melloni

Prof. Richard Soref

Coordinator of Ph.D. Program:

Prof. Mario Carpentieri

Course XXXVIII, 01/11/2022–31/10/2025

Contents

Introduction

Important information concerning an object is carried by its spectrum: temperature, chemical composition, and relative speed with respect to the observer can be derived from an accurate analysis of the absorption and/or emission spectrum of a body. An optical spectrometer is an instrument used to investigate the wavelength-dependent properties of light; it resolves the frequency components of an optical signal by measuring the optical power associated with each spectral component.

The growing use of spectral analysis in everyday applications is pushing spectrometers to become smaller and more easily integrated into portable devices. The miniaturization process is not trivial and involves multiple challenges: on the one hand, one must identify the most suitable integration technology to achieve a compact, low-footprint device; on the other hand, the spectral resolution must be as high as possible to guarantee a meaningful analysis of a sample. The miniaturization of optical spectrometers is attracting the interest of the scientific community not only for academic, but also for commercial reasons. Indeed, the market for miniaturized spectrometers is expected to reach 900 million dollars [1]. The increasing demand for portable spectral analysis devices is pushing the miniaturization of these systems towards the centimetre and millimetre scale. The aim of realizing lab-on-chip devices or smartphone-based sensing solutions is driven by a wide range of applications, including environmental monitoring, biomedical diagnostics, food and beverage analysis, remote sensing, chemical analysis, astronomy, security, and defence.

The first review paper discussing miniaturized on-chip spectrometers dates back to 2004 [2]. In that work, Goldman et al. (1990) [3] is reported as the first miniaturized optical spectrometer for chemical analysis based on planar waveguides and grating couplers. Since then, many works have been published, advancing the field and enabling the development of new models, architectures, and technologies; this has led to the need to classify and categorize integrated spectrometers. Recently, detailed reviews have been published, focused on the description of basic working principles and integration technologies used to fabricate micro- and nano-spectrometers [4]–[6].

Resolving very closely spaced optical wavelengths often requires long optical paths, leading to a trade-off between size and resolution, thereby highlighting the challenge of miniaturizing high-performance spectrometers. Besides size and resolution, other important parameters must be optimized in the design of a high-performance integrated spectrometer, namely spectral range, bandwidth-to-resolution ratio, dynamic range, and measurement speed.

The motivation of this PhD research work has its roots in the challenges outlined above. The main objectives of this PhD research are:

- to analyze in detail the literature on integrated spectrometers published over the past two decades;
- to define metrics and identify the state-of-the-art technologies according to such metrics;
- to provide a reference database to enable a fair comparison among integrated spectrometer solutions;
- to propose and design alternative architectures that are competitive with previously published solutions;
- to experimentally characterize integrated spectrometers fabricated during the PhD research activities;
- to extend the modelling framework towards quantum-optics integrated spectrometers.

The thesis is organized as follows. In Chapter 1, the main metrics that describe a spectrometer are summarized, and an overview of the classification of miniaturized spectrometers according to their basic working principles is provided, together with a classification according to the adopted material platforms for on-chip spectrometers; an insight into the corresponding mathematical models is also reported.

In Chapter 2, the design of a digital integrated spectrometer based on the Vernier effect is described; the analytical equations describing the operating algorithm are derived, and the resulting scanning procedure is presented.

In Chapter 3, Fourier-transform spectrometers are described, and the case of a particular on-chip spectrometer is discussed. Based on this layout, three different samples have been fabricated. Results of the passive and active measurements taken at the University of Southampton are reported and detailed in this chapter.

In Chapter 4, a computational spectrometer based on two cascaded ring resonators is described. The reconstruction procedure is detailed, together with the algorithms and the typical methods adopted in inverse problems. Results of the reconstruction procedure are provided at the end of the chapter.

In Chapter 5, an on-chip single-photon spectrometer is discussed as a special case. A brief introduction to the relevant quantum-optics concepts and equations is provided at the beginning of the chapter to support the discussion.

Conclusions are drawn at the end.

The main achieved results can be summarized as follows:

- demonstration and numerical validation of a Vernier-based digital integrated spectrometer and its operating algorithm;
- experimental characterization of an on-chip Fourier-transform spectrometer, including passive components and phase-shifted Bragg gratings;
- development and validation of a reconstruction workflow for a computational spectrometer based on cascaded ring resonators;
- assessment of key design trade-offs (resolution, bandwidth, footprint, and measurement speed) for the considered architectures.

The main original contributions of this thesis are summarized below (a detailed discussion is provided in the Conclusions):

- design and simulation of a Vernier-based digital integrated spectrometer (Chapter 2);
- experimental measurements of output powers for passive components of a Fourier-transform spectrometer and measurements of the output powers of phase-shifted Bragg gratings (main functional components of the considered FTS) (Chapter 3);
- design, simulation, and reconstruction methodology for a computational spectrometer based on two cascaded ring resonators covered with phase-change material (Chapter 4).

In addition, this thesis includes a tutorial overview of the quantum-optics formalism required to model single-photon measurements in photonic integrated circuits, illustrated through a representative case study from the literature, as a basis for future developments (Chapter 5).

Related publications resulting from this PhD work include (a complete list is provided in the dedicated Publications chapter):

- **[P1]** Coppola, C. M., De Carlo, M., De Leonardis, F., and Passaro, V. M. N., "i-PHAOS: An Overview with an Open-Source Collaborative Database on Miniaturized Integrated Spectrometers," *Sensors*, 2024, 24(20):6715, doi: 10.3390/s24206715.
- **[P2]** Coppola, C. M., De Carlo, M., De Leonardis, F., and Passaro, V. M. N., "A new integrated optical spectrometer based on a Vernier-like configuration," *25th Anniversary International Conference on Transparent Optical Networks (ICTON)*, Barcelona, Spain, 2025, pp. 1–4, doi: 10.1109/ICTON67126.2025.11125160.
- **[P3]** Coppola, C. M., De Carlo, M., De Leonardis, F., and Passaro, V. M. N., "High-Resolution On-Chip Digitally Tunable Spectrometer Based on Double-Cascaded Ring Resonators," *Advanced Photonics Research*, 2025, 6:2500021, doi: 10.1002/adpr.202500021.

Chapter 1

Classification of spectrometers

1.1 Introduction

In this chapter we classify miniaturized on-chip spectrometers according to working principle and material platform. Important information concerning an object is carried by its spectrum; the temperature, as well as the chemical composition and the relative speed with respect to the observer can be derived from an accurate analysis of the absorption and/or emission spectrum of a body. An optical spectrometer is an instrument used to investigate the wavelength-dependent properties of light; it is able to solve the frequency components of light, measuring the intensity of power associated with each frequency component. The process of miniaturization is not trivial, and it involves multiple challenges. Indeed, on one hand, one should find the best integration technology to have a compact and low footprint device, on the other hand, the resolution should be as high as possible to guarantee a meaningful spectral analysis of a sample. The miniaturization of optical spectrometers is attracting the interest of the scientific community not only for academic, but also for commercial reasons. Indeed, the future market for miniaturized spectrometers is expected to reach 900 million dollars [1].

The increasing demand for portable spectral analysis devices is pushing the miniaturization of these devices towards the centimetre and millimetre scale. The aim of realizing lab-on-chip or smartphone-based sensing devices is driven by a wide range of applications including environmental monitoring, biomedical diagnostics, food and beverage analysis, remote sensing, chemical analysis, astronomy, security and defence. The first review paper discussing miniaturized on-chip spectrometers dates back to 2004 [2]. In that work, Goldman et al. [3] is reported as the first example of miniaturized optical spectrometer for chemical analysis based on planar waveguides and grating couplers. Since then, many works have been published, advancing the field and enabling the development of new models, architectures and technologies; this led to the need to classify and categorize integrated spectrometers. Recently, detailed reviews have then been published, focused on the description of the basic working principles and integration technologies used to fabricate micro- and nano-spectrometers [4]–[6].

The ability to resolve very close-by optical wavelengths often requires long optical paths, leading to a trade-off between size and resolution, thus explaining the challenge in the miniaturization of high-performance spectrometers. Apart from size and resolution, there are other important parameters to be optimized in the design of a high-performance integrated spectrometer, namely spectral range, bandwidth-to-resolution ratio, dynamic range and measuring speed. A plethora of data concerning the main metrics of integrated spectrometers can already be found in the scientific literature. However, a useful tool to collect and compare data has not yet been published. This work is motivated by the urge to organize and easily compare the values of the several relevant metrics in a referenced and updatable database. Together with the collected metrics, processing tools to analyze the data are also provided in terms of Python scripts that can be customized to get the desired plots. Thus, differently from previous published reviews on integrated spectrometers, this work contains a robust framework to allow for an easier comparison among metrics and features (like materials and technologies implemented), defining miniaturized spectrometers and photodetectors.

The chapter is organized as in the following. In the first Section, the main metrics that describe a spectrometer are summarized. In the second Section, an overview of the classification of miniaturized spectrometers according to their basic working principles is provided, while in the third Section, on-chip spectrometers are characterized according to the materials used to fabricate them. An insight on the mathematical models is also reported both in the second and third section. In the fourth Section, an open-source project is suggested, that collects a database including the fundamental metrics of integrated spectrometers and a Python script to analyze the database entries. The database will be available on GitHub and periodically updated by the community. Conclusions are drawn at the end.

1.2 Spectrometers: definitions and performance metrics

In order to classify and compare spectrometers, it is worth summarizing the main measurable physical quantities typically used to determine their performances and features. In the following they will be listed, grouped according to the physical measure they relate to and then briefly be described.
Spectral range: it represents how large is the window of detectable wavelengths; it is provided as the range between the maximum and minimum distinguishable wavelengths.
Target peak or central operating wavelength: It represents the central wavelength of the spectral range.
Spectral Resolution: it gives a measure of the ability to distinguish between close-by wavelengths; it is usually provided as the difference between the two nearest distinguishable input wavelengths.
Bandwidth-to-resolution ratio: it gives the number of distinguishable wavelength channels within the spectral range. It is strictly related to spectral range and spectral resolution.
Dynamic range: it represents the range of input power that can be distinguished by the spectrometer. It is usually given as the ratio between the maximum and minimum input power.
Footprint: it is an important measure of the area occupation of the spectrometer on the chip. Usually, the footprint of an integrated chip is proportional to the cost of the device fabrication.
Measuring speed: it provides a useful way to evaluate the total time required for a full reconstruction of the input spectrum. It can be also given as the maximum rate of spectrum acquisitions.

Together with the above-mentioned measurables, spectrometers can also be described according to other quantities, e.g. their scalability, i.e. the intrinsic possibility to miniaturize them, given their architecture and the fabrication technology. While the miniaturization process makes the field of possible applications of spectrometers wider, it compromises the spectral resolution and the bandwidth [7].

There are other parameters affecting the quality of a spectrometers and related to the photodetectors implemented in the spectrometer architecture. Specifically, these parameters are listed below.
External Quantum Efficiency EQE: it is defined as the ratio between the charge carriers (electrons or electron-hole pairs) generated by absorbing photons.
Internal Quantum Efficiency IQE η: it represents the ratio between the number of absorbed photons, nphoton, and emitted electrons (or recombined electron-hole pairs), n$_{carriers}$:

$$\eta = \frac{n_{photons}}{n_{carriers}}. \tag{1.1}$$

S **Responsivity R [AW^{-1}]:** it is a wavelength-dependent quantity, defined as the ratio between the output current, i_{output}, or voltage, V_{output}, produced and the input optical power:

$$R = \frac{i_{output}}{P_{input}}[AW^{-1}]. \tag{1.2}$$

As a function of the frequency, the responsivity can be expressed as:

$$R(f) = \frac{R(0)}{\sqrt{1+\left(\frac{f}{f_c}\right)^2}} \tag{1.3}$$

where f_c represents the so-called cut-off frequency, i.e. the frequency at which the response decreases as $1/e$, while $R(0)$ represents the responsivity for null frequency. **Noise Equivalent**

Power NEP [W Hz^{-1}]: it is defined as the input power per square root of the bandwidth resulting in a signal-to-noise ratio SNR = 1:

$$NEP = \frac{P_{min}}{\sqrt{\Delta f}} = \frac{N}{R}[WHz^{-1/2}] \tag{1.4}$$

Given a specific SNR, using the NEP, it is possible to evaluate the lowest input signal to obtain the desired SNR:

$$P_{min} = NEP\sqrt{\Delta f}SNR \tag{1.5}$$

Detectivity D = NEP^{-1}: it represents the inverse of the NEP; hence, the higher the detectivity, the better the photodetector:

$$D = \frac{1}{NEP}[W^{-1}Hz^{1/2}] \tag{1.6}$$

Specific Detectivity D* [Jones]: it is defined as the inverse of the NEP multiplied by the square root of the detection area A of the photodetector:

$$D^* = \frac{\sqrt{A}}{NEP}[\text{Jones}] \tag{1.7}$$

where 1 Jones = cm·Hz$^{1/2}$W^{-1} [8].
Risetime and falltime [s]: given an optical impulse or a square-pulse signal, they are defined as the time at which the produced photocurrent increases from 10% to 90% and from 90% to 10% of the maximum value achievable with constant illumination of the spectrometer, respectively.
-3 dB bandwidth f$_{-3dB}$: using the definition of responsivity, the -3 dB bandwidth f$_{-3dB}$ is defined as the frequency at which the output power, R^2, halved:

$$R^2(f_{-3dB}) = \frac{1}{2}R^2(0) \tag{1.8}$$

Full-width-half-maximum (FWHM): the wavelength range where the responsivity is higher than half of its maximum value. According to this parameter, a photodetector can be defined as narrowband or broadband. For a deeper analysis, it is suggested reading the book by Liu [9].

1.3 Mechanism-based classification of spectrometers

The main way to classify spectrometers considers their working principles; in this perspective, spectrometers can be classified as wavelength demultiplexing (WDM) and wavelength multiplexing (WM). In an alternative but equivalent way, they are respectively called split-channel and digital spectrometers.

1.3.1 Wavelength de-multiplexing spectrometers

They are based on the spatial separation of different wavelength components of light; this is the reason why they are also referred to as split channel spectrometers. Because the main components for this first kind of spectrometers are dispersive elements (mainly gratings) or filters, wavelength demultiplexing (WdM) spectrometers can be further classified as dispersive or filter-based ones. Integrated dispersive spectrometers are based on similar principles that are commonly implemented in non-miniaturized spectrometers, for example in the Czerny-Turner [10], or Fastie-Ebert [11], [12] configurations spectrometers. In WdM spectrometers different wavelength components of the input spectrum $S_{in}(\lambda)$ (hereafter λ represents the wavelength in vacuum) are spatially separated by the split channel optical components, and they are detected by N photodetectors. The detected current I_i at the i-th photodetector is related to the input spectrum $S_{in}(\lambda)$ via the i-th photodetector responsivity $R_i(\lambda)$ and the optical transmitted fraction, C_i, of the input spectrum to the i-th photodetector. I_i can then be expressed as:

$$I_i = \int R_i(\lambda)\, C_i(\lambda)\, S_{\text{in}}(\lambda)\, \mathrm{d}\lambda, \qquad i = 1, \ldots, N \tag{1.9}$$

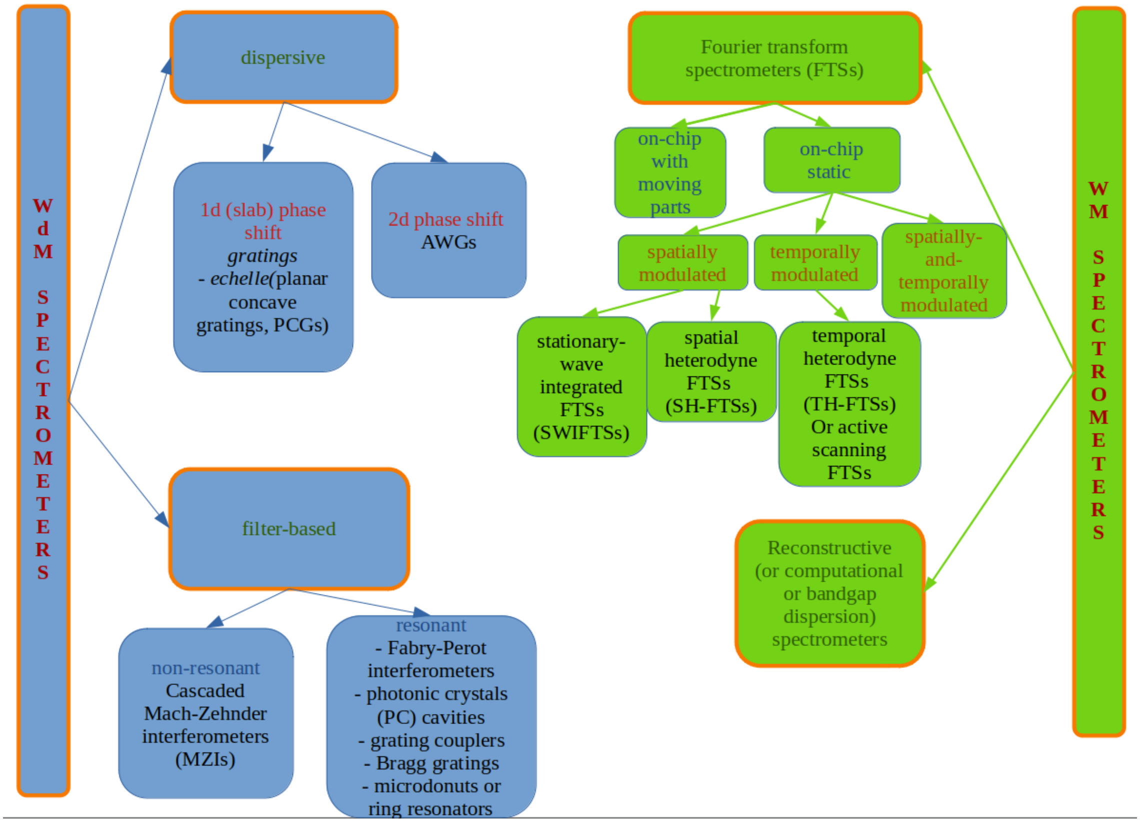

Figure 1.1: Classification of on-chip spectrometers according to their basic working principles.

over the bandwidth. It is worth noting that possible losses are accounted for in $R_i(\lambda)$. The full set of output currents can be arranged in an $N \times 1$ vector, I. In a split-channel spectrometer N corresponds to the bandwidth-to-resolution ratio. Moreover, in an ideal case, $C_i(\lambda)$ is proportional to a delta function centred to the i-th filtered wavelength.

Typical components of dispersive spectrometers are gratings, like the echelle gratings, the planar concave gratings and arrayed waveguided gratings (AWGs). In most of the cases, both before and after interacting with the grating, light freely propagates in slab regions called free propagation regions (FPRs); in the case of AWGs, such regions are named star couplers (see Figure 1.2). Gratings in integrated spectrometers can be both used in transmission and reflection.

The basic principle of dispersive spectrometers is the multi-path interference of light. The optical paths are designed to have different lengths such that light experiences different known phase shifts. The optical path differences are typically obtained by either confining light in one dimension using slab waveguides and diffracting it via gratings with specific geometries (as in the case of echelle gratings and planar concave gratings, PCGs), or by confining light in two dimensions using waveguides (e.g. strip or rib) with different lengths (as in the case of AWGs). For this reason, the first and second kinds of spectrometers can be labelled as 1D- (or slab) and 2D-phase shift driven spectrometers. In the echelle gratings light is diffracted via saw-like grooves, that might be placed following the circumference of the so-called Rowland circle. This geometrical figure has been suggested by Henry A. Rowland in 1883 [13] as an improvement in the shape of gratings used in optics. The advantages of concave gratings mainly rely in their better light focusing and in the reduction of aberration effects [14]. Rowland circles are also used in designing the free propagation regions of AWGs.

It is worth noting that, in the case of 1D-phase shift driven spectrometers, the region of the slab where light propagates from the input to the grating is also used for light to reach the output photodetectors. This aspect can suggest an optimized way of using the available space on the chip compared to the case of e.g. AWGs. However, reflection-type AWGs have been suggested to use the same free propagation region both for the input and output of light [15]. Moreover, the freedom in organizing the architecture of the device enables additional flexibility in the layout design of AWG-based on-chip spectrometers.

In [16], SOI AWGs and PCGs have been demonstrated to perform better for high- and low-resolution applications, respectively.

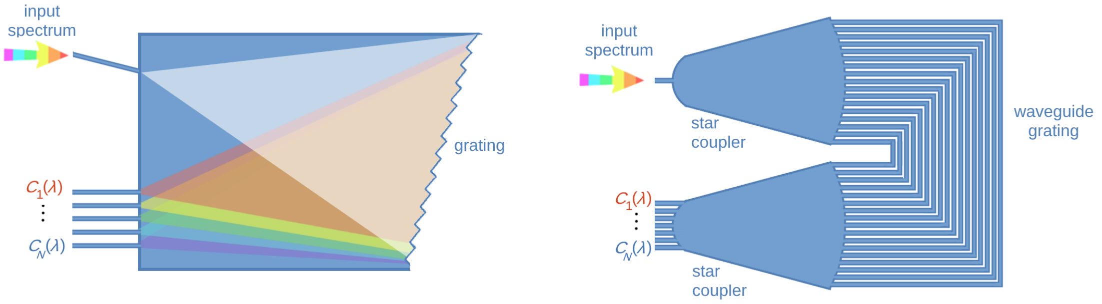

Figure 1.2: Schematic diagrams describing demultiplexing dispersive spectrometers. (a) Grating (b) Array-waveguide grating.

The class of filter-based units in wavelength demultiplexing spectrometers is characterized by the usage of non-resonant filters such as cascaded Mach-Zehnder interferometers and resonant filters, like Fabry-Perot interferometers, photonic crystal (PhC) cavities, Bragg gratings and microdonut or ring resonators. Non-resonant filters are also referred to as finite-impulse response (FIRs) filters. The working principle of these spectrometers is suggested by their name. Indeed, different optical filters separate the wavelength components of the input light. Such filters are designed to be as selective as possible in the wavelength domain. For this reason, they are labelled as narrowband filters. Differently from dispersive gratings that only implement a spatial separation of the light components, narrowband filters can both work through spatially or temporally separate light. The spatial separation is typically achieved in arrayed narrowband filters, while tunable narrowband spectrometers implement a temporal separation (see Figure 1.3).

A review on silicon-based optical micro spectrometers implementing Fabry-Perot filters has been presented in [17]. Emadi et al. [18] showed the design and fabrication of a high-resolution micro spectrometer based on a Fabry-Perot filter with linearly variable distance between the dielectric mirrors, integrated with a detector array. The resolution of the spectrometer goes from 2.2 nm in the broadband design down to 0.7 nm in the narrowband configuration (spectral ranges 570 nm - 740 nm and 610 nm - 680 nm, respectively).

PhC cavities can be used as wavelength filters because of their intrinsic periodic structure, as for the case of Bragg gratings. Spectrometers based on PhC cavities could either be constituted by an array of tuned cavities or by a single dynamically tunable cavity. Liapis et al. [19] fabricated a high quality factor single tunable PhC cavity in SOI technology. Its resolution is reported to be 0.02 nm around 1550 nm. Sharma et al. [20] developed a spectrometer based on TiO_2 and SiO_2 alternating-stacked layers. These materials have been chosen because of their low absorption and high refractive index contrast, that in principle makes it possible to have a spectral range in the visible region (400 nm-700 nm).

Concerning integrated micro spectrometers employing ring resonators or microdonut resonators as wavelength filters, in 2016 Zheng et al. [21] suggested a high-resolution spectrometer with a tunable micro-ring resonator filter, with 19 nm spectral range and 0.15 nm resolution. Eventually, Zheng et al. [22] proposed a remarkable architecture combining ring resonators and AWGs, where a 25.4 nm spectral range and a 0.1 nm resolution were achieved in an extremely reduced footprint compared to devices that purely implement only AWGs. Recently, Chen et al. [23] have suggested a spectrometer based on a micro-ring resonator array, having a very compact footprint, an operating spectral range greater than 12 nm and a spectral resolution of 0.17 nm.

As in Zheng et al. [22], it is also possible to find mixed approaches that include both dispersive and filter-based optical components in the same prototyped miniaturized spectrometer. For example, in [24] a biochemical sensing spectrometer implementing both a cascaded microring resonator and an AWG was shown, with a high spectral resolution of 0.42 nm and spectral range of 90 nm. In 2022, Zhang et al. [25] proposed an integrated spectrometer based on a tunable micro-ring resonator and an AWG, with a 70 nm optical spectral range and 0.2 nm resolution. In other designs, several filters of different kind have been used in the same on-chip spectrometer. For example, Horie et al. [26] adopted a Fabry-Perot filter together with Bragg reflectors while Alshamrani et al. [27] used an add-drop ring resonator as a narrowband filter, combined with a distributed Bragg reflector as a broadband filter.

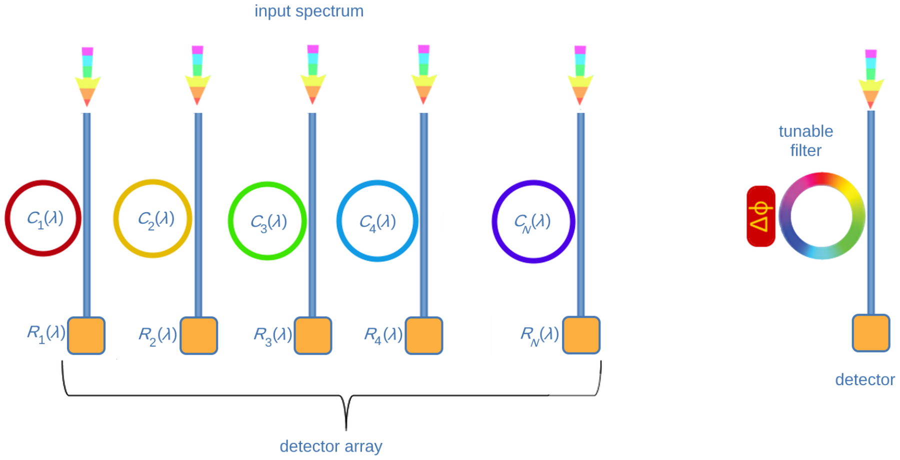

Figure 1.3: Schematic diagrams describing demultiplexing filters-based spectrometers. (a) Arrayed narrowband filters. (b) Tunable narrowband filters spectrometer.

The bandwidth-to-resolution ratio of arrayed-filters spectrometers corresponds to the number of the adopted filters, while the resolution is limited by the transmission function of each filter.

A description of the differences among the performance metrics of dispersive (AWGs, PCGs) and filter-based (Mach-Zehnder filters) components developed in SOI technology that can be used to realize spectrometers can be found in [28].

1.3.2 Wavelength multiplexing spectrometers

As suggested by their name, the wavelength multiplexing spectrometers are based on the principle of wavelength multiplexing. They can be divided into Fourier-transform spectrometers (FTSs) and reconstructive spectrometers (or computational spectrometers, CSs, or bandgap dispersion spectrometers), typically implementing Fourier-transform interferometers and sets of distinct tuneable broadband filters, respectively.

1.3.2.1 Fourier-transform spectrometers (FTSs)

FTSs are based on interference of light. Their main advantages are a large optical throughput and a high signal-to-noise ratio, which allow them to be suitable in detecting even faint signals in dark conditions. The architecture of the FTSs consists of a series of interferometers; the output signal power at the detector is [29]:

$$P_{out}(l) = \frac{1}{2}\int_0^\infty S(\nu)[1+\cos(2\pi\nu l)d\nu] \tag{1.10}$$

where ν is the wavenumber in vacuum of the input light and l is the optical path difference between the interferometer arms. By defining $\bar{P}_{out}(l) = 2P_{out}(l) - P_{out}(0)$ (that is called interferogram) and using the Fourier theorem, $\bar{P}_{out}(l)$ and $S(\nu)$ are related as:

$$\bar{P}_{out}(l) = \int_0^\infty S(\nu)[\cos(2\pi\nu l)d\nu] \Longleftrightarrow S(\nu) = \int_0^\infty \bar{P}_{out}(l)[\cos(2\pi\nu l)dl] \tag{1.11}$$

In practice, the integration to be performed to obtain the input spectrum is done up to a maximum value of optical path difference l_0. So, the input spectrum can be approximated as:

$$S(\nu) \approx \bar{S}(\nu) = \int_0^{l_0} \bar{P}_{out}(l)\cos(2\pi\nu l)dl \tag{1.12}$$

The expression for $S(\nu)$ can be rewritten as:

$$S(\nu) = \frac{1}{2}\int_{-\infty}^{+\infty} \bar{P}_{out}(l)\exp(-2\pi i\nu l)dl \tag{1.13}$$

by using Euler identity $\exp^{-2\pi i\nu l} = \cos(2\pi\nu l) - i\sin(2\pi\nu l)$ and using simmetry properties of $\bar{P}_{out}$ that is even respect to the independent variable l[1]. Hence, $S(\nu)$ can also be approximated as:

$$S(\nu) \approx \bar{S}(\nu) = \frac{1}{2}\int_{-l_0}^{l_0} \bar{P}_{out}(l)\exp\left(-2\pi i\nu l\right)dl \tag{1.14}$$

Limiting the integration domain corresponds to multiplying by a box-car function (equal to 1 between $S(\nu)$ and $\mathrm{sinc}(l_0\nu)$. According to the Rayleigh criterion, the resolution is thus obtained as:

$$\delta\nu = \frac{1}{l_0} \tag{1.15}$$

Consequently, the input spectrum can be approximated at a discrete finite number of wavenumbers (between ν_0 and ν_K). Moreover, experimentally the interferograms are collected at discrete and finite values of optical path differences equal or lower than l_0, so the interferogram can be written as:

$$\bar{P}_{out}(l_n) = \sum_{k=0}^{K} \bar{S}(\nu_k)[\cos\left(2\pi\nu_k l_n\right)], \qquad \text{for } n = 0, ..., N \tag{1.16}$$

Eq. 1.16 can be solved with different numeric methods (i.e. minimum least squares), in order to obtain $\bar{S}_{\nu_k}$.

There are several advantages related to FTSs if compared to a wavelength demultiplexing spectrometer. These advantages are usually named after the scientists that underlined them, namely Peter Berners Fellgett, Pierre Jacquinot and Janine Connes. Fellgett's advantage concerns the possibility to retrieve information from all wavelengths at once: because the scanning time is reduced, this also implies a higher signal-to- noise ratio [30]. Jacquinot's advantage is also called the throughput advantage, and it is related to the fact that FTSs possess a larger input area compared to the linear apertures usually adopted in dispersive spectrometers, thus allowing for a higher throughput of incident light. Connes's advantage [31] is connected to FTSs higher wavelength accuracy. FTSs can be subcategorized into on-chip static spectrometers and on-chip spectrometers with moving parts. An interesting review on miniaturized FTSs has been recently published [32]. Considering only the static spectrometers, it is possible to have FTSs that are spatially, temporally or spatially-and-temporally modulated. In the first group it is possible to mention the stationary-wave integrated FTSs (SWIFTSs) and the spatial heterodyne FTSs (SH-FTSs). SWIFTSs can be built using two different arrangements, called the Lippmann and the Gabor (or counter-propagative) configurations, respectively. They are named after Gabriel Lippmann and Dennis Gabor, both awarded with Nobel Prize in Physics. In both configurations, nanodetectors are periodically placed on the waveguides in order to feel the evanescent field of the waveguides themselves. The Lippmann configuration consists in the injection of light in a waveguide where a mirror is placed at the end, while the Gabor configuration corresponds to the case in which there is light input from both the extremities of the waveguide; in the latter case, light is injected into the waveguide extremities via a Y-junction. When a monochromatic light enters in the SWIFTSs, both in the Lippmann and in the Gabor configurations, stationary waves are formed along the waveguides. However, if white light is injected, different interference patterns will appear. Specifically, in the case of the Lippmann configuration, the so-called Lippmann interferogram is created, characterized by the presence of the black central fringe at the mirror interface and resulting from the superposition of the several stationary waves. In the case of the Gabor configuration, the waves interfere in counter-propagating way, thus producing a Fourier interferogram with the black fringe at the centre of the device when the difference in their phase is null. In the Gabor configuration it is then possible to have information both on the spectrum and on the phase of the interfering electromagnetic waves (Figure 1.4, see also [33], [34]). The first integrated implementation of a SWIFTS has been reported by Cavalier et al. 2011 [35], where superconducting nanowires are used as single photon detectors along a SiN waveguide. An integrated implementation of this configuration can be found in [36], where the interferograms are under-sampled in the interference region with golden nanorods and obtained by changing the phase of the input light signals using electro-optical modulation. Temporally modulated spectrometers are also called temporal

---

[1] In the case of ideal reciprocal interferometer, the detected interferogram $\bar{P}_{out}(l)$ is a real-valued quantity being the measured power and it is even with respect to the optical path difference l, since it depends on $\cos(2\pi\nu l)$. In the presence of wavelength-dependent phase errors $\phi(\nu)$ (e.g. in the case of dispersion or misalignment in the interferometer), the interferogram may deviate from perfect even symmetry. In these cases, an odd component is introduced in the function hence requiring a phase correction

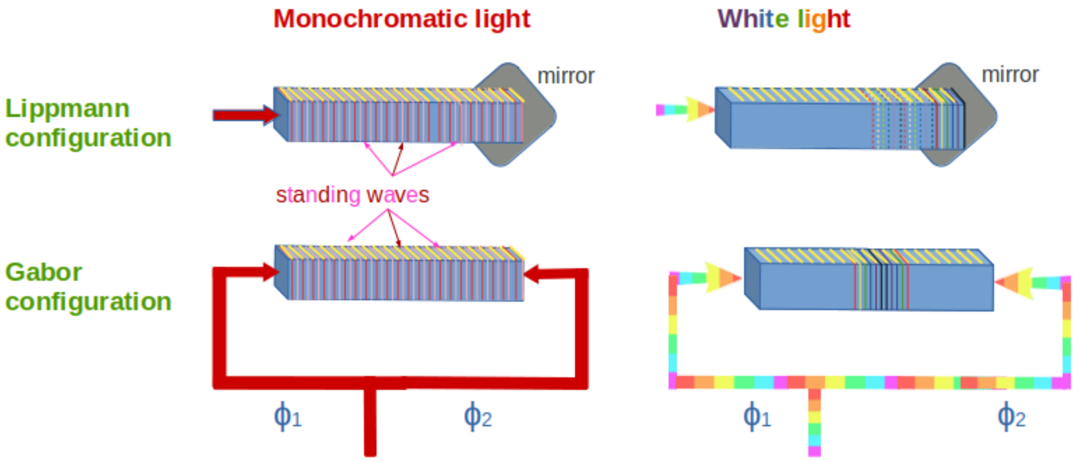

Figure 1.4: Schematic diagrams describing multiplexing/spatial heterodyne FTSs. Top part: Lippmann configuration i.e. the light enters in the waveguide and is reflected by a mirror; in the case of monochromatic light, a standing wave forms, while in the case of white input light an interference figure appears close to the mirror, showing a black fringe at that side. Bottom part: Gabor configuration i.e. the light enters in the waveguide from both sides; if monochromatic, standing wave forms, otherwise the interference figure shows up along the waveguide. The interferogram is centred if the phases of the interfering waves are the same.

heterodyne FTSs (TH-FTSs) or active scanning FTSs because of the presence of both passive and active parts on the photonic integrated circuit (hereafter PIC). The active part is performed by means of the thermo-optical or electro-optical effect. In TH-FTSs, the interferogram is obtained as an ensemble of output power collected at different time, corresponding to different applied phase shifts. In Figure 1.5 an example of SH-FTSs is reported, where the differences in the optical paths are achieved using unbalanced Mach-Zehnder interferometers (MZIs). SH-FTSs typically employ arrays of unbalanced Mach-Zehnder interferometers with linearly increasing differences in the optical path differences. In Heidari et al. 2019, an example is provided using the silicon-on-sapphire technology [37]. In this configuration, the interferogram is obtained as the collection at the output at spatially displaced photodetectors.

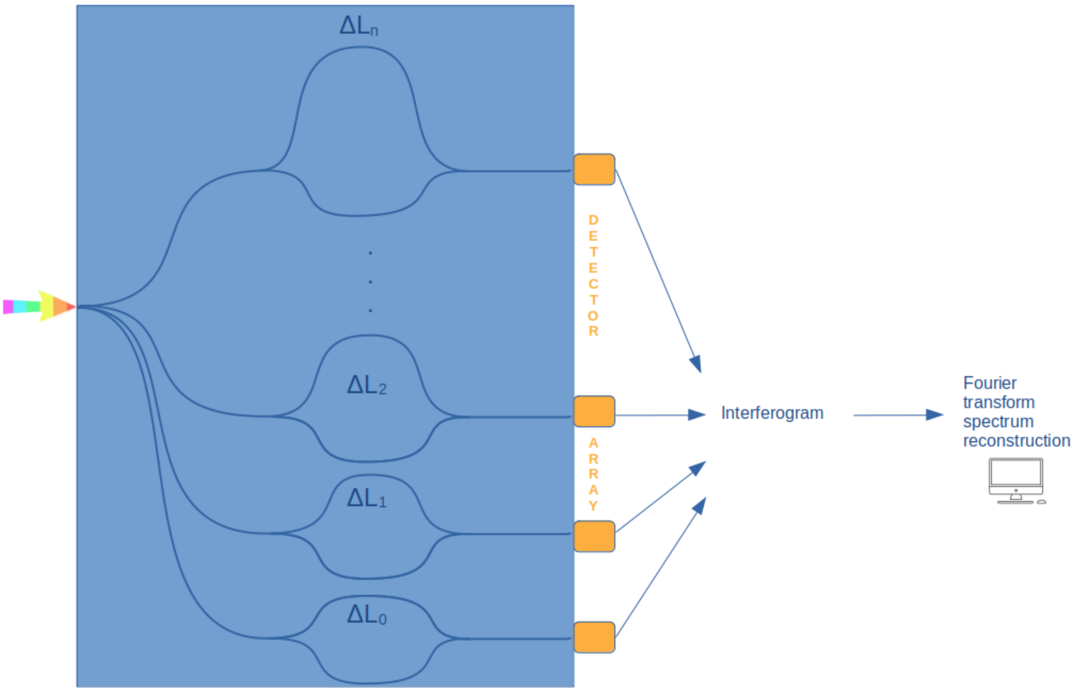

Figure 1.5: Schematic diagram describing multiplexing spatial-heterodyne Fourier-transform spectrometers (SH-TFSs).

In Figure1.6 a schematic example of the working principle of a TH-FTS is reported. Typically, the phase change $\Delta\Phi$ can be achieved either via the thermo-optic or the electro-optic effect. In Zheng et al. 2019 [38] an example of a spatially-and-temporally modulated FTS is reported; such an alternative FTS is obtained by cascading a tunable micro-ring resonator with a tunable Mach–Zehnder interferometer. More recently, Xu et al. 2024 [39] demonstrated an integrated spectrometer with a resolution of 250 pm over a 200 nm bandwidth with a configuration implementing both spatial and temporal modulation, referred to as a 2D Fourier-transform spectrometer. Li et al., 2024 [40] suggested an inversely designed integrated spectrometer in which the spectrometer can work under two different regimes and it is based on a programmable photonic circuit.

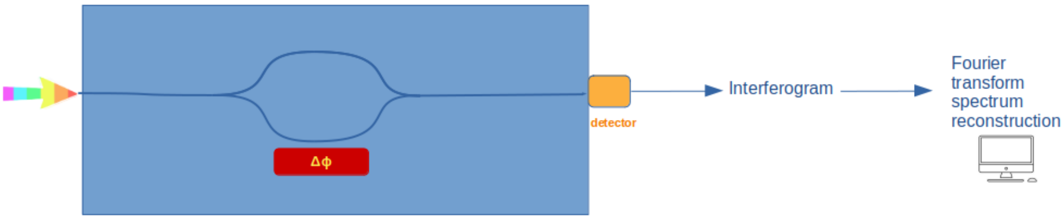

Figure 1.6: Schematic diagram describing multiplexing temporal heterodyne Fourier-transform spectrometers (TH-FTSs) or active spectrometer.

1.3.2.2 Frequency-comb-enabled integrated spectroscopy

As a Fourier-transform-like technique, chip-scale dual-comb spectroscopy maps two optical frequency combs into a radio-frequency photocurrent via multi-heterodyne detection. An optical frequency comb is a light source whose optical spectrum consists of a set of narrow, phase-coherent lines ("teeth") equally spaced in frequency. The frequency of the n-th comb line can be written as

$$f_n = f_0 + n\Lambda, \tag{1.17}$$

being Λ the repetition rate (i.e. the line spacing between the teeth) and f_0 the so-called carrier-envelope offset frequency. Optical combs can be produced in several ways (e.g. mode-locked lasers, electro-optic modulation, or microresonator-based Kerr nonlinearities (microcombs)).

Optical frequency combs have enabled high-precision and broadband spectroscopic techniques. In integrated photonics, microresonator-based combs (microcombs) and integrated dual-comb sources have recently enabled chip-scale dual-comb spectroscopy (DCS). In such devices, two combs with slightly different repetition rates $\Lambda_2 = \Lambda_1 + \Delta\Lambda$ connect optical spectra with a radio-frequency (RF) electric signal (see Fig.1.7 for a graphical representation). In this context, the RF photocurrent is usually referred to as radio-frequency beat notes; they are approximately located at

$$f_{\mathrm{beat},n} \approx \Delta f_0 + n\,\Delta\Lambda. \tag{1.18}$$

This description is pretty close to Fourier-transform spectroscopy but without moving parts [41]–[43].

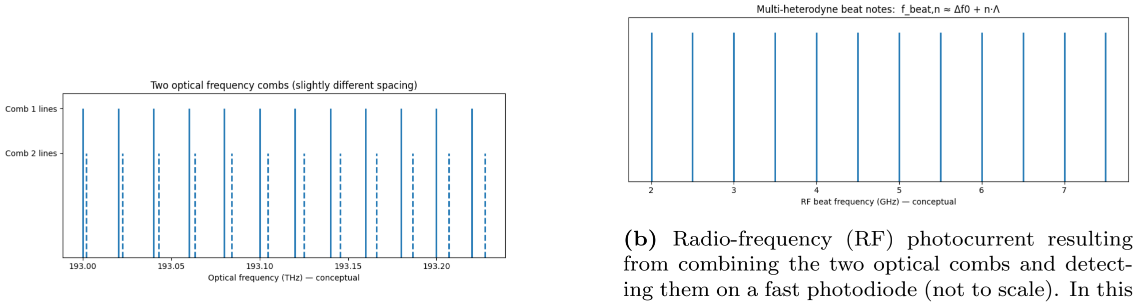

(a) Two optical frequency combs with slightly different repetition rates.

(b) Radio-frequency (RF) photocurrent resulting from combining the two optical combs and detecting them on a fast photodiode (not to scale). In this context, the RF tones are usually referred to as *beat notes*.

Figure 1.7: Graphical representation of the working principle of dual-comb spectroscopy.

1.3.2.3 Reconstructive spectrometers (or computational spectrometers) RSs

Reconstructive spectrometers are special kinds of spectrometers in which the input spectrum is acquired at all wavelengths at once and it is reconstructed by means of postprocessing algorithms applied to the output optical powers collected by a photodetector matrix. In particular, they are designed such that the input light interacts with special optical components, designed such that their response functions ensure the orthogonality among output vectors.

The reconstruction procedure is based on the theoretically demonstrated finding by Wang and Yu in 2014 [44] that random spectral filters can help in gaining high spectral resolution. This can be achieved together with using advanced signal processing methods, e.g. compressive sensing or others (see e.g. [7], [45]–[48] for a detailed description). Based on this finding, the first experimental computational spectrometer has been shown in the seminal work by Bao and Bawendi [49]. Successive works have been performed by [50], [51] and [52]. RSs can also be called bandgap dispersion spectrometers because the typical basic elements in the optical detection are photonic crystal slabs or nano-structured semiconductors. In general, broadband filters are implemented in RCs as detecting units that separate light components. As in the case of narrowband filters, broadband filters can be also arranged as array or in a tunable configuration (Figure 1.8).

Given an unknown input spectrum $S(\lambda)$ and N photodetectors, it is possible to express the measured photocurrent I_i at each ith photodetector as:

$$I_i = \int R_i F_i(\lambda) S(\lambda) d\lambda \equiv \int D_i(\lambda) S(\lambda) d\lambda, \qquad i = 1, ..., N \tag{1.19}$$

where $R_i(\lambda)$ is the responsivity of the i-th photodetector and $F_i(\lambda)$ corresponds to the transmission function of the adopted broadband filter. For convenience, we define their product as $D_i(\lambda)$. Discretizing Eq. 1.19, the outputs of the photodetectors can then be arranged as a $N \times 1$ vector:

$$I = D \cdot S \tag{1.20}$$

where I is an $N \times 1$ vector, D is an $N \times P$ matrix and S is a $P \times 1$ vector, being P the number of discretized wavelengths. The transmission spectral response matrix D is obtained via calibration procedures. Typically, a calibration laser source is scanned over a certain wavelength range and the output intensity I is recorded. The transmission matrix D relates the spectral domain to the spatial domain in a not-trivial one-to- one way, as it occurs in the case of classical split channel spectrometers. In reconstructive spectrometers, each row of the matrix D contains information on the transmission spectrum at different wavelengths. Eventually, it is possible to recover the unknown spectrum by inverting the transmission matrix in Eq. 1.20:

$$S = D^{-1} \cdot I \tag{1.21}$$

The matrix inversion is a numerically unstable procedure because of the intrinsic fluctuation connected to the noise [53]. For this reason, it is usually performed together with a non-linear optimization procedure. The most commonly used reconstruction algorithm is based on the so-called l1 norm optimization, in the convex or non-convex version, while other algorithms have been suggested, as the greedy algorithm and Bayesian method. The main reference papers for these algorithms have been published during the first decade of 2000s. A comparison between several compressive sampling strategies for integrated spectrometers can in found in [54]. In [55] an interesting framework to compare different compressive algorithms can be found. This open-source project aims in providing a standardized tool to develop and perform image compressive sensing. The updated git repository can be found at the link `https://github.com/PSCLab-ASU/OpenICS`. This approach can be applied even in the case N<<P, i.e. when the number of broadband filters is smaller than the discretization dimension of the input spectrum. Such a condition corresponds to undetermined linear systems often prone to be ill-conditioned [54]. To prevent ill-conditioning effects on the spectrum reconstruction, the resolution of Equation 1.21 can be performed using reconstructive procedures that implement regularization algorithms. Together with the usage of such algorithms, reconstructive spectroscopy can proceed by using compressed sensing. Compressed algorithms for signal processing are based on the idea to measure a spectrum using a limited number of measurements and to reconstruct it via reconstruction algorithms by using a compressed version of such measurements [56]. Among the suggested reconstructive algorithms, neural networks have also been adopted [57]. Several approaches have been developed as reconstruction techniques, namely the so-called speckle- spectroscopy, the filter-array reconstruction spectroscopy and the stochastic optical reconstruction spectroscopy (STORS) technique [48]. RSs have been fabricated by using multimode optical fibers [58], colloidal quantum dots [49], structurally engineered silicon nanowires [59], a single-nanowire [60], black-phosphorus [61], single-dot perovskite [62], a superconductive nanowire [63]. It is worth noting that spectrometers like the ones described in [62]–[65] could be considered as a subset of RSs in which the spectrometer is externally biased N times in order to fill the responsivity matrix $R_i(\lambda)$ and the spectrum is detected at each bias by a single photodetector (rather than having N distinct photodetectors acquiring the input spectrum filtered by N broadband filters). Oliver et al. [66], [67] showed that it is possible to work both on the reconstructive algorithms and the transmittances in order to improve the resolution of the spectrometer, in particular the resolution of spectrometers increases with hyper-random transmittances. In 2021 Sharma et al. [20] have developed a photonic crystal-based reconstructive spectrometer with alternating layers of TiO_2 and SiO_2. It has been recently suggested [68], [69] to use photonic molecules (specifically, in [68], four microdisk photonic atoms are adopted) in order to spectrally discriminate light. The spectral resolution is demonstrated to be ∼8 pm, though keeping the footprint very small ($70\times50\ \mu m^2$). This approach paves the way for further miniaturization scales. The application of reconfigurable photonics has been recently adopted to produce a broadband high resolution (pm) integrated spectrometer, that uses the reconstructive approach to derive the output spectrum [70], [71]. An exotic spectrometer has been suggested by Kwak et al. [72] that exploits the optical features of the mother-of-pearl. A recent review on RCs has been published [73]. A comparison of cons and pros for each kind of spectrometer have been summarized in Table 1.1.

1.4 Spectrometers classification based on material type: inorganic, organic and metamaterials

It is useful to classify miniaturized (micro- and nano-) spectrometers and their photodetecting optical components according to the materials that are adopted to fabricate them. Indeed, an insight of the chemical compounds suggests their efficiencies and their potential usages in specific applications. Moreover, the analysis of the materials is beneficial to understand the basic working

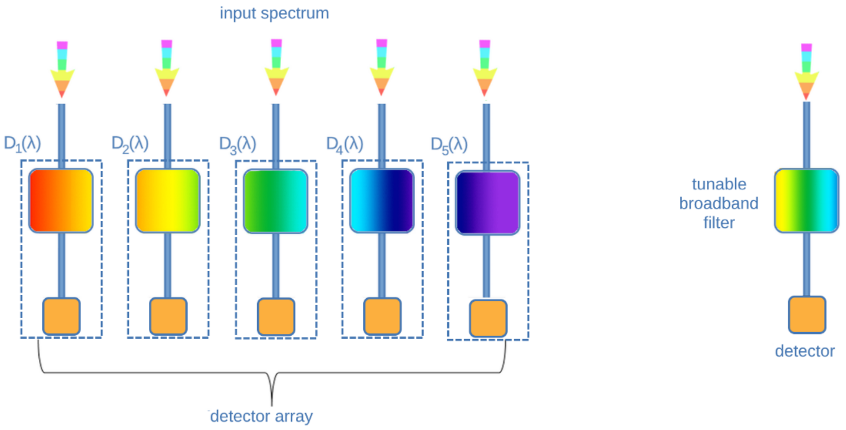

Figure 1.8: Schematic diagrams describing multiplexing broadband filter-based spectrometers (reconstructive or computational spectrometers). (a) Arrayed broadband filters; (b) Tunable broadband filters spectrometer.

principles and, as a consequence, the optimal architecture to be adopted. It is possible to group the spectrometers into inorganic material- and organic material-based devices. Together with these categories, it is worth to add a third class, represented by metamaterial-based miniaturised spectrometers. In the first two classes, the main photodetective materials are semiconductors.

1.4.1 Inorganic material-based spectrometers

The conventional semiconductor used to fabricate integrated spectrometers is silicon, the second more abundant chemical species on Earth. Among other reasons, the usage of silicon for integrated optical circuits is promoted for the full compatibility with mature CMOS technologies. There are several technologies in PICs that implement silicon, namely SOI (an acronym that stands for silicon-on-insulator) and silica-on-silicon. The high refractive index contrast of silicon (n_{Si} = 3.476) and its oxide SiO_2 ($n_{SiO_2} = 1.444$) at $\lambda = 1550$ nm is relatively high, hence the light can be waveguided with very small cross-sections and reduced bend radii. As a consequence, the footprint associated with such devices is small. Spectrometers fabricated using Silicon-based technologies can be found in several papers [27], [28], [74]–[80]. Another IV group semiconductor element that is used in spectrometers is germanium (Ge) [80], whose corresponding technology for integrated circuits is named GOS (germanium- on-silicon). For GOS platform, the contrast index is even higher that the SOI technology, being the refractive index of germanium $n_{Ge} = 4.2162$ for $\lambda =$ 1550 nm (the highest refractive index in the case of this element is found for infrared radiation). In integrated spectrometers Si and Ge can be used both for optical passive components and for photodetectors, according to the absorption of the chosen material in a certain operational wavelength region. Specifically, the transparency windows of Silicon and Germanium are approximately [1.9 - 12] μm and [1.2 - 7] μm, respectively, hence in these regions they can be used to realize passive optical components. Instead in the absorption wavelength regions, they can be adopted to realize photodetectors (although the absorption is limited by them being both indirect semiconductors). It is possible to have composite semiconductors, using elements from the III-V, II-VI, and IV-IV groups. Additional binary semiconductors that are used in photonic devices and give the name to the corresponding technologies for optical devices platforms are indium phosphide (InP) and silicon nitride (Si_3N_4). III-V group semiconductors have direct energy gaps: this feature leads to high absorption probabilities and tunable energy gaps, hence broader spectral ranges and higher sensitivities. Moreover, these platforms can be heterogeneously integrated on chip, as well as monolithically, to have both light sources and photodetectors on the same chip. III-V group materials can be used as gain materials for lasers and LEDs. This aspect makes them appealing in order to achieve lower dimensions and highly dense integrated spectrometers [81]. SiN devices are also compatible with CMOS technologies, and they have the additional advantages of having very low propagation loss and broadband spectral range, practically not influenced by thermal variations. Several spectrometers have been recently suggested using Si_3N_4 [82]–[85]. Previously, Nie et al. [86] reported the development of a Fourier-transform spectrometer integrated on silicon nitride platform with an extremely small footprint (0.1 mm^2) and 6 nm resolution. Several materials have been used to fabricate PCGs and AWGs, such as silica-on-silicon, SOI (silicon-on-insulator), GOS (germanium-on-silicon) and Si_3N_4 (silicon nitride) integration technologies [87]. It is worth introducing and distinguishing the concepts of hybrid and heterogeneous integration that can be used to realize PICs. The former refers to the integration process according to which different photonic integrated chips are bonded together to form a single device. Typically, in hybrid integration the starting chips are made of different materials and/or they have been fabricated using different technologies. Heterogeneous integration, on the contrary, concerns the integration process with which different materials and/or technologies are integrated on the same photonic chip. This integration option has major advantages like being very similar to monolithic integration, having lower fabrication costs than hybrid circuits and allowing for an easier alignment of the optical elements. Because of this last advantage, optical power losses are moderate at the interface between waveguides, although implemented using heterogeneous technologies. An interesting description of the experimental methods used to perform both hybrid and heterogeneous integration in optical devices can be found in [88]. Heterogeneous integration approaches have been adopted in fabricating integrated optical spectrometers [89]–[91].

1.4.2 Organic material-based spectrometers

Nowadays, in order to overcome the high fabrication costs of inorganic semiconductors, organic compounds are suggested as a feasible and interesting alternative. In fact, the usage of some polymers in order to create a planar grating spectrograph dates to several decades ago [92], where Polymethylmethacrylate (PMMA) was adopted in order to create the dispersive structure of an infrared spectrometer. More recently, research has been conducted in the field of polymer based organic photodetectors (OPDs). Narrowband OPDs can be easily implemented to fabricate an integrated filter-based spectrometer. OPDs standard design consists in a heterojunction containing compounds that behave as electron-acceptor and some other blend behaving as electron-donor. For this behaviour, acceptors and donors resemble the inorganic n- and p-type semiconductors, respectively, hence the name of organic semiconductors (OSs). It is possible to either deposit a donor layer followed by an acceptor layer (in this case a planar bilayer heterojunction is created) or acceptors and donors can be blended together to form bulk heterojunctions (BHJs) (Figure 8). The region where acceptor and donor are placed represent the photo-active part, typically tens-nm thick. As in the case of inorganic semiconductors, such region is put in between the electrodes. In this case, the absorption of the photons occurs through one of the electrodes that is semi-transparent (for example, based on indium tin oxide - ITO). In organic semiconductor materials, the absorption of photons induces the formation of a quasi-particle called exciton. When an exciton dissociates, free charge carriers are generated; contributing in principle to the photocurrent when they can reach the electrodes. However, the mobility of these charge carriers is limited compared to the inorganic counterparts (up to four orders of magnitude lower) due to the different interaction between electrons and periodic potentials, the presence of impurities or defects in the crystals, amorphous or crystalline nature of the compounds. The colour discrimination in such devices can be mainly achieved either using special kind of effects that can be exploited in organic compounds or via specific design of the architecture of the spectrometer itself. For

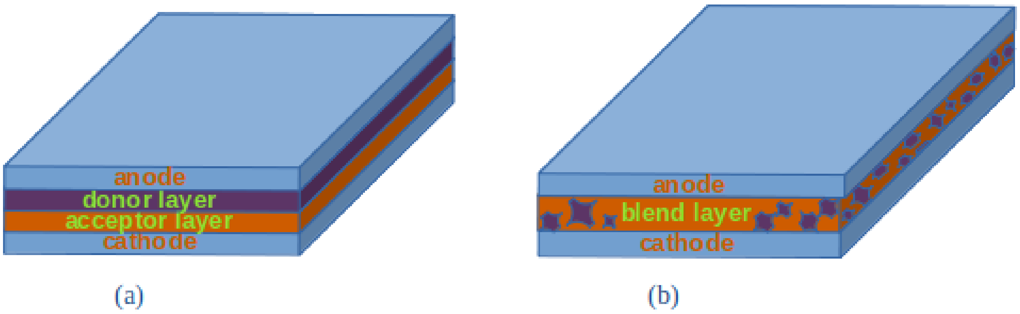

Figure 1.9: Basic types of organic photodetectors (OPDs).

the first category of approaches, the mainstream consists in using the so-called charge collection narrowing (CCN) [93]: in an optically and electrically thick heterojunction, the transit times for the carriers depend on the wavelengths of the incoming photons. For this reason, a narrowband response can be achieved by exploiting the different times. For the second approach, cavity-enhanced OPDs are usually implemented in order to obtain an integrated spectrometer by tuning the cavity length [50], [94], [95]. Xing et al. [94] have suggested a spectrometer built using a transmission cavity-based organic photodetectors with remarkable specific detectivity of 10^{14} Jones and spectral range between 400 nm and 1000 nm. The materials used for the active blend are DCV5T-Me:C60, BDP-OMe:C60, and QM1:C60 because of their absorption spectra in the blue, green and red wavelengths range, respectively. Li et al.[96] have recently suggested a prototype spectrometer based on a special organic semiconductor (namely quinoid-capped OSs) used as photodetectors working between 400 nm and 1250 nm, with a detectivity that is comparable to InGaAs photodetectors ($\sim 10^1 2$ Jones).

1.4.3 Metamaterial-based spectrometers

Metamaterials are defined as structures with artificially produced low-scale patterns that allow some specific optical properties to be achieved. For this reason, metamaterials are also referred to as reconfigurable materials, having physical properties that can be tuned according to their shapes and sizes. Specifically, metamaterials can be designed to be used in photonics applications [97]. In the case of photodetectors, metamaterials give the possibility to have a good spectral tunability [98]. Moving to the quantum size domain (¡ 10 nm), materials show electrical and optical properties that depend on their size. In particular, for 0D nanostructures like quantum dots, the energy gap increases as the size of the nanoparticles decreases. For 1D metamaterials like nanowires and nanotubes, the tunability of the ranges of the physical hallmarks is achieved by changing the radius of the 1D nanostructures, while for 2D materials the thickness of the layers determines their peculiar optoelectronic properties [99], [100]. A very interesting review on the nanomaterials adopted to miniaturize spectrometers has been recently published [6]. The metamaterials typically used as optical integrated components for spectrometers are mainly inorganic, with some of them compatible with complementary metal-oxide- semiconductor (CMOS) technologies. This feature makes them promising materials to realize integrated on chip spectrometers. However, organic quantum dots have also been explored as photodetectors in micro-spectrometers [101]. Among 0D metamaterials, quantum dots (QDs, both organic and inorganic [101]), colloidal quantum dots (CQDs) and perovskite quantum dots are used as optical components in different materials and arrangements [102]–[104]. QDs are also used as filters, as in [105], where an array of PbS and PbSe QDs have been used as optical filter in a reconstructive spectrometer because of their spectrum tunability. Indeed, in this case, the band gaps depend on the size, the composition and the ligand of the QDs. Wen et al.[106] designed micro- spectrometers based on HgSe CQDs and distributed Bragg reflectors, working as a resonant cavity. Among 2D metamaterials, hexagonal boron nitride (hBN) and transition group metal sulfides are used because of their very good optical detection properties. In particular, a black phosphorus- based spectrometer has been fabricated, showing a spectral range of 9 μm with a spectral resolution of 90 nm [61]. The bandgap of black phosphorus is intimately related to the thickness of the sample, hence making the spectral range varying according to a macroscopic quantity. A spectrometer based on a MoS_2/WSe_2 heterojunction in hBN stacked layers has been suggested [64]. Graphene is also adopted [107], [108] in fabricating optical spectrometers. A comprehensive list of 2D materials beyond graphene used in optoelectronics can be found in [109]. Both dispersive gratings and narrowband filters can be produced by using anisotropic metamaterials [110].

1.5 Open-source spectrometer database

So far, an overview of the materials and integration technologies has been presented to show on one hand the richness and variety of data existing in the scientific literature, on the other hand to suggest the need for a referenced framework in which important information could be easily found. The information has been organized according to the diagram and keywords shown in Figure 1.10. All the data available in literature and concerning integrated and micro-/nano- spectrometers have been usefully collected in the database i- PHAOS: integrated PHotodetectors And Optical Spectrometers, in which the metrics for each spectrometer are easily accessible for comparison. In fact,

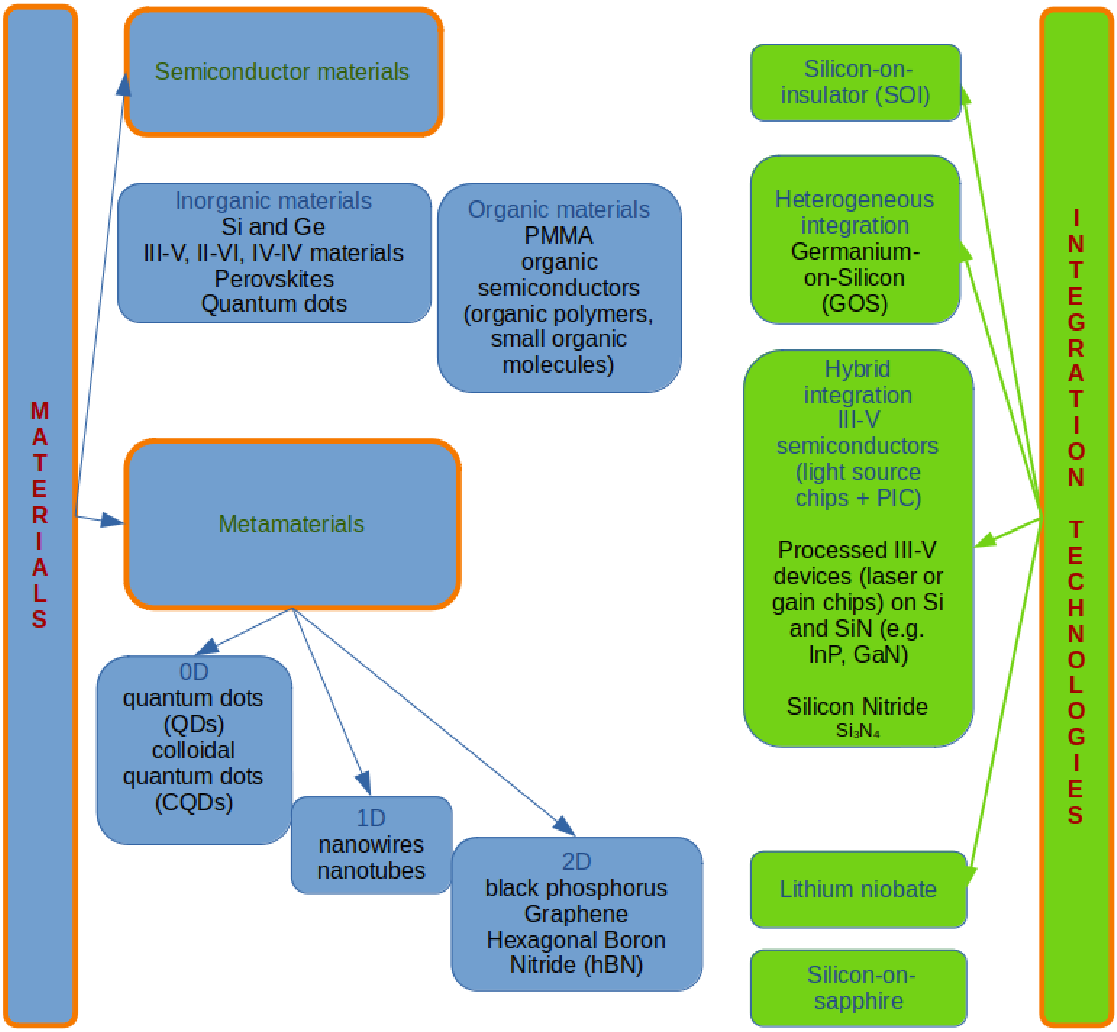

Figure 1.10: Materials and integration technologies implemented in miniaturized spectrometers: an overview.

given the plethora of available data, we suggest here a referenced database available on GitHub at the link `https://github.com/carlamariacoppola/iPHAOS` (released under the GNU v3.0 license). The database is provided as an Excel file consists of two sheets named "spectrometers" and "photodetectors for spectroscopy". A third sheet is provided with the drop-on entries included in the previous sheets. The entries for the references are numbered according to the paper bibliography, while each reference is explicitly mentioned and hyperlinked to the corresponding doi page on the GitHub version. The data included in the sheet named "spectrometers" are:

1. Type of spectrometer: it is possible to choose the entry as dispersive (gratings) spectrometer, filter- based spectrometer, Fourier-transform spectrometer and reconstructive (computational) spectrometer.
2. Materials/Integrated platform
3. Spectral range: it is sub-categorised as spectral range (min value), spectral range (max value), bandwidth and target peak. All data are provided in nm.
4. Spectral resolution [nm]
5. Bandwidth-to-resolution ratio
6. Dynamic range
7. Footprint, area [mm^2]

8. Footprint, volume [mm^3]
9. Measuring speed [s]
10. CMOS compatibility
11. Year
12. Ref.

Similarly to the best available review table available in literature on photodetectors by Wang et al. 2022 [95], the sheet named “photodetectors for spectroscopy” is organized according to the following metrics:

1. Material
2. Spectral range: it is sub-categorised as spectral range (min value), spectral range (max value) and target peak. All data are provided in nm.
3. Spectral resolution [nm]
4. FWHM [nm]
5. D* [Jones]
6. EQE [%]
7. R [A W-1]
8. Bias [V]
9. LDR [dB]
10. f-3dB [kHz]
11. Footprint, area [mm^2]
12. Footprint, volume [mm^3]
13. CMOS compatible
14. Year
15. Ref.

The database available on the GitHub repository can be analysed by means of a Python script as the one provided in the same repository with the filename spectrometers.py. The source file is commented to ease the reader in customizing the queries to the database according to the needs. In this script, the database is imported as a dataframe using the Python library `pandas`, that is also used to perform the analysis of the entries. In the repository, some examples of plots are provided and produced by using the matplotlib library. We report here some examples of plots that can be produced to quickly perform comparison among metrics of interest. In Figure 1.11 the case of the bandwidth in nm for each reference is plotted while in Figure 1.12 the spectral resolution in nm is reported.

In Figure 1.13, the case of a 3D scatter plot of the spectral resolution and the bandwidth-to-resolution ratio for each reference is reported. The multidimensional plots are provided such that, whenever an entry for a specific metric (row) of the database is not available, the corresponding reference is dropped from the dataframe by using the method “dropna”. The project is open-source and scientists are invited to include their data to increase the stored information and keep track of the changes and improvements in the field. All the papers referenced in the database (version tagged as v0 in the github repository) and not yet cited in this manuscript can be found in references [15], [111]–[163].

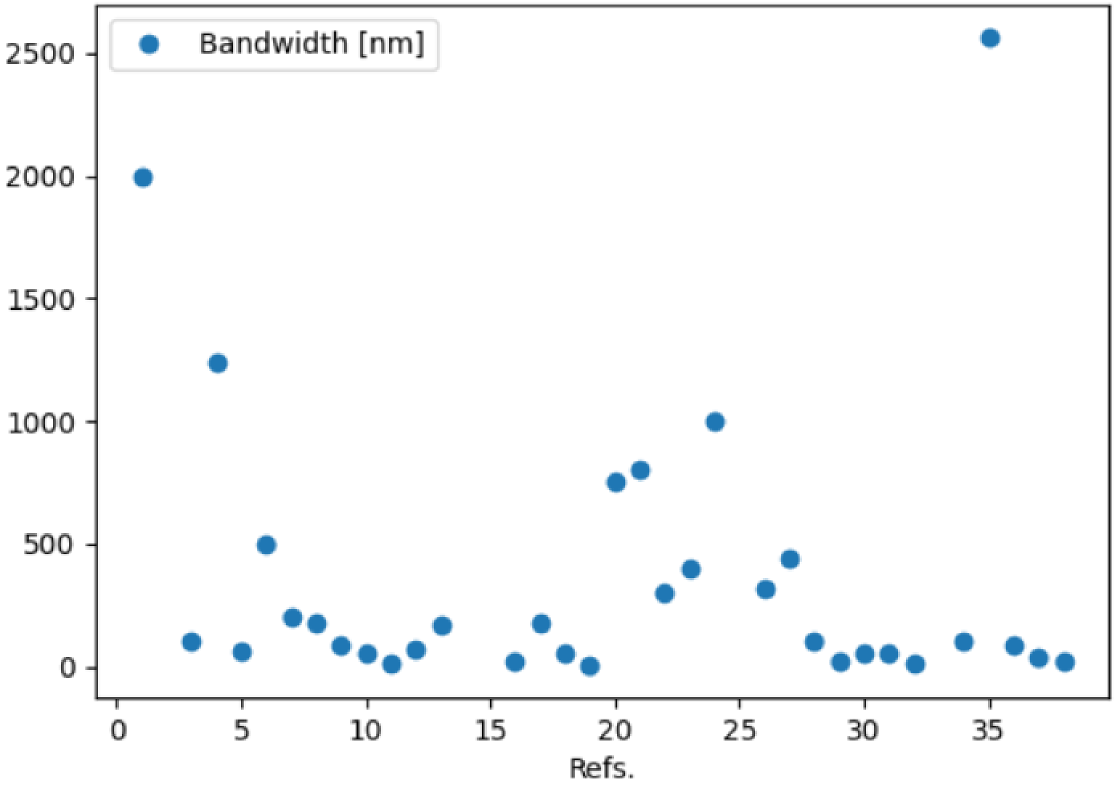

Figure 1.11: Demonstration of plots that the database analysis can generate: example 1.

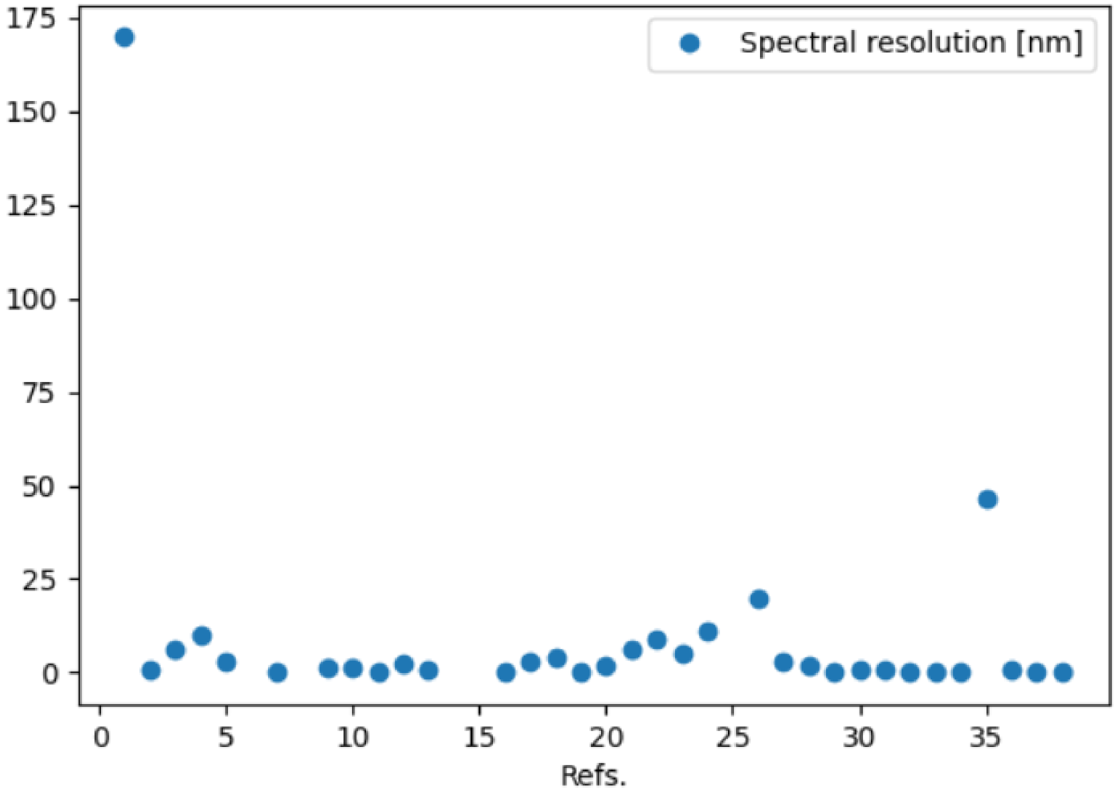

Figure 1.12: Demonstration of plots that the database analysis can generate: example 2.

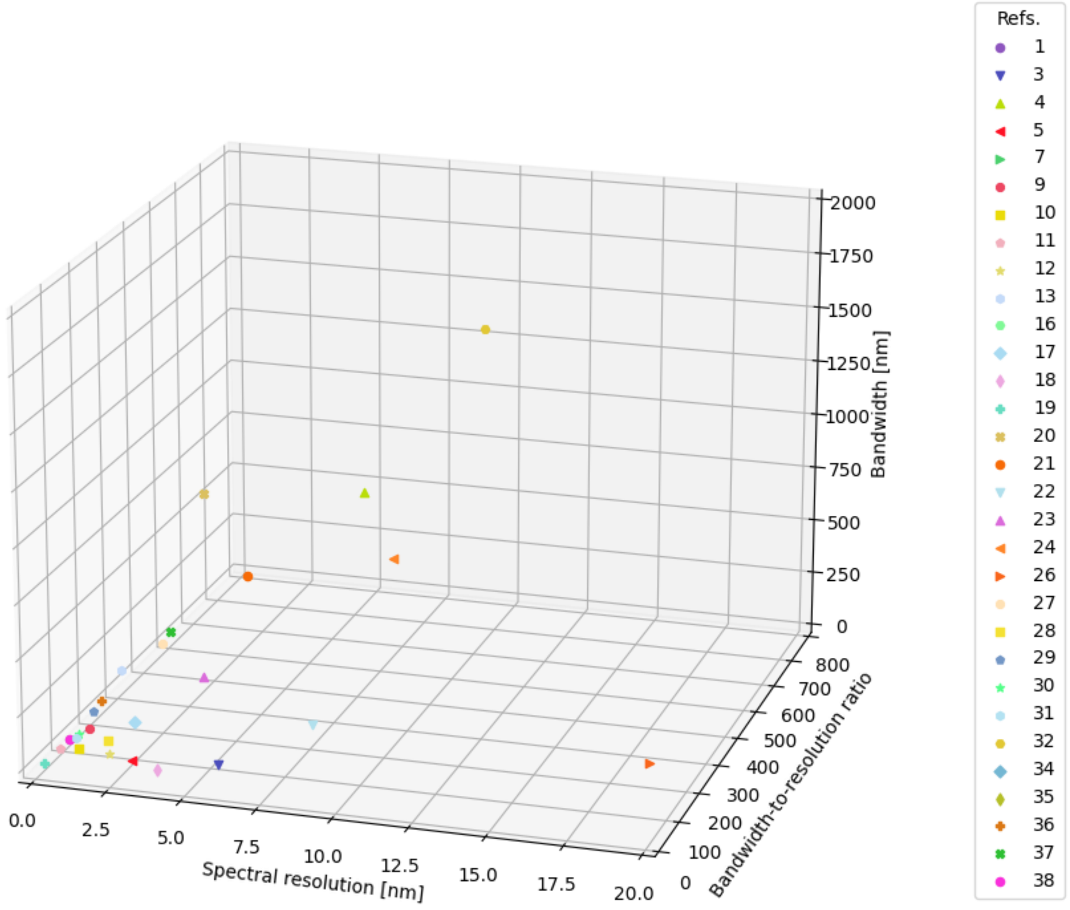

Figure 1.13: Example of informative plots that can be produced by analysing the database: 3D scatter plot of the spectral resolution in nm and bandwidth-to-resolution ratio for each reference providing both entries.

1.6 Conclusions

Optical spectrometers are important and widely used devices for several applications, including research fields as biomedicine, astronomy, chemistry, physics, communication etc. The high demand for portable and miniaturized spectrometers is pushing the recent research towards their on-chip integration, down to the micro- and nano-scale. The challenge of such miniaturization process relies in the intrinsic trade-off between the size of the spectrometer and its performances (i.e. spectral resolution, spectral range, measuring speed). One of the exciting possible applications of the integration of spectrometers is the fabrication of devices able to perform the full spectral analysis of analytes to be characterized (e.g. [79]). In this paper an overview of the main approaches that have been recently followed in the design and development of on- chip integrated spectrometer has been presented. At the current state-of-the-art, the latest works on miniaturized spectrometers show integrated circuits exhibiting footprint that are fractions of mm^2 and bandwidth-to-resolution ratio on the order of hundreds, in some cases thousands. Several technologies and materials are implemented, going from the heavily used silicon (e.g. in SOI, SOS, SiN platforms) to metamaterials of different dimensionality. Because of the availability of numerous modelled and fabricated devices, a devoted database of the main metrics has been created with the aim of collecting the existing information and processing them. This project has been meant to be open-source and collaborative meaning that contributors are invited to send entries to be added to the database via a merge request or email and periodic updates of the database will be released. The database is provided as a tool for people working in the field of research and development of on-chip spectrometers, hence scientists are invited to update the database on the GitHub repository.

Table 1.1: Summary table of pros and cons of the different kinds of integrated spectrometers

WdM/WM	**Spectrometer Type**	**Subtype**	**Pros**	**Cons**
WdM	Dispersive	1D (slab) phase shift	+ Simple design + High measuring speed	- Limited spectral range - Low resolution
		2D phase shift	+ High measuring speed	- More complex fabrication - Low resolution - Larger footprint
	Filter-based	Non-resonant	+ Wide spectral range + High resolution + Tunable options	- Lower spectral resolution - Larger footprint - Power hungry
		Resonant	+ High spectral selectivity + Compact and integrable design	- Sensitive to temperature variations - Fabrication complexity
WM	Fourier-Transform Spectrometers	Spatially modulated	+ High spectral resolution + High throughput (Jacquinot advantage)	- Requires precise alignment - Potentially complex readout
		Temporally modulated	+ Very high spectral resolution (depending on delay range)	- Complex for broadband spectrometers - Requires sophisticated processing

Chapter 2

Digital integrated spectrometer using the Vernier effect

2.1 Introduction

As shown in Chapter 1, integrated spectrometers are emerging as fundamental tools in several fields of science for the detection and analysis of light signals. The need for miniaturized devices is pushing both academia and companies to produce as small and compact as well as reliable and precise spectrometers to be used in many applications, e.g. medicine, environmental sciences, food analysis, astronomy, communications, to name some of them. The main classification summarizes the spectrometers in demultiplexing and multiplexing [5]. The common challenge in the development of on-chip spectrometers is mainly represented by the trade-off between footprint, bandwidth and resolution. According to the application, these metrics have different impact. In general, the lower the footprint, the larger the bandwidth and the smaller the resolution, the better is the spectrometer in terms of the most relevant metrics. In the framework of scientific research, the implementation of miniaturized spectrometers has been possible by the developments in nanophotonic technology made in the very recent decades, allowing at the limit to have micrometers scale spectrometers (e.g. [60], [62], [64]). In particular, integrated spectrometers implementing Vernier wavelength fine-tuning with cascaded micro-ring resonators in their architectures have been suggested (e.g. [164], [165]).

Along with the advances in the design and fabrication of architectures for integrated photonic circuits for spectrometry, material science has greatly enhanced nanophotonics by suggesting and tayloring materials with important optical properties, for example the so-called phase change materials (PCMs). The most relevant features that distinguish these materials rely in their property to have distinct physical phases that can be very fastly switched between; moreover, a significant change in the refractive index between the crystalline and amorphous phases characterizes these materials. This change is non-volatile, hence suggesting, together with other features, several applications in optics, in which PCMs are considered very promising material candidates, e.g. reconfigurable nanophotonics or non-volatile re-writable optical memories etc. Recent reviews on PCMs and applications in photonic integrated circuits can be found in [166] and [167]; specifically, for chalcogenides based PCM, a review of fundamental properties can be found in [168]. Among PCMs, antimony trisulfide, Sb_2S_3 (found in nature in the mineral stibnite) is considered an interesting and promising material because of its optical properties. In fact, its band gap can be tuned between 2.2 eV to 1.6 eV [169] according to its phase thus allowing its use in several optical applications. Moreover, it is possible to tailor its band gap by applying very high pressure, making it a suitable material candidate for thermoelectric applications under very high pressure (where the gap goes down to 0.68 eV at 15 GPa [170]). First-principles calculations to derive optically relevant quantities like dielectric function, refractive index, extinction coefficient, reflectivity and absorption spectrum, have been published in the first decade of 2000 (e.g. [171]); more recently, a review summarizing the development in the research on antimony trisulfide has been published [167].

In this chapter a novel spectrometer is suggested, based on two cascaded ring resonators covered with antimony sulfide. The described segmented configuration allows for the use of these rings as two different scales of a Vernier-like optical caliper. Although simple in its architecture, this

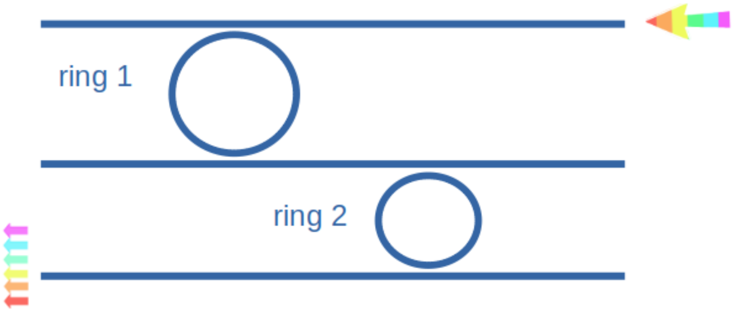

Figure 2.1: Double cascaded ring resonators.

integrated spectrometer shows its robustness in the possibility to geometrically confine the PCM elements hence making the spectrometer digitally controllable. The presented solution represents an important improvement towards the development of high-performance integrated spectrometers, because it enables the possibilty of increasing the bandwidth of a ring-based spectrometer of a specific factor (according to its design) at the cost of much smaller increase of the footprint, without losing resolution.

2.2 General definitions: effective refractive and group indices

2.3 Geometry and basic definitions

The digital spectrometer designed in this paper is reported in **Figure 2.5**. It consists of two cascaded ring resonators made of Si_3N_4, buried in SiO_2, in a Vernier-like architecture. On top of each ring resonator, a layer of antimony sulfide is deposited (**Figure 2.2**, left panel) in many isolated segments (green parts, Figure 2.2, right panel). In fact, in the configuration of the spectrometer here presented, the Sb_2S_3 layer is not continuous but rather intermitting and interspersed with SiO_2. Temperature control on the PCM segments (hence the non-volatile phase-change) is performed via graphene-based microheaters. The Sb_2S_3 phases (amorphous or crystalline) are hereafter denoted as a and c, respectively; they are characterized by different refractive indices. The effective index of a material can be expressed as a Taylor expansion around a certain value of wavelength λ_0 [172]:

$$n_{eff}(\lambda) = n_{eff}(\lambda_0) + \frac{dn_{eff}(\lambda)}{d\lambda}\Big|_{\lambda_0}(\lambda - \lambda_0) + ... + \mathcal{O}(n) \tag{2.1}$$

hence at the first order in the expansion the effective index can be expressed as:

$$n_{eff}(\lambda) = n_{eff}(\lambda_0) + \frac{n_{eff}(\lambda_0) - n_{g,eff}(\lambda_0)}{\lambda_0}(\lambda - \lambda_0) \tag{2.2}$$

Both group and effective refractive indices depend on the material and on the geometry of the light-confining device. The effective and group refractive indices of all the materials used in this spectrometer are reported in **Table 2.1**. They have been computed at wavelength $\lambda_0 = 1.55\mu m$, for a geometry like the one shown in Figure 2.2, left panel, using the MODE - Finite Difference Eingenmode (FDE) solver available in Ansys Lumerical - Optics [173]. The refractive indices used to compute data in Table 2.1 are: $n_{Si_3N_4} = 1.9963$, $n_{SiO_2} = 1.444$, $n_{Sb_2S_3(a)} = 2.712$, $n_{Sb_2S_3(c)} = 3.308$.

Hereafter, the index 1 and 2 denote quantities describing or belonging to the upper (first) ring and the lower (second) ring, respectively. The total phase shift for each loop and ring can be written as:

$$\beta_1 l_1 = \beta_{SiO_2,1} l_{SiO_2,1} + \beta_{a,1} l_{a,1} + \beta_{c,1} l_{c,1} \tag{2.3}$$

$$\beta_2 l_2 = \beta_{SiO_2,2} l_{SiO_2,2} + \beta_{a,2} l_{a,2} + \beta_{c,2} l_{c,2} \tag{2.4}$$

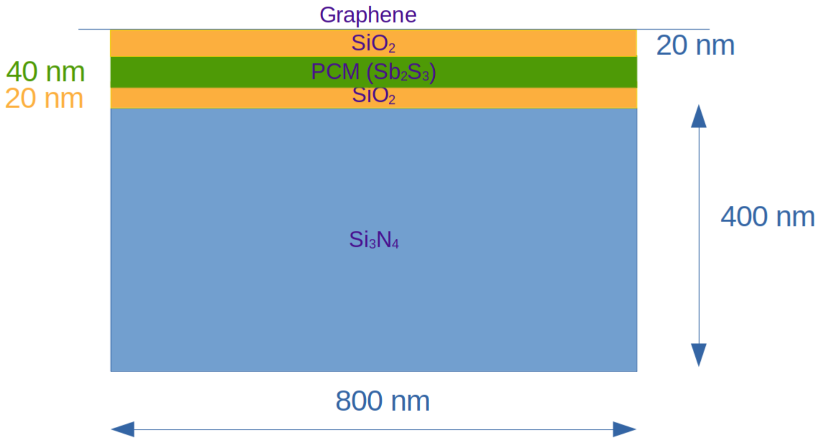

(a)

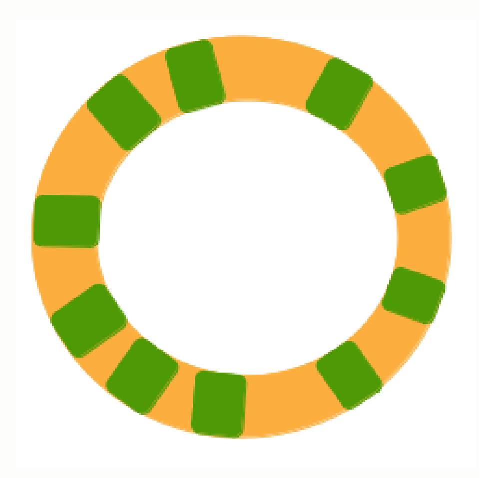

(b)

Figure 2.2: Geometrical arrangement of the materials in the simulations performed in this work. A Si_3N_4 ring resonator is intermittently covered by stibnite, further covered by graphene micro-heaters in order to allow the stibnite to be warmed up and eventually undergo a phase transition. (a) Section view. (b) Top view.

In Equation 2.3 l_1 corresponds to the total length of ring 1 while $l_{SiO_2,1}$, $l_{a,1}$ and $l_{c,1}$ correspond to the total lengths of the segments made with the material SiO_2, amorphous Sb_2S_3 and crystalline Sb_2S_3 in ring 1, respectively. $\beta_{SiO_2,1}$, $\beta_{a,1}$ and $\beta_{c,1}$ represent the phase constants associated to the total SiO_2, amorphous Sb_2S_3 and crystalline Sb_2S_3 segments in ring 1:

$$\beta_{SiO_2,1} = \frac{2\pi}{\lambda} n_{eff,SiO_2,1}(\lambda) \tag{2.5}$$

$$\beta_{a,1} = \frac{2\pi}{\lambda} n_{eff,a,1}(\lambda) \tag{2.6}$$

$$\beta_{c,1} = \frac{2\pi}{\lambda} n_{eff,c,1}(\lambda) \tag{2.7}$$

being $n_{eff,SiO_2,1}(\lambda)$, $n_{eff,a,1}(\lambda)$ and $n_{eff,c,1}(\lambda)$ the effective refractive indices of the cross-sections without PCM segments, with amorphous and with crystalline segments for ring 1, respectively. Similarly, in Equation 2.4 l_2 represents the total length of ring 2 while $l_{SiO_2,2}$, $l_{a,2}$ and $l_{c,2}$ are the total lengths of the segments made with the material SiO_2, amorphous Sb_2S_3 and crystalline Sb_2S_3 in ring 2. $\beta_{SiO_2,2}$, $\beta_{a,2}$ and $\beta_{c,2}$ represent the phase constants associated to the total SiO_2,

Material	$n_{eff}(\lambda_0)$	$n_{g,eff}(\lambda_0)$	$\left.\frac{d^2 n_{eff}(\lambda)}{d\lambda^2}\right\vert_{\lambda_0} \left[\frac{ps}{\mathrm{nm \cdot km}}\right]$
Si_3N_4 + SiO_2	1.600225	2.022070	-1553.6
Si_3N_4 +Sb_2S_3 (a)	1.657544	2.113090	-1038.6
Si_3N_4 +Sb_2S_3 (c)	1.716478	2.243614	-1012.5

Table 2.1: Group and effective refractive indices for the materials and geometry as in Figure 2.2 at $\lambda_0 = 1.55\mu m$. The labels “a“ and “c” refer to antimony sulfide in its amorphous and crystalline states, respectively.

amorphous Sb_2S_3 and crystalline Sb_2S_3 segments in ring 2:

$$\beta_{SiO_2,2} = \frac{2\pi}{\lambda} n_{eff,SiO_2,2}(\lambda) \tag{2.8}$$

$$\beta_{a,2} = \frac{2\pi}{\lambda} n_{eff,a,2}(\lambda) \tag{2.9}$$

$$\beta_{c,2} = \frac{2\pi}{\lambda} n_{eff,c,2}(\lambda) \tag{2.10}$$

being $n_{eff,SiO_2,2}(\lambda)$, $n_{eff,a,2}(\lambda)$ and $n_{eff,c,2}(\lambda)$ the effective refractive indices of the cross-sections without PCM segments, with amorphous and with crystalline segments for ring 2, respectively. In Equation 2.3 and Equation 2.4 β_1 and β_2 are the equivalent phase constants for ring 1 and 2, respectively, that can be written as:

$$\beta_1 = \frac{2\pi}{\lambda} n_{eff,1}(\lambda, \eta_{SiO_2,1}, \eta_{a,1}) \tag{2.11}$$

$$\beta_2 = \frac{2\pi}{\lambda} n_{eff,2}(\lambda, \eta_{SiO_2,2}, \eta_{a,2}) \tag{2.12}$$

where $n_{eff,1}$ and $n_{eff,2}$ are equivalent effective refractive indices for ring 1 and ring 2, respectively. The term “equivalent” refers to the fact that such index corresponds to the effective refractive index of an equivalent cross section, uniform along the ring and leading to the same propagation constant. In Equation 2.11, $\eta_{\mathrm{SiO_2},1}$ and $\eta_{\mathrm{a},1}$ are the fractions of SiO_2, amorphous Sb_2S_3 and crystalline Sb_2S_3 segments over the total length of ring 1, respectively. Equivalently, in Equation 2.12, $\eta_{\mathrm{SiO_2},2}$ and $\eta_{\mathrm{a},2}$ are the fractions of SiO_2 segments and amorphous PCM over the total length of ring 2, respectively. In fact, recalling equations from Equation 2.3 to Equation 2.10, $n_{eff,1}$ and $n_{eff,2}$ can be expressed as a weighted average of the effective refractive indices of each material:

$$\begin{aligned} n_{eff,1}(\lambda, \eta_{Si,1}, \eta_{a,1}) =& \eta_{SiO_2,1} \cdot n_{eff,SiO_2,1}(\lambda) + \\ & \eta_{a,1} \cdot n_{eff,a,1}(\lambda) + \\ & (1 - \eta_{a,1} - \eta_{SiO_2,1}) \cdot n_{eff,c,1}(\lambda) \end{aligned} \tag{2.13}$$

$$\begin{aligned} n_{eff,2}(\lambda, \eta_{Si,2}, \eta_{a,2}) =& \eta_{SiO_2,2} \cdot n_{eff,Si,2}(\lambda) + \\ & \eta_{a,2} \cdot n_{eff,a,2}(\lambda) + \\ & (1 - \eta_{a,2} - \eta_{SiO_2,2}) \cdot n_{eff,c,2}(\lambda) \end{aligned} \tag{2.14}$$

Omitting the subscript 1 or 2 (being valid for both rings), it is then possible to write the equivalent effective refractive index as:

$$\begin{aligned} n_{eff}(\lambda, \eta_{Si}, \eta_a) =& \eta_{SiO_2} \cdot n_{eff,SiO_2}(\lambda) + \\ & \eta_a \cdot n_{eff,a}(\lambda) + \\ & (1 - \eta_{SiO_2} - \eta_a) \cdot n_{eff,c}(\lambda). \end{aligned} \tag{2.15}$$

According to Equation 2.1 and at the first order in the Taylor expansion, Equation 2.15 can be written as:

$$n_{eff}(\lambda, \eta_{SiO_2}, \eta_a) = A + B \cdot (\lambda - \lambda_0) \tag{2.16}$$

being:

$$\begin{aligned}A &= \eta_{SiO_2} \cdot n_{eff,SiO_2}(\lambda_0) \\ &\quad + \eta_a \cdot n_{eff,a}(\lambda_0) + [1 - \eta_{SiO_2} - \eta_a] \cdot n_{eff,c}(\lambda_0) \\ &= \eta_{SiO_2}[n_{eff,SiO_2}(\lambda_0) - n_{eff,c}(\lambda_0)] \\ &\quad + \eta_a[n_{eff,a}(\lambda_0) - n_{eff,c}(\lambda_0)] \\ &\quad + n_{eff,c}(\lambda_0)\end{aligned}$$

and

$$\begin{aligned}B &= \eta_{SiO_2} \cdot \frac{dn_{eff,SiO_2}(\lambda)}{d\lambda}\Big|_{\lambda_0} + \eta_a \cdot \frac{dn_{eff,a}(\lambda)}{d\lambda}\Big|_{\lambda_0} + \\ &(1 - \eta_{SiO_2} - \eta_a) \cdot \frac{dn_{eff,c}(\lambda)}{d\lambda}\Big|_{\lambda_0} \\ &= \eta_{SiO_2} \cdot \left[\frac{dn_{eff,SiO_2}(\lambda)}{d\lambda}\Big|_{\lambda_0} - \frac{dn_{eff,c}(\lambda)}{d\lambda}\Big|_{\lambda_0}\right] + \\ &\eta_a \cdot \left[\frac{dn_{eff,a}(\lambda)}{d\lambda}\Big|_{\lambda_0} - \frac{dn_{eff,c}(\lambda)}{d\lambda}\Big|_{\lambda_0}\right] + \\ &\frac{dn_{eff,c}(\lambda)}{d\lambda}\Big|_{\lambda_0}\end{aligned}$$

and being l and m the length of the ring resonator and the resonance order, respectively. For a ring resonator, the resonance wavelength is given by:

$$\lambda_{RES} = \frac{n_{eff}(\lambda_{RES}, \eta_{SiO_2}, \eta_a) \cdot l}{m} \tag{2.17}$$

As a first order in the expansion, the resonance wavelength can then be found by inserting Equation 2.16 in Equation 2.17:

$$\lambda_{RES} = \frac{[A + B \cdot (\lambda_{RES} - \lambda_0)] \cdot l}{m} \tag{2.18}$$

implying:

$$\lambda_{RES} = \frac{A - B\lambda_0}{\frac{m}{l} - B}. \tag{2.19}$$

It corresponds to the length that fills the total ring length an integer number of times; in particular, since light is propagating in a medium, this translates into having the optical path length that is an integer multiple of the resonance wavelength. We define the right side of Equation 2.19 as:

$$\begin{aligned}F\Big(&m, l, \eta_{Si}, \eta_a, \\ &n_{eff,SiO_2}(\lambda_0), n_{eff,a}(\lambda_0), n_{eff,c}(\lambda_0), \\ &\frac{dn_{eff,SiO_2}(\lambda)}{d\lambda}\Big|_{\lambda_0}, \frac{dn_{eff,a}(\lambda)}{d\lambda}\Big|_{\lambda_0}, \frac{dn_{eff,c}(\lambda)}{d\lambda}\Big|_{\lambda_0}\Big)\end{aligned}$$

For convenience, in the following, all parameters associated to a ring and the ones depending to a fixed wavelength λ_0 will be identified with the symbol:

$$\begin{aligned}\mathfrak{R} \equiv \Big\{&m, l, \eta_{SiO_2}, \eta_a, \\ &n_{eff,SiO_2}(\lambda_0), n_{eff,a}(\lambda_0), n_{eff,c}(\lambda_0), \\ &\frac{dn_{eff,SiO_2}(\lambda)}{d\lambda}\Big|_{\lambda_0}, \frac{dn_{eff,a}(\lambda)}{d\lambda}\Big|_{\lambda_0}, \frac{dn_{eff,c}(\lambda)}{d\lambda}\Big|_{\lambda_0}\Big\}\end{aligned}$$

Hence, $\mathfrak{R}_1$ and $\mathfrak{R}_2$ represent the set of optical and geometrical parameters specific to ring 1 and 2, respectively.

2.4 Working principles

The particular configuration of each ring in the described architecture can be interpreted as a digitalization of the ring resonator. For this reason, in principle, such a digitalized ring resonator can be used *per se* to scan wavelengths, then working as a spectrometer. Introducing further digitalized ring resonator in cascade is a way to improve the spectral resolution and to increase the bandwidth. The described system can be interpreted as an integrated spectrometer implementing the so-called Vernier effect. The main point of such tool is to use different scales for a higher precision measurement of lengths: the resolution obtained by using the scales simultaneously is higher than the resolutions of the measurements performed by using the scales separately. In the design described in this paper, the two scales with different periods are represented by ring resonators with different lengths, thus having different resonances wavelengths. In this perspective, the cascaded ring resonators covered with PCM segments (hence with tunable optic lengths) can be considered as an "optic Vernier caliper". In optics, it is possible to harness this effect by means of interferometers with different interferometric frequencies (e.g. [174]).

In order to use such a configuration for implementing a Vernier effect-based spectrometer, the conditions to be satisfied are:

- the lengths of the rings should be different and the ratio between optical paths should be a rational number;
- each ring should be covered with PCM segments (Sb_2S_3 in our case) in order to achieve different optical path lenghts (OPLs);
- only one transmission peak should be visible at the output (i.e. the Vernier architecture should be designed in the first operating regime [175], [176]);
- the resonances of the two rings should be aligned by changing the phase of the PCM segments (hence the refractive index) of the second ring;
- the resonances should be appropriately tuned by changing the phase of the PCM segments (hence the refractive index) of the first ring.

Indeed, ring resonators are characterized by a fixed geometrical length l corresponding to an OPL, due to the fact that light is traveling in a material with a certain effective refractive index. The optical path length is given by the product of the effective refractive index and the physical length the light is traveling through:

$$OPL = n \cdot l \tag{2.20}$$

The rings can have different arrangements of refractive indices because of the topology adopted to build them; specifically, by interspersing active optic materials with changing phase like Sb_2S_3 it is possible to digitally control the change of the effective refractive indices. As a consequence, different optical path lenghts are achieved. In the presented spectrometer, in the initial operational configuration all Sb_2S_3 segments are in their crystalline phase. In this condition, the system is in its coldest state. In fact, the phase variation (and, as a consequence, the refractive index change) is achieved by increasing the temperature of a certain amount of the PCM segments. The choice of Sb_2S_3 has been suggested by its very promising features (large bandgap, high refractive index, low optical losses) in the near-infrared (NIR) among other PCM candidates for nanophotonic applications. As shown in [177], the variation in the refractive indices between amorphous and crystalline phases is around 0.57, and the extinction coefficients (both for the crystal and amorphous phases) are negligible for wavelenghts above 700 nm. As a first step, the optical path along each ring resonator is adjusted in order to initially align one resonance of the two resonators at a common wavelength λ_0 (panel (a) in **Figure 2.8**). Eventually, both optical paths of the two resonators are adjusted simultaneously to gradually shift the peak of the output, thus scanning the wavelength in between the first resonance and the following one. Then, a second alignment is performed between immediately subsequent resonances (panel (b) in Figure 2.8); again the optical paths of the two rings are tuned simultaneously to scan the wavelength of the spectrometer in between the second and the third resonances. This procedure is performed for all the resonances up to the last one, represented by the minimum number between the number of resonances of the first and second ring.

The expression of the power transmission at the drop port of each ring is defined as [178]:

$$T_d = \frac{I_{drop}}{I_{input}} = \frac{(1-r_1^2)(1-r_2^2)a}{1-2r_1r_2a\cos(\phi)+(r_1r_2a)^2} \tag{2.21}$$

in the assumption of continuous wave operation, matching fields and negligible back reflections into the bus waveguides. In Equation 2.21, a represents the single-pass amplitude transmission, related to the power attenuation coefficient α as $a^2 = \exp^{-\alpha \cdot l}$, while r_1 and r_2 are the self-coupling coefficients of the ring with the bus waveguides; ϕ is the total phase shift along the ring, defined as in Equation 2.3 and Equation 2.4. The power transmission of the full device is given by the product of the power transmission at the drop port of each ring.

2.4.1 Description of the algorithm

Mathematically, the procedures of aligning the resonances and scanning the wavelengths are achieved according to the following algorithm:

1. the optical length of the first ring is fixed such that the first resonance corresponds to a fixed wavelength λ_0, according to Equation 2.17:

   $$l_1 = \frac{m_1 \cdot \lambda_0}{n_{eff1}} \tag{2.22}$$

   and in the condition of no-amorphous PCM for the first ring ($\eta_{a1} = 0$).

2. the closer resonance to λ_0 for the second ring is aligned to λ_0 by searching the length l_2^* of the second ring under the condition of no-amorphous PCM ($\eta_{a,2} = 0$) in both first and second ring:

   $$\frac{A_2 - B_2\lambda_0}{\frac{m_2}{l_2} - B_2} = \frac{A_1 - B_1\lambda_0}{\frac{m_1}{l_1} - B_1}$$
   $$\Downarrow$$
   $$l_2^* = \frac{m_2}{B_2 + \left(\frac{m_1}{l_1} - B_1\right)\frac{A_2 - B_2\lambda_0}{A_1 - B_1\lambda_0}} \tag{2.23}$$

3. all the resonances are aligned: this is achieved by finding η_{a2} [1] such that:

   $$\frac{A_2 - B_2\lambda_0}{\frac{m_2+i}{l_2^*} - B_2} = \frac{A_1 - B_1\lambda_0}{\frac{m_1+i}{l_1} - B_1} \tag{2.24}$$

   This condition corresponds to having:

   $$\eta_{a2}^* = \frac{k_1\frac{m_2+i}{l_2^*} - k_2 - k_1k_3 + k_3\lambda_0}{k_4 - k_5\lambda_0 + k_1k_5} \tag{2.25}$$

   where:

   $$k_1 = \frac{A_1 - B_1\lambda_0}{\frac{m_1+i}{l_1} - B_1}$$
   $$k_2 = \eta_{Si,2}[n_{eff2,Si}(\lambda_0) - n_{eff2,c}(\lambda_0)] + n_{eff2,c}(\lambda_0)$$
   $$k_3 = \eta_{Si,2}\cdot \left[\left.\frac{dn_{eff2,Si}(\lambda)}{d\lambda}\right|_{\lambda_0} - \left.\frac{dn_{eff2,c}(\lambda)}{d\lambda}\right|_{\lambda_0}\right] + \left.\frac{dn_{eff2,c}(\lambda)}{d\lambda}\right|_{\lambda_0}$$
   $$k_4 = n_{eff2,a}(\lambda_0) - n_{eff2,c}(\lambda_0)$$
   $$k_5 = \left.\frac{dn_{eff2,a}(\lambda)}{d\lambda}\right|_{\lambda_0} - \left.\frac{dn_{eff2,c}(\lambda)}{d\lambda}\right|_{\lambda_0}$$

---

[1] (in case of i=0, Equation 2.31 is solved for $\eta_{a,2}^* = 0$, according to initial fully crystalline condition of the PCM segments of the second ring)

4. the wavelengths are tuned in order to scan from one resonance to the following, according to a resolution lower or equal to a fixed $\Delta\lambda_{\min}$. This is achieved by:
   (a) finding η_{a1}^{scan} such that for each resonance:

$$\frac{A_1^{(j+1)} - B_1^{(j+1)}\lambda_0}{\frac{m_1+i}{l_1} - B_1^{(j+1)}} - \frac{A_1^{(j)} - B_1^{(j)}\lambda_0}{\frac{m_1+i}{l_1} - B_1^{(j)}} = \Delta\lambda_{\min} \tag{2.26}$$

   that corresponds to having:

$$\tilde{\eta}_{a1}^{scan} = \frac{k_1^*\left(\frac{m_1+i}{l_1} - k_3^*\right) - k_2^* + k_3^*\lambda_0}{k_4 - k_5 * \lambda_0 + k_1^* k_5} \tag{2.27}$$

   where:

$$\begin{aligned} k_1^* &= \mathrm{j} * \Delta\lambda_{\min} + F(\mathfrak{R}_1) \\ k_2^* &= \eta_{Si,1} \cdot \\ &\quad [n_{eff1,Si}(\lambda_0) - n_{eff1,c}(\lambda_0)] + n_{eff1,c}(\lambda_0) \\ k_3^* &= \eta_{Si,1} \cdot \\ &\quad \left[\left.\frac{dn_{eff1,Si}(\lambda)}{d\lambda}\right|_{\lambda_0} - \left.\frac{dn_{eff1,c}(\lambda)}{d\lambda}\right|_{\lambda_0}\right] \\ &\quad + \left.\frac{dn_{eff1,c}(\lambda)}{d\lambda}\right|_{\lambda_0} \end{aligned}$$

   (b) searching η_{a2} in order to align the resonances, as for the previous step:

$$\frac{A_2^{(j+1)} - B_2^{(j+1)}\lambda_0}{\frac{m_2+i}{l_2^*} - B_2^{(j+1)}} - \frac{A_2^{(j)} - B_2^{(j)}\lambda_0}{\frac{m_2+i}{l_1} - B_2^{(j)}} = \Delta\lambda_{\min}$$

   corresponding to:

$$\tilde{\eta}_{a2}^{scan} = \frac{k_1^{**}\left(\frac{m_2+i}{l_2} - k_3^*\right) - k_2^* + k_3^*\lambda_0}{k_4 - k_5 * \lambda_0 + k_1^{**} k_5}$$

2.5 The Vernier effect

The described system can be used as an integrated spectrometer implementing the so-called Vernier effect[2] applied to optics, under the condition that:

- the resonances of the two rings can be aligned;
- the resonances can be appropriately tuned by changing the refractive index of the rings

The principle will be here explained for linear lengths for an easier presentation in terms of figures, but it can be eventually extended to rings. Let's imagine to have two different rulers as in the top panel of Fig. 2.4. Once aligning the zeros of the two scales, the rulers marks will be at the same position after integer multiples of a certain length L. In L there are m_1 marks of the first ruler and m_2 marks of the second ruler; these numbers represent the non-common integer factors that can be found when considering multiple integers of L (see central panel of Fig. 2.4 for an example). The second scale is called the Vernier scale, and it measures smaller distances. The measurement is performed by adding the readout value obtained with the first scale (2, in the example shown in Fig. 2.4, bottom panel) together with the value read with the Vernier scale and obtained by

---

[2] In 1631 the French mathematician Pierre Vernier invented the measurement tool called "Vernier scale" after his name; this device was described in the book *Construction, l'usage et les propriétés du quadrant nouveau de mathématique*. The main point of such tool is to use different scales for a higher precision measurement of lengths: the resolution obtained by using the scales simultaneously is higher than the resolutions of the measurements performed by using the scales separately.

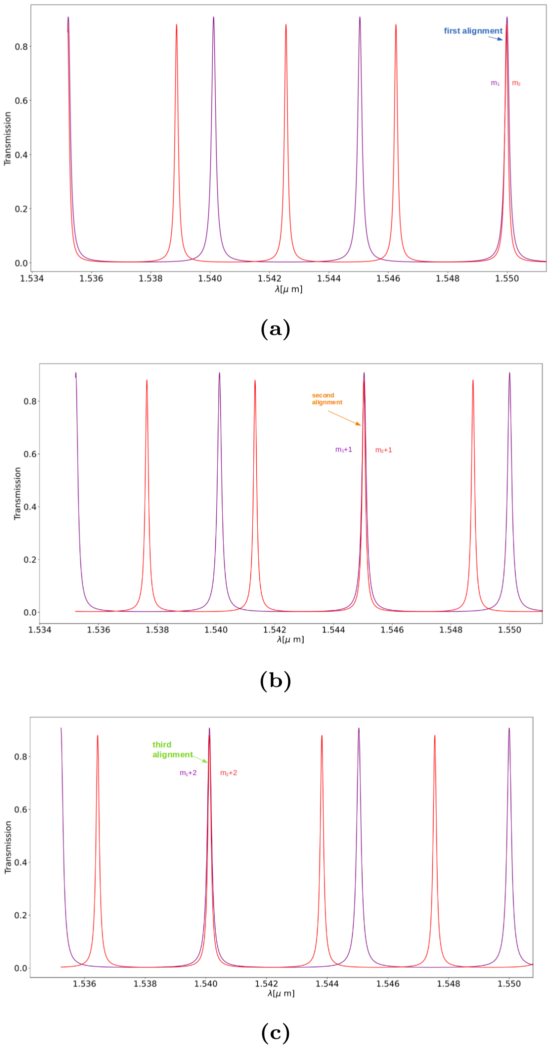

(a)

(b)

(c)

Figure 2.3: Alignments of the resonances of ring 1 and ring 2: first alignment (a), second alignment (b) and third alignment (c).

reading the first value at which the marks of the two scales align (8 in the example, same figure). In this way, it is possible to achieve a higher resolution in the measurement of lengths.

It is possible to extend this concept to ring resonators. They are characterized by a fixed geometrical length l that influences the optical path length (OPL) due to the fact that light is traveling in a material with a certain effective refractive index. The optical path length is given by the product of the effective refractive index and the physical length the light is traveling through:

$$OPL = n \cdot l \tag{2.28}$$

The rings can have different arrangements of refractive indices because of the topology adopted to build them; specifically, by interspersing active optic materials with changing phase with Si_3N_4 it is possible to digitally control the change of the refractive indices.

2.6 Algorithm

The procedure of aligning the resonances is achieved according to the following algorithm:

1. the length of the first ring is fixed such that the resonance corresponds to a fixed wavelength λ_0, according to Eq. 2.17:

$$l_1 = \frac{m_1 \cdot \lambda_0}{n_{eff1}} \tag{2.29}$$

and in the condition of no-amorphous PCM for the first ring ($\eta_{a1} = 0$).

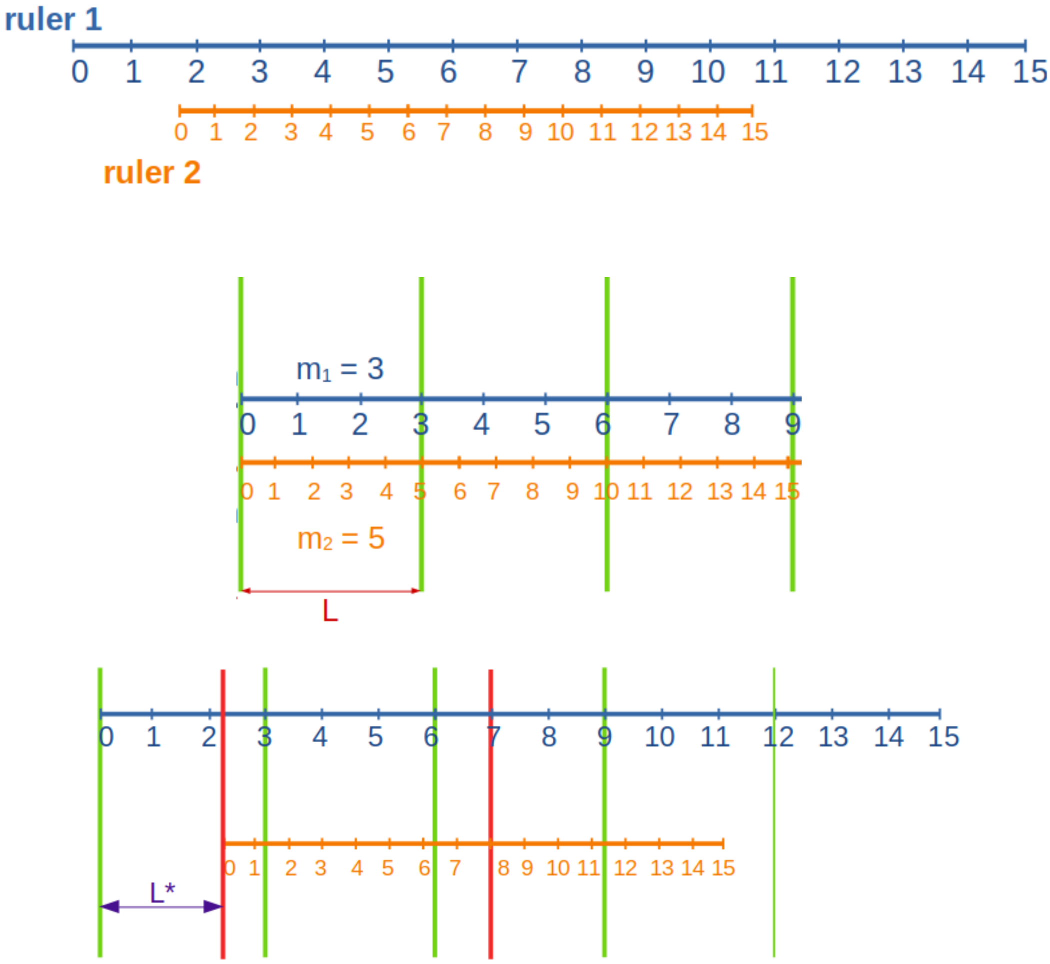

Figure 2.4: Explanation of the algorithm behind the Vernier. *Top panel:* at least two different rulers are needed in order to build a Vernier. *Central panel:* the zero in the measurement is obtained by aligning the zeros of the two rulers. The marks of the rulers align every integer numbers m_1 and m_2 . *Bottom panel:* the measurement of the length of L* is found by adding the value read from the first ruler (2 units of the first ruler) and the first value of the second ruler at which the marks align (8 units of the second ruler).

2. the closer resonance to λ_0 for the second ring is aligned to λ_0 by searching the length of the second ring under the condition of no-amorphous PCM in both first and second ring:

$$\frac{A_2 - B_2\lambda_0}{\frac{m_2}{l_2} - B_2} = \frac{A_1 - B_1\lambda_0}{\frac{m_1}{l_1} - B_1}$$

$$\Downarrow$$

$$l_2^* = \frac{m_2}{B_2 + \left(\frac{m_1}{l_1} - B_1\right)\frac{A_2 - B_2\lambda_0}{A_1 - B_1\lambda_0}} \tag{2.30}$$

3. aligning all the resonances: this is achieved by finding η_{a2} such that:

$$\frac{A_2 - B_2\lambda_0}{\frac{m_2+i}{l_2^*} - B_2} = \frac{A_1 - B_1\lambda_0}{\frac{m_1+i}{l_1} - B_1} \tag{2.31}$$

This condition corresponds to having:

$$\eta_{a2}^* = \frac{k_1\frac{m_2+i}{l_2^*} - k_2 - k_1k_3 + k_3\lambda_0}{k_4 - k_5\lambda_0 + k_1k_5} \tag{2.32}$$

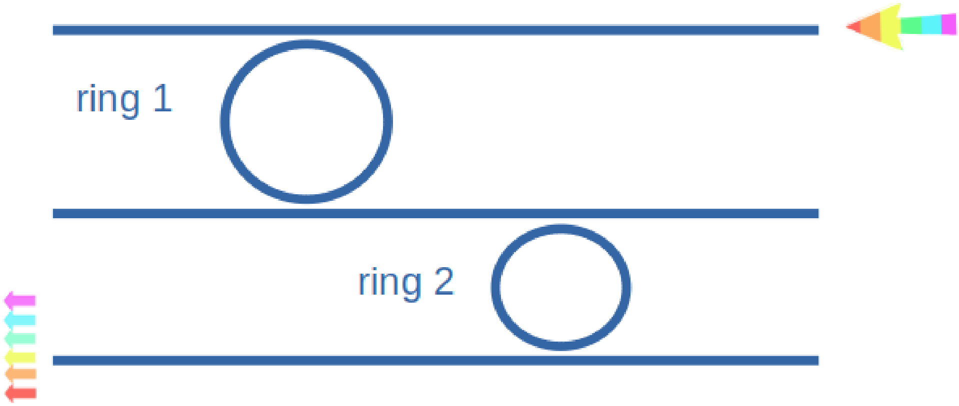

Figure 2.5: Double cascaded ring resonators.

where:

$$\begin{aligned}
k_1 &= \frac{A_1 - B_1\lambda_0}{\frac{m_1+i}{l_1} - B_1} \\
k_2 &= \eta_{Si,2}[n_{eff2,Si}(\lambda_0) - n_{eff2,c}(\lambda_0)] + n_{eff2,c}(\lambda_0) \\
k_3 &= \eta_{Si,2}\left[\frac{dn_{eff2,Si}(\lambda)}{d\lambda}\bigg|_{\lambda_0} - \frac{dn_{eff2,c}(\lambda)}{d\lambda}\bigg|_{\lambda_0}\right] + \frac{dn_{eff2,c}(\lambda)}{d\lambda}\bigg|_{\lambda_0} \\
k_4 &= n_{eff2,a}(\lambda_0) - n_{eff2,c}(\lambda_0) \\
k_5 &= \frac{dn_{eff2,a}(\lambda)}{d\lambda}\bigg|_{\lambda_0} - \frac{dn_{eff2,c}(\lambda)}{d\lambda}\bigg|_{\lambda_0}
\end{aligned}$$

4. tuning the wavelengths in order to scan from one resonance to the following. This is achieved by:
   (a) η_{a1}^{scan} found such that for each resonance:

   $$\frac{A_1^{(j+1)} - B_1^{(j+1)}\lambda_0}{\frac{m_1+i}{l_1} - B_1^{(j+1)}} - \frac{A_1^{(j)} - B_1^{(j)}\lambda_0}{\frac{m_1+i}{l_1} - B_1^{(j)}} = \text{resolution} \tag{2.33}$$

   that corresponds to have:

   $$\tilde{\eta}_{a1}^{scan} = \frac{k_1^*\left(\frac{m_1+i}{l_1} - k_3^*\right) - k_2^* + k_3^*\lambda_0}{k_4 - k_5 * \lambda_0 + k_1^* k_5} \tag{2.34}$$

   where:

   $$\begin{aligned}
   k_1^* &= \text{j} * \text{resolution} + F(\mathfrak{R}_1) \\
   k_2^* &= \eta_{Si,1}[n_{eff1,Si}(\lambda_0) - n_{eff1,c}(\lambda_0)] + n_{eff1,c}(\lambda_0) \\
   k_3^* &= \eta_{Si,1}\left[\frac{dn_{eff1,Si}(\lambda)}{d\lambda}\bigg|_{\lambda_0} - \frac{dn_{eff1,c}(\lambda)}{d\lambda}\bigg|_{\lambda_0}\right] + \frac{dn_{eff1,c}(\lambda)}{d\lambda}\bigg|_{\lambda_0}
   \end{aligned}$$

   (b) η_{a2} is searched in order to align, as for the previous step:

   $$\frac{A_2^{(j+1)} - B_2^{(j+1)}\lambda_0}{\frac{m_2+i}{l_2^*} - B_2^{(j+1)}} - \frac{A_2^{(j)} - B_2^{(j)}\lambda_0}{\frac{m_2+i}{l_1} - B_2^{(j)}} = \text{resolution}$$

   corresponding to:

   $$\tilde{\eta}_{a2}^{scan} = \frac{k_1^{**}\left(\frac{m_2+i}{l_2} - k_3^*\right) - k_2^* + k_3^*\lambda_0}{k_4 - k_5 * \lambda_0 + k_1^{**} k_5} \tag{2.35}$$

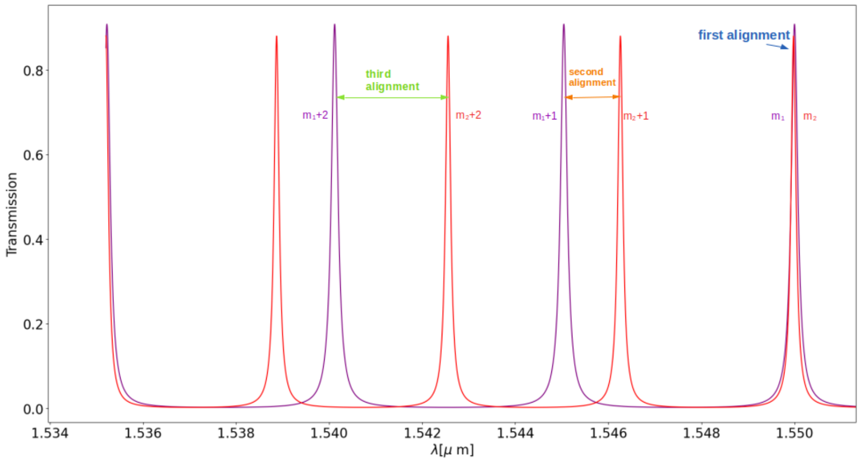

Figure 2.6: Resonances alignment of the resonances of the rings.

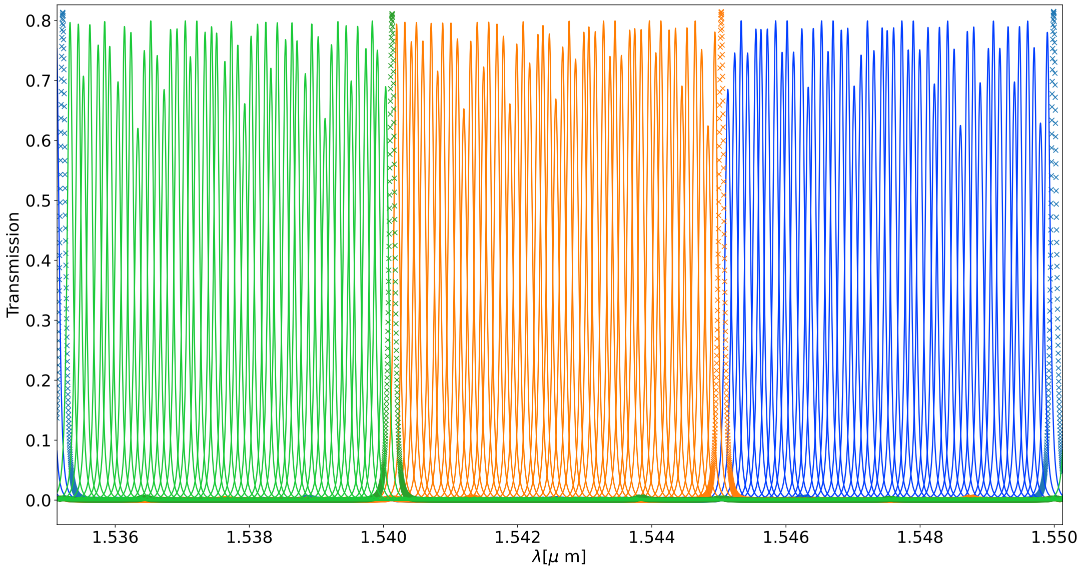

Figure 2.7: Resonances scanning.

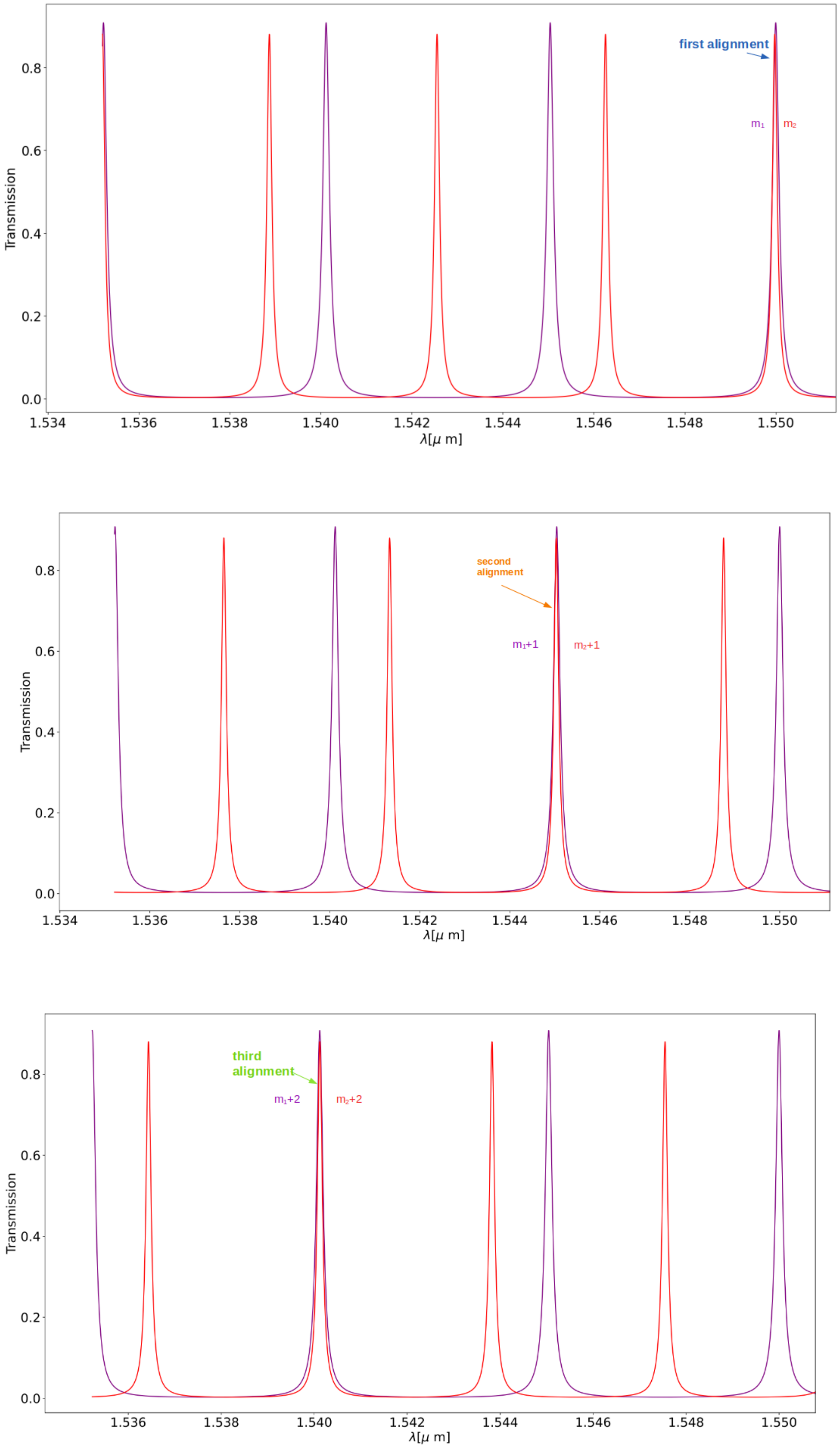

Figure 2.8: Alignments of the resonances of ring 1 and ring 2: first alignment (a), second alignment (b) and third alignment (c).

2.7 Results and discussion

The equations derived and discussed in Sections 2.3 and 2.6 can be used to simulate a system consisting of two cascaded ring resonators. Specifically, the orders of resonances for the two ring resonators have been searched for in the range of integers [240, 340]. The results shown in this paper refer to the resonance orders $m_1 = 240$ and $m_2 = 320$. Such relatively high values can guarantee as a consequence a higher bandwidth but at the same time do not negatively affect the footprint of the overall device. Using the refractive indices reported in Table 2.1 and a central wavelength $\lambda_0 = 1.55\mu$m in Equations 2.29 and 2.30, the lengths of the rings can be retrieved, respectively $l_1 = 230$ μm and $l_2 = 300$ μm. Along the full length of the rings, the length of PCM segments has been fixed to 300 nm (green parts of right panel in Fig. 2.2). The design has been developed with a resolution lower or equal to 0.1 nm. In Fig. 2.8 the results of the procedure of alignment of the resonances for the two rings is shown; specifically, the total optical power defined as the product of the transmission to the drop port of each ring is reported. For the specific case, the smallest co-prime numbers of m_1 and m_2 are 3 and 4; this corresponds to having 3 resonances for the first ring and 4 for the second in the bandwidth range, respectively. Once aligned the first resonances to the chosen central wavelength λ_0, the maximum number of subsequent alignment is limited by the smaller co-prime number between m_1 and m_2 (3, in this case): as a matter of fact, three alignment procedures can here be performed. The alignments are performed by changing the amount of crystalline and amorphous PCM in the second ring resonators (η^*_{a2} in Eq. 2.32), that is digitally achieved by thermally switching on/off the metal pads on top of the PCM regions. For each alignment, the wavelength scan is eventually performed by changing the amount of crystalline and amorphous PCM on ring 1 ($\tilde{\eta}^{scan}_{a1}$ in Eq. 2.34) and ring 2 ($\tilde{\eta}^{scan}_{a2}$ in Eq. 2.35). In Fig. 2.10 the result of the implemented algorithm for the scanning procedure is reported for m_1 and m_2; in particular, the product of the transmission for the two rings is large both in the alignment of the resonances (blu, orange and green bold peaks) and among them, where the swipe of the wavelength is performed by changing the phase of the PCM segments of the first ring. The non-uniformity, defined as the ratio between the highest and the lowest values of the peaks in between the resonances, is at maximum 1.64 dB.

A potential concern is the presence of back-reflections introduced by the PCM segments due to the local refractive-index discontinuities at each interface. However, each discontinuity is expected to be weak, hence the reflection from a single segment is small. Significant reflection would only arise if the interfaces contributed coherently, i.e., if the PCM segments were arranged periodically so as to form an effective Bragg grating. In that case, a strong response would be expected only when operating close to the corresponding Bragg wavelength set by the segment spacing. Therefore:

- by avoiding a strictly periodic placement of PCM segments;
- if periodicity is present, by operating away from the Bragg condition;

reflections do not add constructively and are expected to remain negligible.

From a numerical point of view, the percentage of amorphous and crystalline PCM fraction that is needed to be changed in order to align the resonances of the two ring resonators is 0.003% for the first alignment, 0.03% for the second alignment and 0.06% for the third alignment. Considering the total length of ring 2 and the length of the PCM segments, these fractions correspond to the change in phase of a total number of PCM segments (x_2) on ring 2 equal to 2, 30 and 57, respectively. For the wavelength scanning, the percentages of PCM to be converted from crystalline to amorphous both in ring 1 and ring 2 are $\sim$ 0.1%, corresponding to $\sim$ 80 PCM segments that are supposed to change their phases in order to scan the wavelength distance in between the resonances in the bandwidth, both on ring 1 and ring 2. In particular, for ring 2 around 100 segments are expected to change phase in order to perform the scanning while for ring 1 they are expected to be $x_1 \sim 85$.

In Fig. 2.9 the scatter plot of the number of PCM segments to be switched on ring 2 (x_2) as a function of the number of segments to be switched on ring 1 (x_1) in the processes of alignment and wavelength scanning is reported. The different colours identify the several alignment procedures between the resonances of ring 1 and ring 2, while the scanning procedure for each alignment is highlighted with arrows. After choosing appropriate values for x_2 and x_1 in order to align the resonances, a linear trend between x_2 and x_1 can be noticed. A linear fit $x_2 = b_0 + b_1 \times x_1$ has been performed for each curve. For the first alignment, the fitting coefficients are $b_0 = 2.1414$ and $b_1 = 1.3299$; for the second alignment, $b_0 = 31.1032$ and $b_1 = 1.325$; for the third alignment, $b_0 = 57.8466$ and $b_1 = 1.3326$.

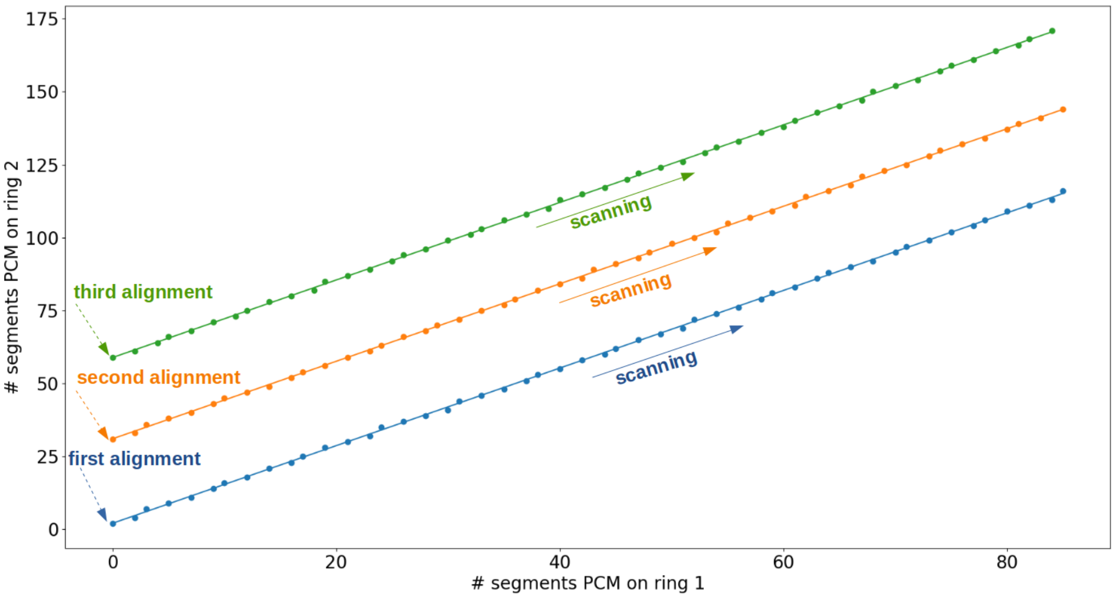

Figure 2.9: Scatter plot of the number of PCM segments on ring 1 and ring 2 in the alignment and scanning procedures.

After modelling the spectrometer, the effect of higher order terms in the refractive index expansion has been investigated. Specifically, the quadratic order terms (corresponding to the dispersion term) have been included. The implemented numbers are reported in Table 2.1 together with the refractive and group indices. Once introduced this effect in the design, the computed non-uniformity has been found equal to 1.32 and the maximum shift in wavelengths is 0.01 nm.

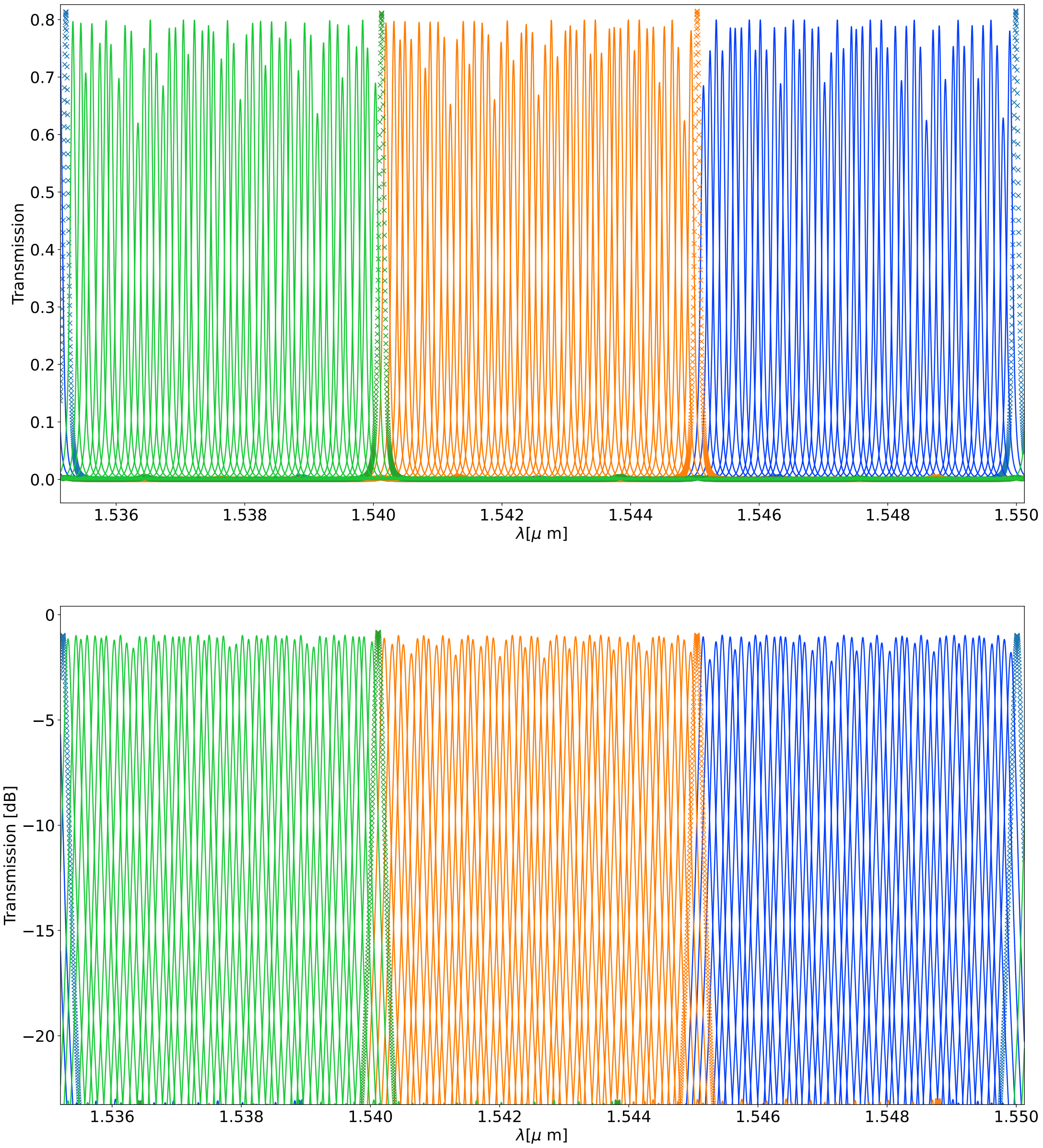

Figure 2.10: Wavelength scanning between resonances. The product of transmission outputs of the rings is reported in normal units (a) and in dB (b).

Chapter 3

Fourier-transform integrated spectrometer

In this chapter the description of a Fourier-transform spectrometer will be provided. Specifically, the architecture can be found in [80]; measurements on three different samples of this model have been performed as experimental laboratory part of the present PhD work.

3.1 Description of the design of the device

The numerical derivation and the equations holding as working principles of a Fourier-transform spectrometer are described in Chapter 1, at Section 1.3.2.1. Moreover, in Appendix A.1 the Fourier relationship between the detected output interferogram $I(p)$ as a function of the optical path difference (OPD) p and the input spectral intensity $I(\bar{\nu})$ as a function of the spatial frequency $\bar{\nu}$ is reported. The main key point in designing an integrated Fourier-transform spectrometer is the way the optical path difference in the interferometer branches can be produced. In fact, it is possible to classify Fourier-transform integrated spectrometers into two main categories, according to the way the optical path difference is achieved in the device:

- analog Fourier-transform spectrometers: the OPD varies continuously, typically implementing by phase-shifters exploiting the thermo-optic or electro-optic effect;
- digital Fourier-transform spectrometers: the OPDs are discrete and predefined and they can be selected according to a network of optical switches. Typically, Mach-Zehnder interferometers are used for such scope, but alternatives can be found (e.g. micro-ring resonator switches [38], Micro-Electro-Mechanical Systems (MEMS)[179], electro-optic directional couplers [180] or PCM [181]).

Thermo-optic and electro-optic effects can be used both in digital and analog integrated spectrometers, though for different scopes. In Tab. 3.1 a resume on the motivations of the use of thermo-optic and electro-optic effects in analog and digital integrated spectrometers is reported in order to summarize the main features and, as a consequence, justify the different architectures.

Table 3.1: Compact comparison between analog and digital Fourier-transform spectrometers.

	Analog FTS	**Digital FTS**
TO/EO effect used for:	Continuous phase tuning	Binary ON/OFF switching
Result	Continuous OPD	Discrete OPD
Control type	Variable voltage/current	Digital state (0/1)
Optical function	Phase modulation	Path selection
Main benefits	High-resolution, tunable	Compact, stable, reconfigurable

In Fig.3.1 the block diagram of a digital Fourier-Transform InfraRed (dFTIR) spectrometer is reported, together with a schematic layout of a 64-channel version in which the outputs of the

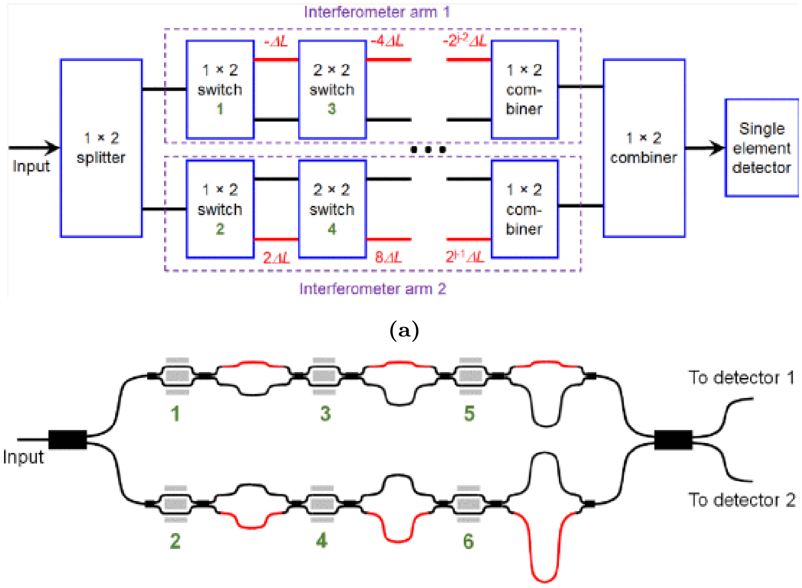

(a)

(b)

Figure 3.1: Block diagram and schematic representation of a digital Fourier-Transform InfraRed (dFTIR) spectrometer. In red: waveguide segments with different varying lengths (not in scale). In green: 1×2 or 2×2 switches [182].

last combiner are detected by two different detectors [182]. In fact, such configuration improves the SNR by a factor $\sqrt{2}$ if compared to the configuration in which a 2 ×1 combiner is used with one detector (as in Fig. 3.1, top panel) [183]. The present work focuses on the analog Fourier-transform spectrometer described by [80][1]. The input light signal is equally divided into the arms of a Michelson Interferometer (MI) through a MultiMode Interferometer coupler (MMI) [2]. Each arm of the MI is composed of several waveguide segments of different lengths. Specifically, the spiral waveguides are active components integrated into the circuit to increase the achievable optical path difference, hence improving the spectral resolution.

The core optical elements of the integrated FTS described in [80] are Waveguide Bragg Grating Resonators (WBGRs), which act as tunable reflective components within the interferometer. The theoretical responses of a uniform and a phase-shifted Bragg grating are shown in Fig. 3.2. The uniform Bragg grating exhibits the typical stopband behavior due to strong reflection around the Bragg wavelength λ_{Bragg}, whereas the phase-shifted Bragg grating introduces a narrow notch within the stopband as a result of the intentionally inserted phase discontinuity. In Fig. 3.3 the phase-shifted WBGR implemented in the layout is reported as a reference.

The spirals interconnect the WBGRs through two configurations - small and large spiral waveguides - corresponding to different optical path lengths. In the design of the device, a minimum ODP between the arms of the interferometer is fixed and defined as ΔL. The small and large spirals are 0.5 ΔL and 4ΔL long, respectively. Moreover, in order to achieve a maximum OPD equal to 64 ΔL an additional long spiral is added in the lower arm of the interferometer (Fig. 3.4).

The layout of the chip has been designed according to the Cornerstone guidelines `https://cornerstone.sotonfab.co.uk/mpw/process-design-kit/`; in particular, the active measurements are designed to be performed using a DC probe array in which the distance between the pins is 100 μm.

---

[1] The adjective "digital" given in the title of the paper refers to the control/sampling and to the data processing, rather than to the physical mechanism generating the optical path difference

[2] MMIs are photonic devices designed to split or combine optical signals by supporting the propagation of multiple modes that interfere within the multimode region. They rely on the optical self-imaging effect: in a multimode waveguide or fiber, an input optical field can form self-images at specific propagation distances as a result of the coherent interference of guided modes [184]. This effect has been extensively exploited in photonic integrated circuits, following the first seminal work by Soldano and Pennings in 1995 [185].

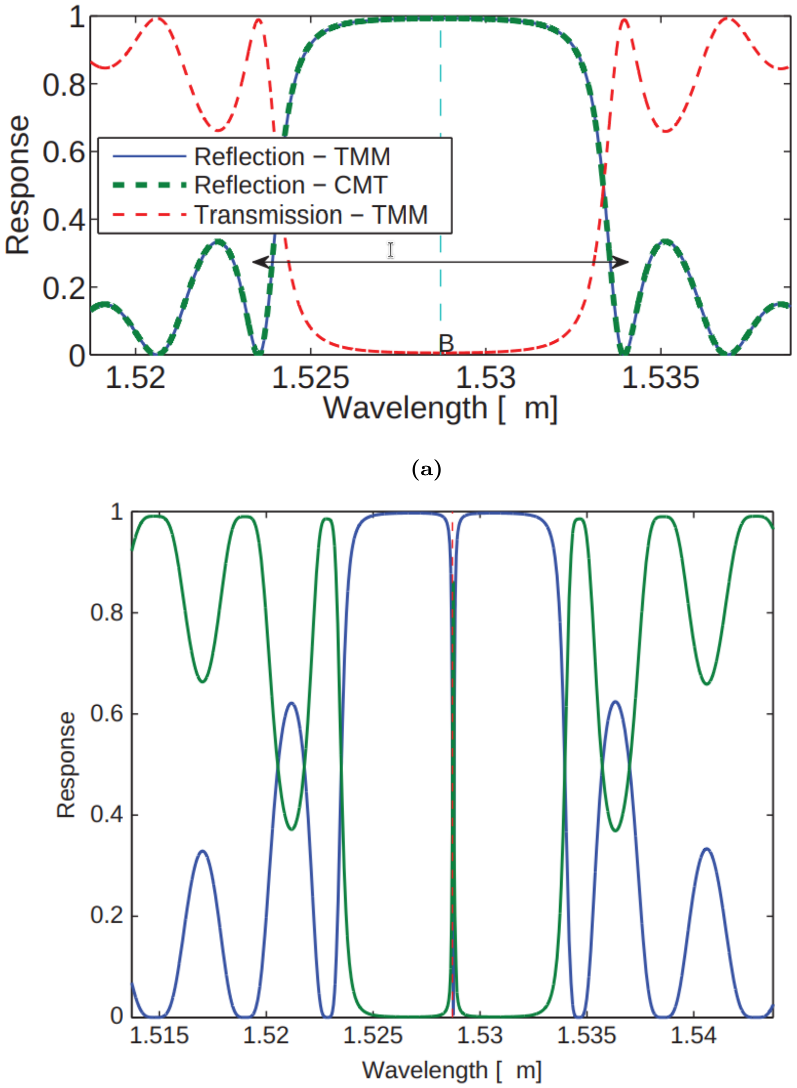

(a)

(b)

Figure 3.2: Theoretical spectral response of a uniform (top panel) and a phase-shifted (bottom panel) Bragg grating. In the caption, TMM stands for Transfer Matrix Method, CMT for Coupled Mode Theory. Figures from [186].

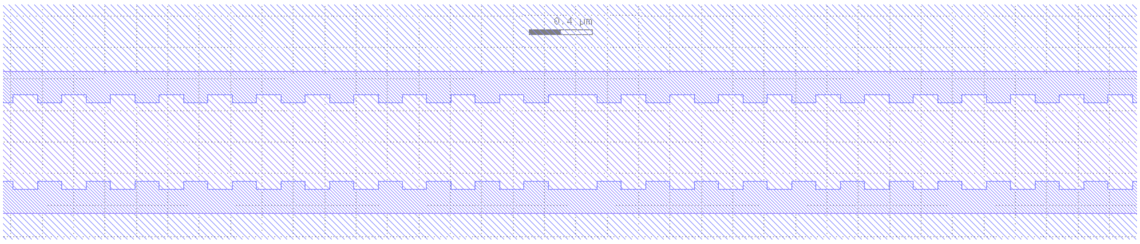

(a)

Figure 3.3: WBGR as in the layout file.

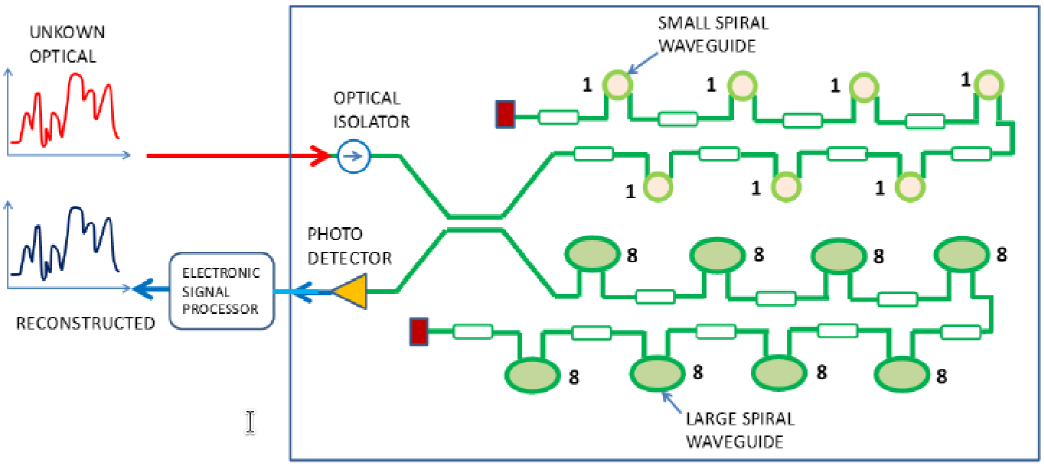

Figure 3.4: Schematic representation of the digital Fourier-Transform InfraRed described in [80].

3.2 Experimental measurements

The experimental measurements have been performed at the laboratory of the University of Southampton. They consisted in mearusing the output power of light in the devices fabricated according to the layout shown in Fig. 3.7. Light emitted by a laser with wavelength $\lambda = 1550\ nm$ has been guided via fiber optic cables onto the photonic integrated circuit. The coupling between optic cables and PIC has been achieved through the presence of grating couplers. Two different kinds of measurements have been performed:

- passive measurements: the output powers have been measured without applying any changes on the optical paths;
- active measurements: the output powers have been measured applying an external voltage. In fact, by means of the thermo-optical effect, different optical paths are achieved and the output depends on the applied external field.

The presence of grating couplers at the input and output of each device is crucial, as they enable efficient coupling between the optical fiber and the on-chip waveguides. A proper understanding of their operating principle is therefore essential to ensure accurate measurements; we refer to the description provided by Kita *et al.* [187] for further details.

A grating coupler consists of a periodic structure that diffracts the incoming light and radiates it upward (or downward) toward an external optical interface, typically a single-mode fiber. In particular, the grating lines are oriented at an angle with respect to the waveguide propagation direction, enabling phase-matched diffraction out of the photonic chip plane.

The coupling condition follows the first-order diffraction equation:

$$n_{\text{eff}} - n_{\text{clad}} \sin\theta = \frac{\lambda}{\Lambda}, \tag{3.1}$$

where n_{eff} is the effective index of the guided mode, n_{clad} is the refractive index of the cladding (usually air or SiO_2), θ is the coupling angle with respect to the chip normal, λ is the operating wavelength, and Λ is the grating period.

By choosing a suitable Λ and duty cycle, the grating can be optimized to maximize coupling efficiency for a desired wavelength and fiber alignment angle. However, due to their diffractive nature, grating couplers typically exhibit a limited bandwidth and polarization sensitivity. These aspects must be taken into account while performing measurements.

The layout of the photonic integrated circuit measurements have been performed on is shown in Fig. 3.7. It consists of four copies of the same devices, each copy is referred to according to the position on the PIC (top left, top right, bottom left, bottom right).

The devices fabricated on the chip can be listed as:

1. normalization waveguides

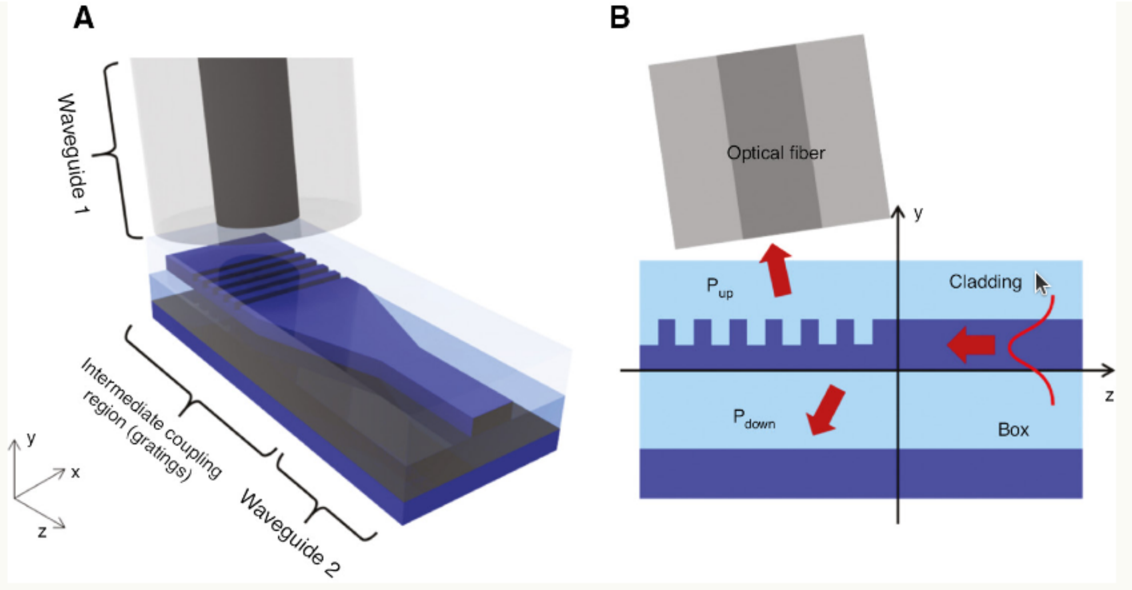

(a) Schematic operational principles of fiber optics and grating couplers coupling. *Left panel*: 3D view; *right panel*: front view.

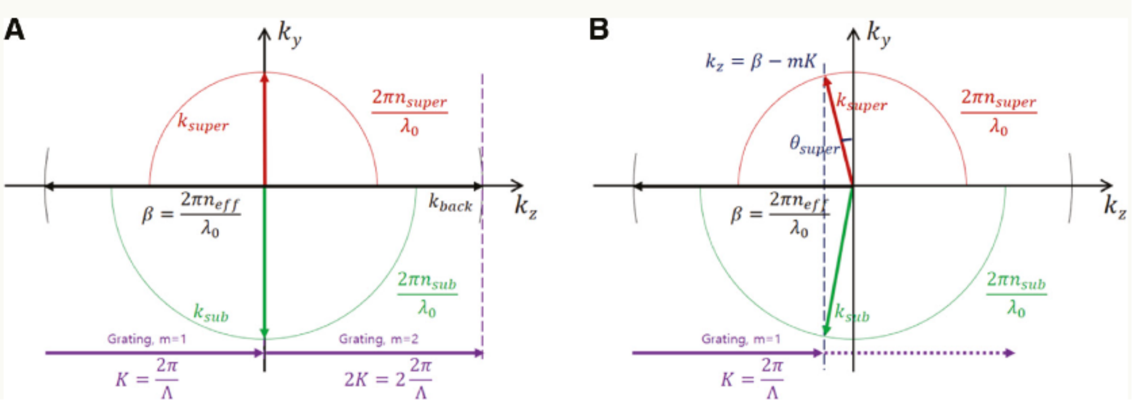

(b) Grating coupler: wavevector representation of the Bragg condition. *Left panel*: ideal perfectly vertical operation. In this condition, the second-order diffraction (m=2) is generated, with increased back-reflection. *Right panel*: off-normal operation. In this case, only the first-order diffraction (m=1) is generated and the back-reflection is reduced. The colours black, purple, red and green for the arrows indicate the propagation constant in the waveguide region, the reciprocal lattice vector of the grating, the wavevector of the upward-diffracted wave and the wavevector of the downward-diffracted wave, respectively.

Figure 3.5: Coupling between optic fiber and waveguides on a PIC via grating coupler. Figures from [187].

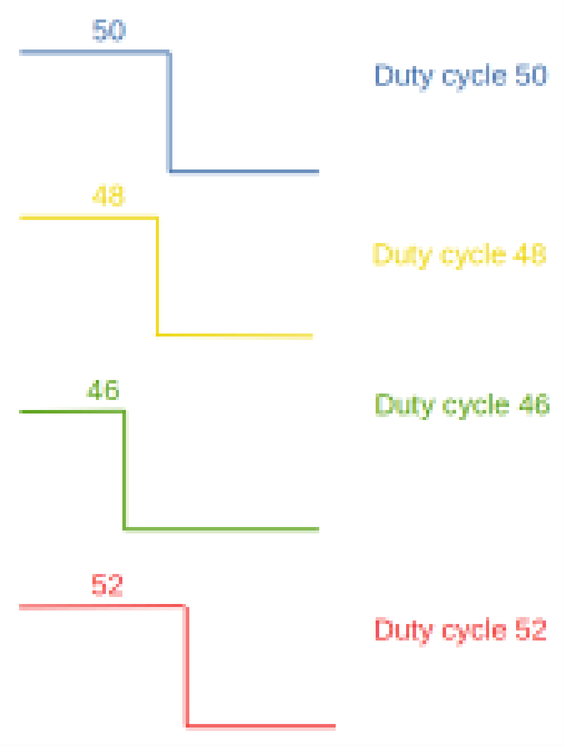

(a)

Figure 3.6: Explanation of the duty cycle numbers inserted as in the layout.

2. grating couplers (GC): they are labelled as DC46, DC48, DC50, DC52 and DC54;
3. small spirals (SS): they are labelled as SS1, SS2, SS3, SS4, SS5, SS6 and SS7;
4. large spirals (SL): they are labelled as SL1, SL2, SL3, SL4, SL5, SL6, SL7 and SL8;
5. phase shifter PS: they are labelled as DC46, DC48, DC50, DC52 and DC54;
6. phase shifter with short heater(PS_SH);
7. phase shifter with long heater(PS_LH).

The acronym DC stands for *duty cycle* and the numbers indicate the percentage of the length of consecutive steps over one whole period in a grating (see Fig. 3.6).

The layout file (.gds) is visualized using klayout.

3.2.1 Passive measurements

3.2.1.1 Sample 1: first run of fabrication

The first run of fabrication has been performed in 2023-2024 by Cornerstone (Southampton, UK). In particular, a chip in SOI technology has been fabricated as from the layout reported in Fig. 3.8 in 2023 and according to the Cornerstone 220 nm SOI technology back then. Details are here reported as a reference; they can be access online[3]:

- technology details
  - Si etch depths: 70 nm, 120 nm & 220 nm;
  - TiN based thermal phase shifters;
  - 4 implantation layers for active device batches;

---

[3] `https://www.cornerstone.sotonfab.co.uk/wp-content/uploads/2023/07/CORNERSTONE-Brochure-digital.pdf`

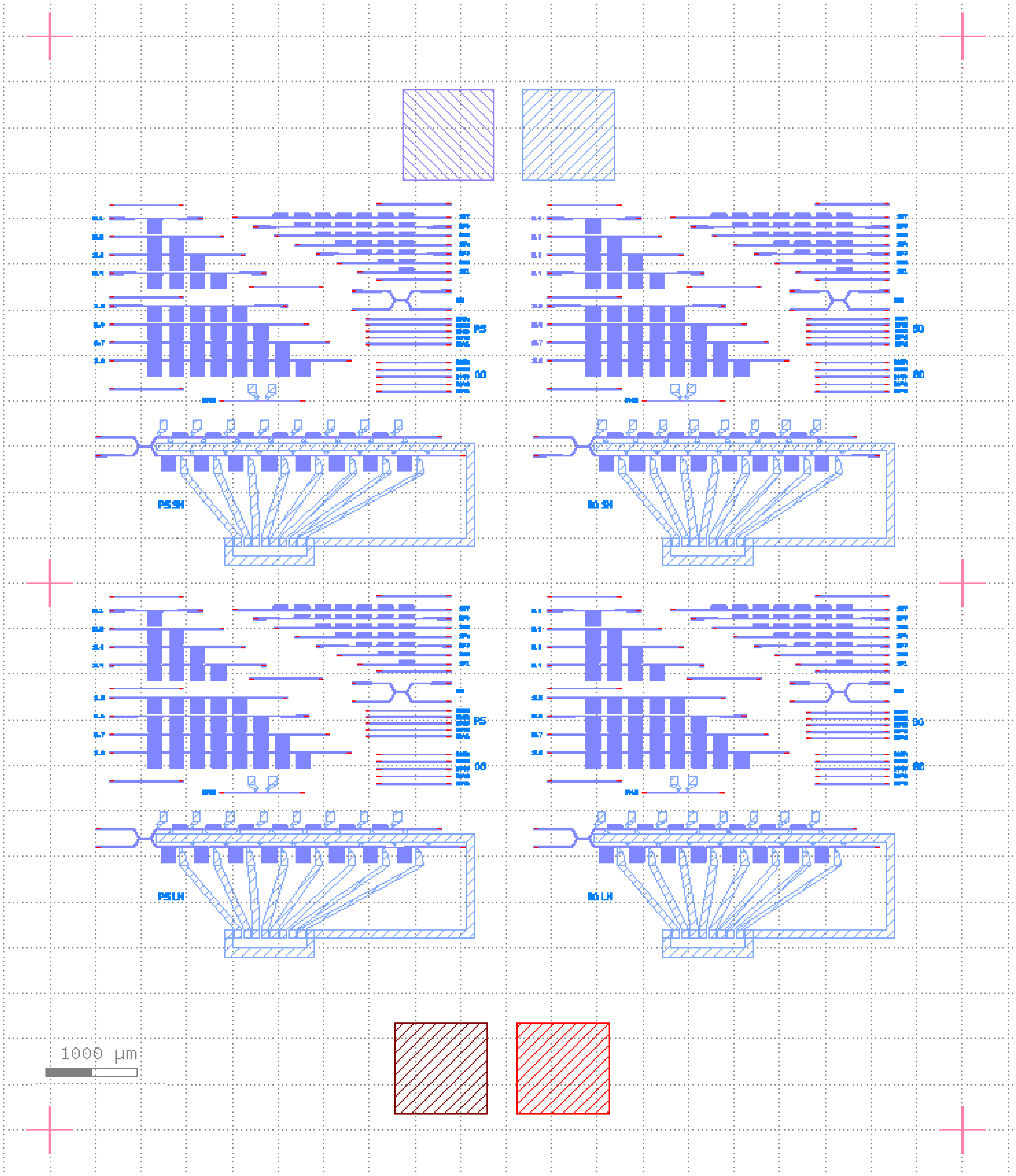

(a)

Figure 3.7: Layout of the chip. On the left side, the phase-shifters (i.e. phase-shifted Bragg gratings) are covered with short (top) and long (bottom) heaters. On the right side, uniform Bragg gratings are fabricated, with short (top) and long (bottom) heaters.

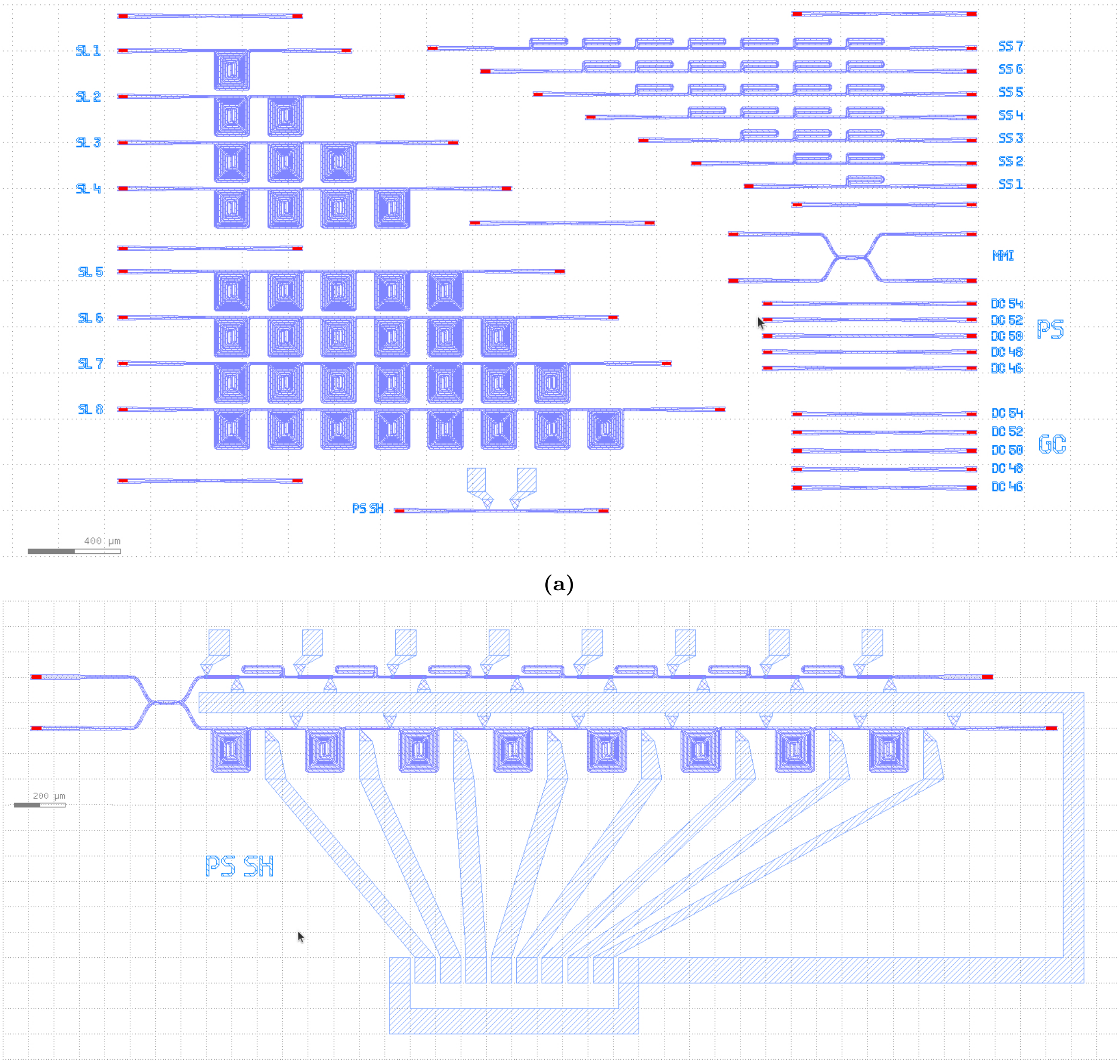

(a)

(b)

Figure 3.8: Measured devices. *T*op panel: zoom of the top left quadrant. *B*ottom panel: full spectrometer as in the top left quadrant.

  - high resistivity handle wafer for improved RF performance (750 ohm.cm);

- performance (TE single mode $\lambda = 1.55$ μm):
  - rib waveguide propagation loss: < 3 dB/cm
  - Strip waveguide propagation loss: < 4 dB/cm
  - Grating coupler loss: 5-6 dB/grating
  - Phase shifter efficiency (MZI): < 20 mW/π
  - Modulator performance (1.8 mm long MZI based carrier depletion):
    - speed @ 2 V dual drive:$>$ 40 Gb/s;
    - insertion loss @ 2 V dual drive: < 5 dB;
    - extinction ratio @ 2 V dual drive:$>$ 3 dB;
- logistics: design area options: 11.47×4.9 mm^2 / 5.5×4.9 mm^2

Eventually, in 2024 a 1 μm thick SiO_2 layer has been deposited on the same chip in order to verify the response of the phase. In the following figures, the comparison between the pre- (green curves) and post- (blue curves) silicon dioxide film deposition are reported. It can be noted that:

- the transmitted powers are lower than pre- deposition case;
- in the phase shifters, the expected double-well behaviour becomes apparent after the deposition of SiO_2. This is because the original design on which the layout was based assumed the presence of a SiO_2 layer on top of the shifters.

Measurements have been taken with an angle read on the inclinometer equal to 20°, i.e. 10° from the normal (see Appendix A.4 for details on the setup). In Figs. 3.9-3.10-3.11 and 3.12 some pictures of the setup and chip used in the first round of measurements are reported.

In Fig. 3.13, the output powers of the grating couplers are reported before and after SiO_2 deposition. As expected from the design, we observe a bell-shaped spectral response centered at 1550 nm. The reduced output power after deposition (blue curves) can be attributed to the additional SiO_2 layer and to differences in sample conditions, such as surface cleanliness and contamination.

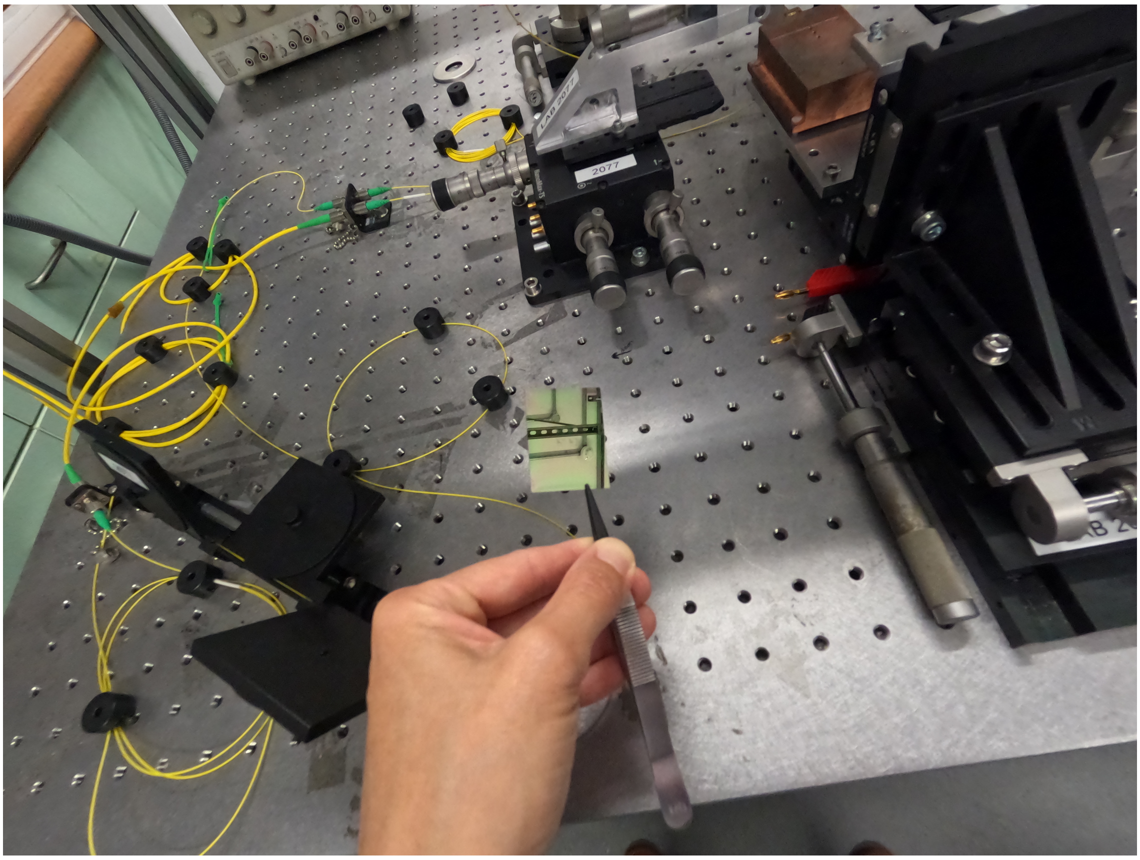

(a)

(b)

Figure 3.9: Chip produced during the first round of fabrication.

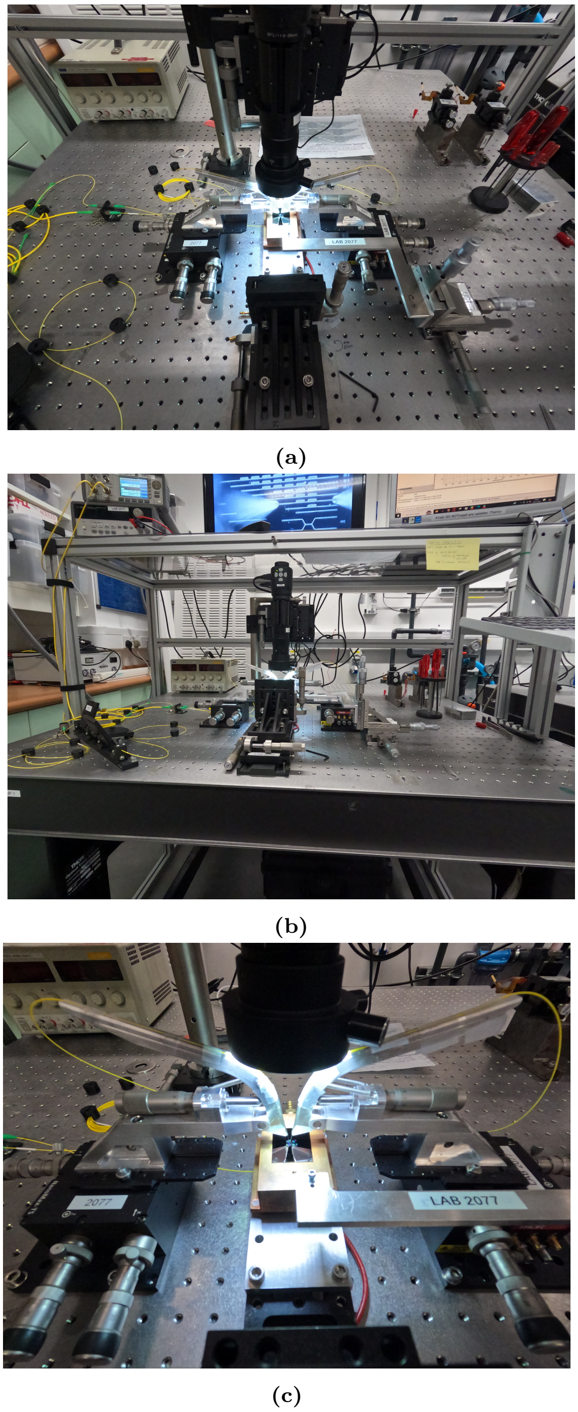

Figure 3.10: Setup view of the first round of measurements: front views.

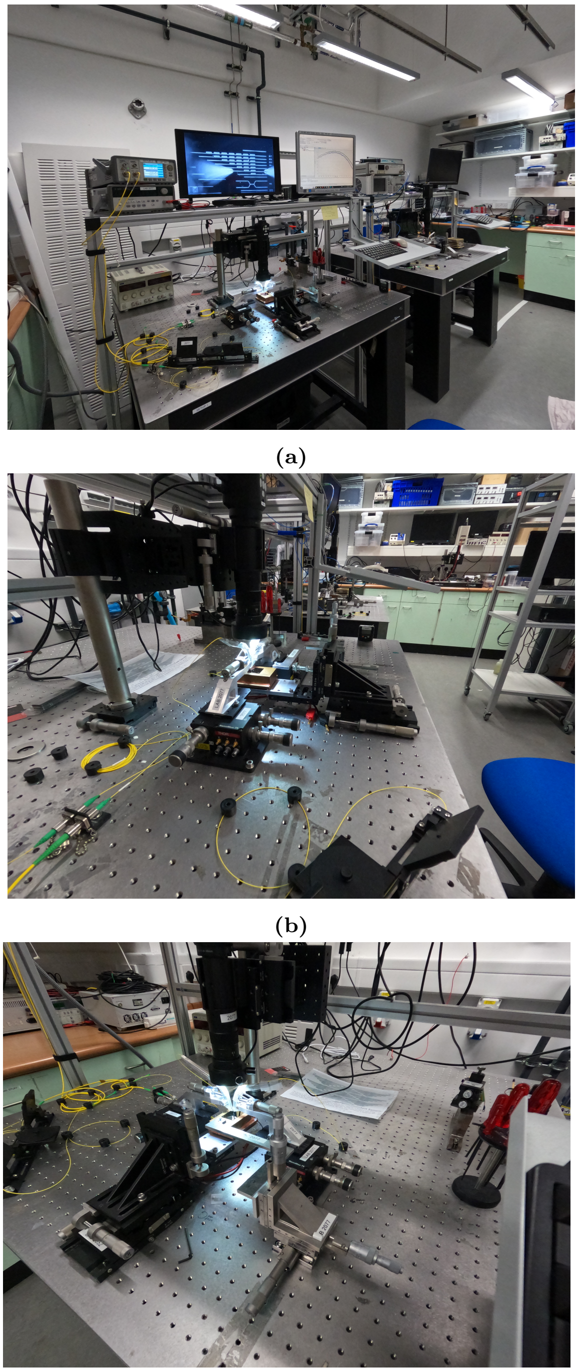

(a)

(b)

(c)

Figure 3.11: Setup view of the first round of measurements: side views.

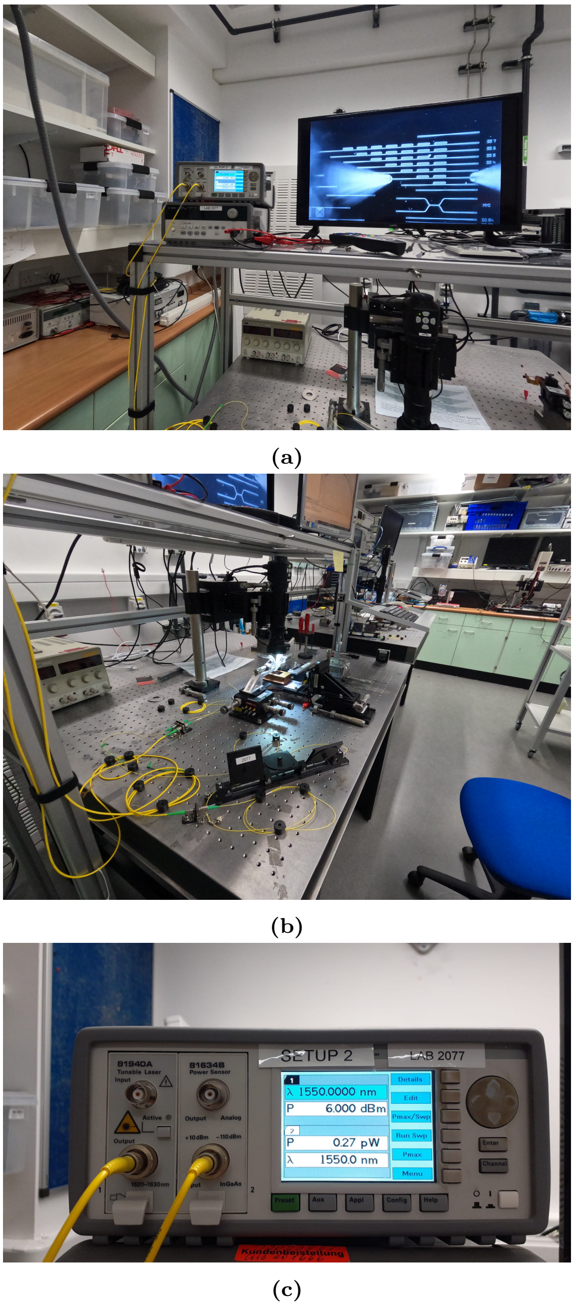

Figure 3.12: Laser and polarizer used in the measurements.

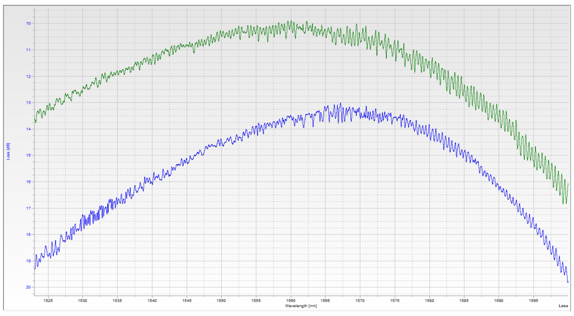

(a) Grating coupler GC DC 46.

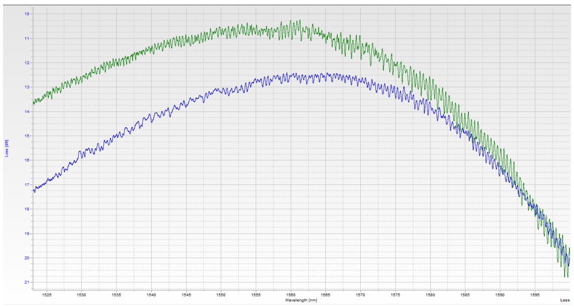

(b) Grating coupler GC DC 48.

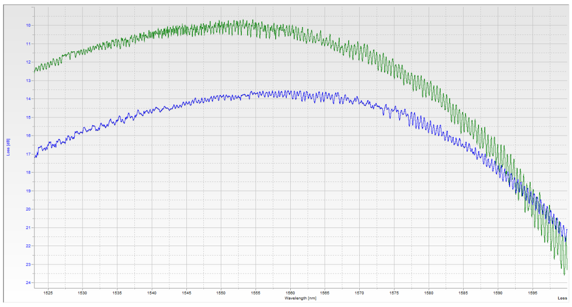

(c) Grating coupler GC DC 50.

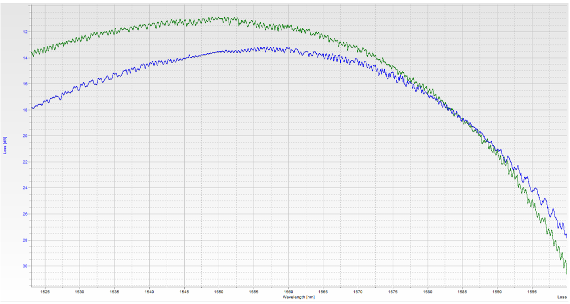

(d) Grating coupler GC DC 52.

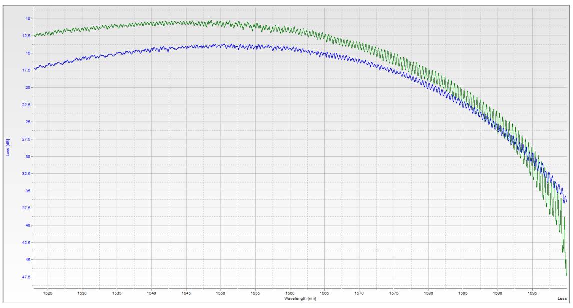

(e) Grating coupler GC DC 54.

Figure 3.13: Grating couplers output powers: first round of fabrication, pre and post SiO_2 deposition.

In Fig. 3.14, the output powers of the short spirals are reported before and after SiO_2 deposition. For Spirals 1–4, a bell-shaped spectral response is observed, as expected. As for the grating couplers, SiO_2 deposition leads to a reduction in the output power. However, for the longer short spirals (i.e., as the spiral length increases), both the spectral shape and the overall trend of the curves before and after deposition are not consistent with expectations. For Short Spirals 6 and 7 the silica deposition increased the output power detected.

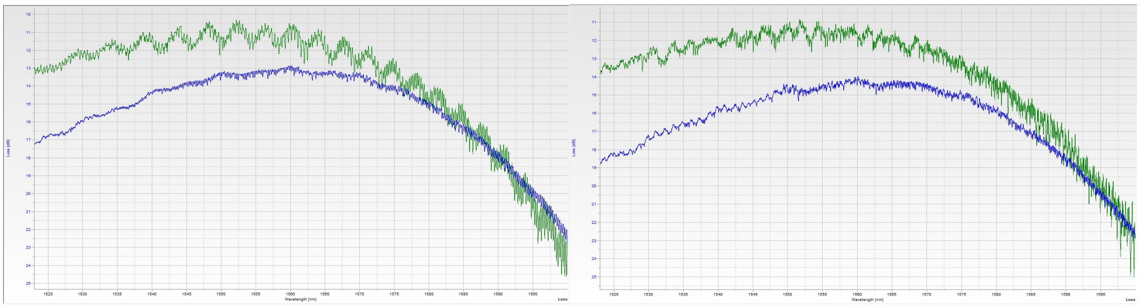

(a) Short spiral (SS) 1.

(b) Short spiral (SS) 2.

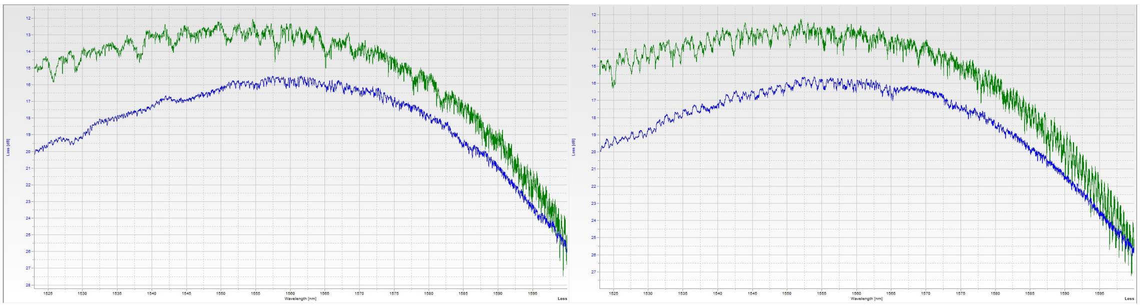

(c) Short spiral (SS) 3.

(d) Short spiral (SS) 4.

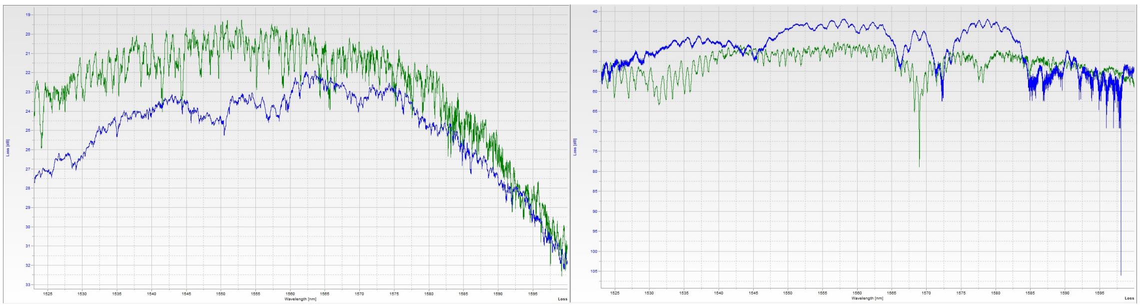

(e) Short spiral (SS) 5.

(f) Short spiral (SS) 6.

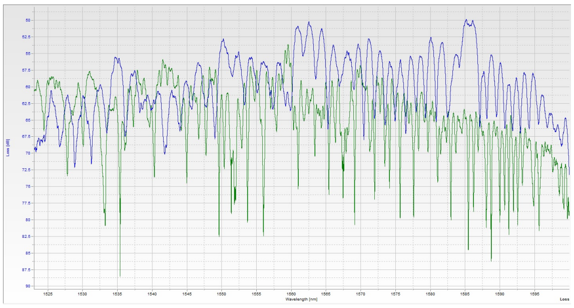

(g) Short spiral (SS) 7.

Figure 3.14: Short spirals output powers: first round of fabrication, pre and post SiO_2 deposition.

In Fig. 3.15, the output powers of the long spirals are reported before and after SiO_2 deposition. As expected, longer spirals generally exhibit higher loss and reduced SNR. However, the degradation is not uniform across devices: some long spirals still show an identifiable spectral shape, whereas others yield strongly distorted and noisy outputs.

Interestingly, for Long Spiral 4, SiO_2 deposition results in an improved spectral shape and higher output power. Overall, these results indicate that, besides the increased optical path length, layout- and device-dependent features (e.g., bend loss, discontinuities etc), as well as measurement conditions (e.g., fiber alignment and polarization state), can play a significant role. This device-to-device variability is consistent with fabrication tolerances becoming increasingly critical as the optical path length increases.

Both the short- and long-spiral measurements motivate a redesign of the spiral layout to reduce losses and improve the transmitted power. For instance, larger bend radii and fewer discontinuities could improve robustness and measurement repeatability.

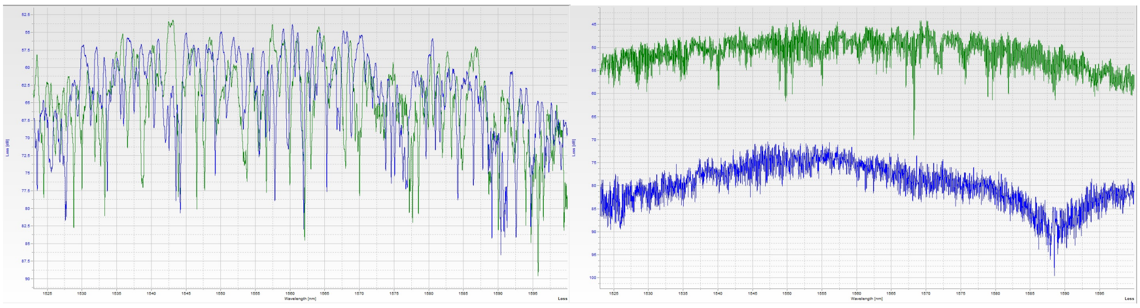

(a) Long spiral (LS) 1. **(b)** Long spiral (LS) 2.

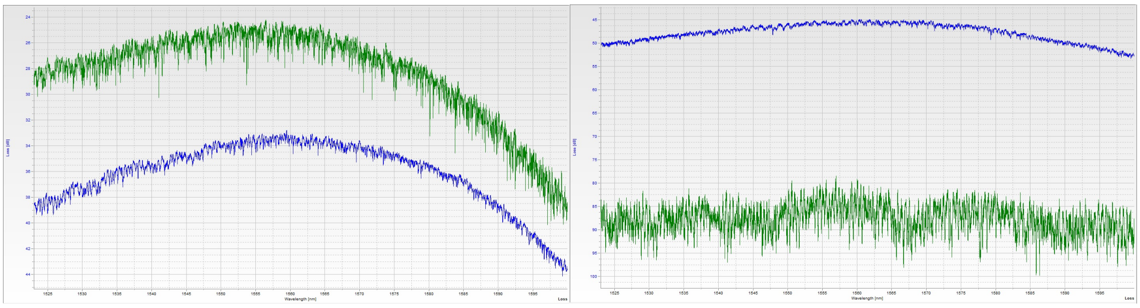

(c) Long spiral (LS) 3. **(d)** Long spiral (LS) 4.

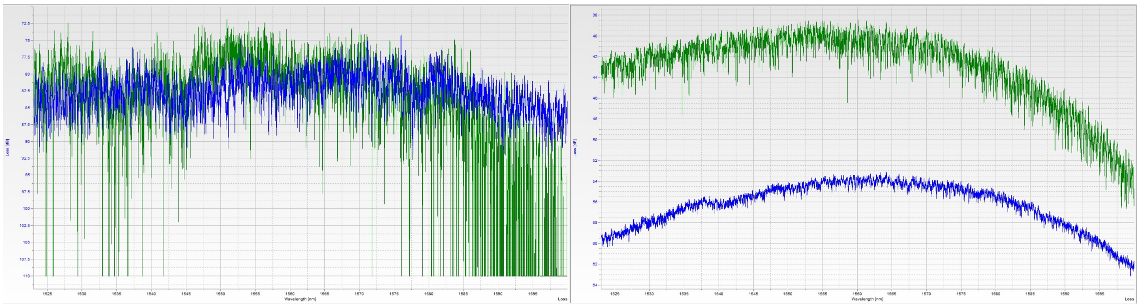

(e) Long spiral (LS) 5. **(f)** Long spiral (LS) 6.

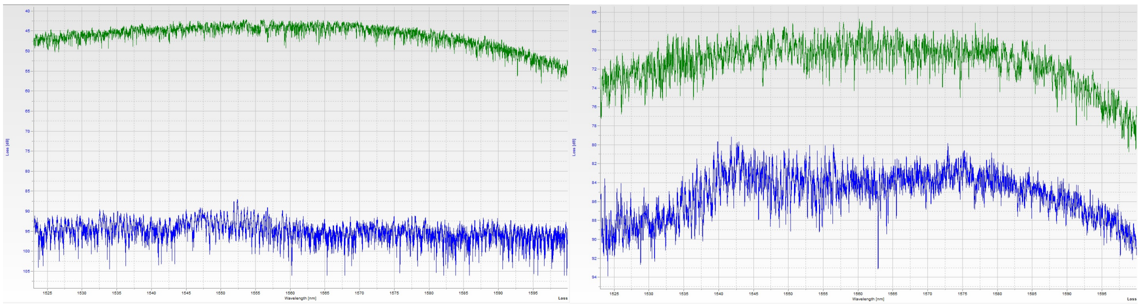

(g) Long spiral (LS) 7. **(h)** Long spiral (LS) 8.

Figure 3.15: Long spirals output powers: first round of fabrication, pre and post SiO_2 deposition.

In Figs. 3.16 the measurements of the output, pre- and post- silica deposition, are reported for the phase shifters (Bragg gratings). It can be noted the the silica deposition allowed to achieved the expected double dips shape of the output. In fact, the design has been performed under the hypothesis of a SiO_2 on top of the devices on the photonic circuit.

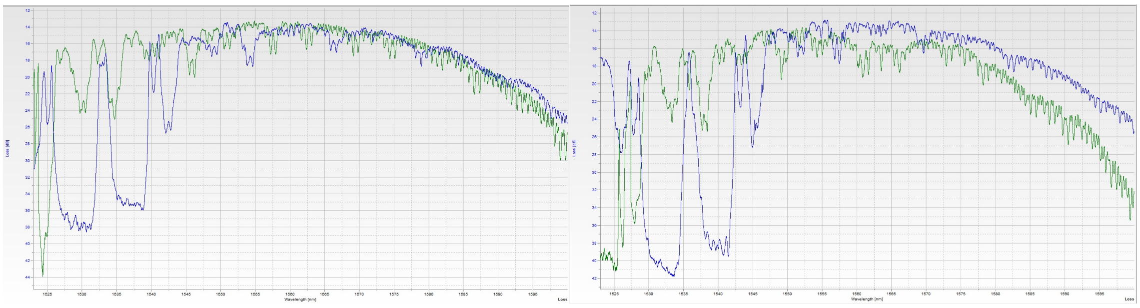

(a) Phase-shifter (PS) DC 46.

(b) Phase-shifter (PS) DC 48.

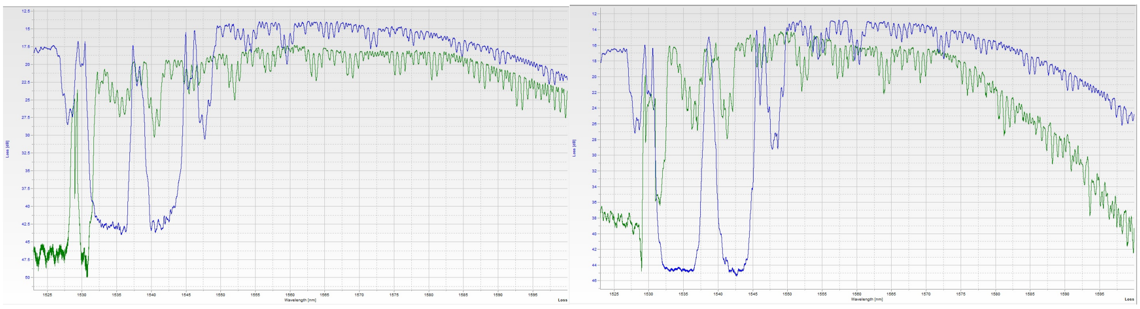

(c) Phase-shifter (PS) DC 50.

(d) Phase-shifter (PS) DC 52.

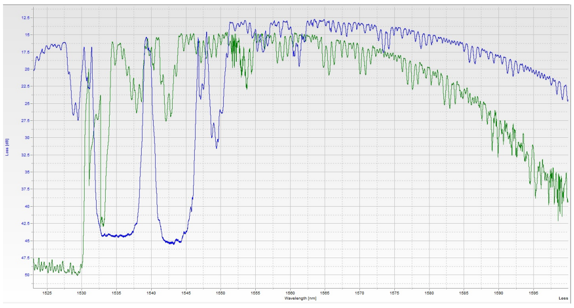

(e) Phase-shifter (PS) DC 54.

Figure 3.16: Phase-shifters: first round of fabrication, pre and post SiO_2 deposition.

In Fig. 3.17 the ouput powers for the phase shifter with the short heater in the pre- and post-SiO_2 deposition are shown. As in Figs. 3.16, the behaviour of the phase-shifter has achieved the expected phase-shifted Bragg gratings shape after SiO_2 deposition. However, differently from the phase-shifters shown in Fig. 3.17, the trend here is noisy.

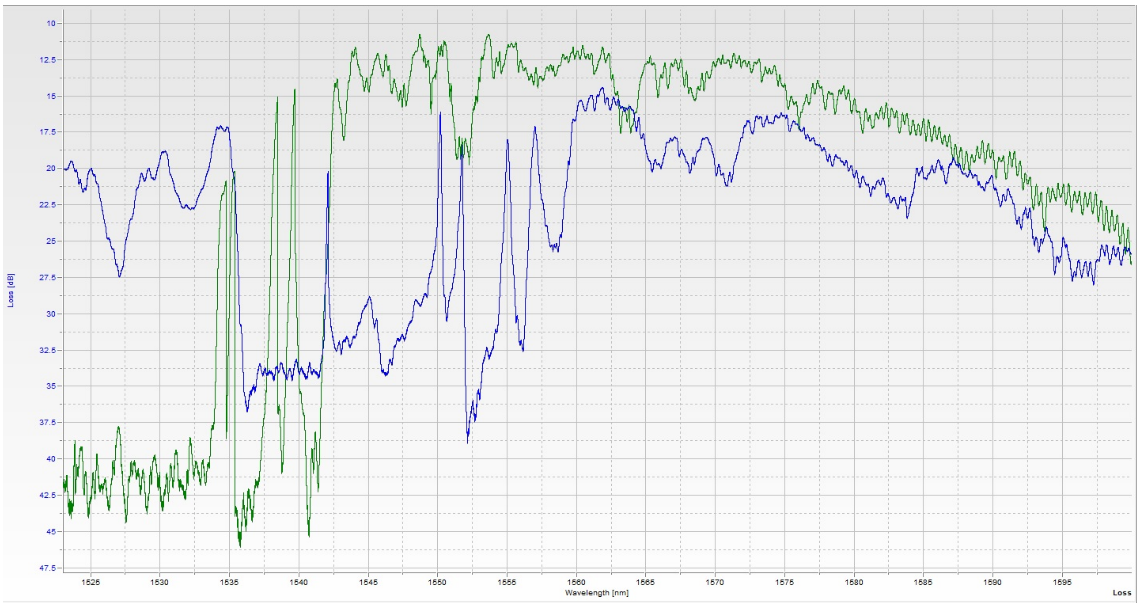

Figure 3.17: Phase-shifter with short heater (PS-SH): first round of fabrication, pre and post SiO_2 deposition.

3.2.1.2 Sample 2A a Sample 2B: second run of fabrication

In the second run of fabrication, the new e-beam facilities at University of Southampton have been used. Details are here reported as a reference and they can be accessed on-line[4]:

- EBL system - JEOL JBX-8100FS G3
  - operating at 100 kV and 200 kV;
  - current range 100 picoamperes to 200 nanoamperes;
  - up to 200 megahertz scan speed;
  - substrate sizes up to 200 mm;
  - minimum feature size <10 nm;
  - 12 cassette autoloader;
  - 1.6 nm minimum spot size (at 100 kV);
  - high throughput mode: ± 20 nm overlay and stitching accuracy; data increment 0.5 μm;
  - high resolution mode: ±9 nm overlay stitching accuracy; data increment 0.05μm field size: 1×1mm at 100 kV; 0.5× 0.5mm at 200 kV
- EBL system - JEOL JBX-A9:
  - operating at 100 kV;
  - substrate size up to 300 mm;
  - semi-production manufacture;
  - high reproducibility;
  - high throughput;
  - 1×1mm field size.

With this new e-beam facility, two different samples of the layout shown in Fig. 3.7 have been fabricated[5]. The main difference between them consists in the deposition of SiO_2; indeed, a different machine has been used.

---

[4] `https://www.southampton.ac.uk/research/facilities/electron-beam-lithography-facility`

[5] The name of these two samples on the provided boxes are sample 1 and sample 2. They correspond to sample 2A and sample 2B in this work, respectively.

Scanning **E**lectron **M**icroscopy images of sample 2B have been provided by the staff (Fig. 3.18). They have been produced using the recently established SEM system - JEOL IT-800i with the following features:

- ultra-high resolution SEM optimised for semiconductors;
- 0.5 nm resolution;
- substrate sizes up to 200 mm;
- SEM supporter - link EBL design to SEM inspection map;
- 60 mm^2 real-time x-ray energy dispersive spectroscopy (EDS).

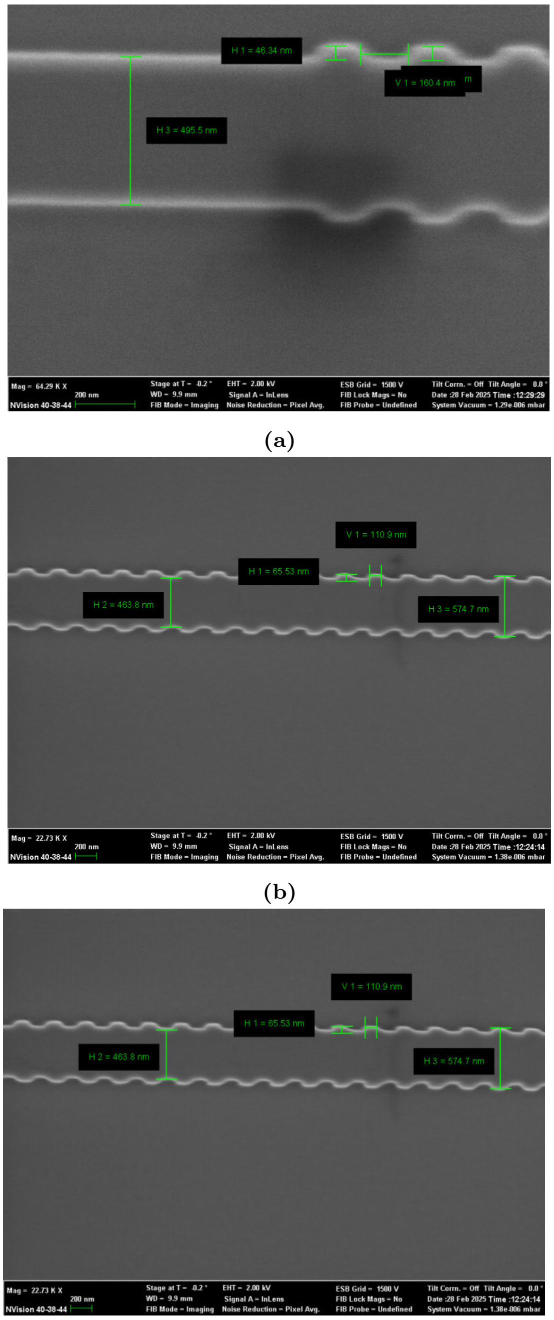

(a)

(b)

(c)

Figure 3.18: SEM images of the Bragg grating on the chip. Thanks to Dr. Aneesh Vincent Veluthandath (Optoelectronics Research Center, Southampton).

In the following, the results on the measurements for both samples are reported.

Sample 2A. Because of fabrication issues on the second (top right) and fourth (bottom right) copies of the spectrometer as in the layout, sample 2A consists of only the top left copy of the spectrometer as in layout Fig. 3.7. For this reason, measurements have been taken only on this part of the PIC. Moreover, because of time limitation, only the grating couplers (GC), the phase-shifters (PS) and the phase-shifter with short heater (PS-SH) have been passively tested. Results are shown in Figs. 3.19, Fig. 3.20 and Fig. 3.21, respectively.

Measurements have been performed with an angle of 8° respect to the normal. In Fig. 3.19 the output for the grating couplers, sample 2A are reported. Outside the main coupling band, the transmitted power becomes very low and the measured output power may show an apparent upturn accompanied by strong oscillations. This region is close to the measurement sensitivity limit and is more affected by the setup noise and parasitic interference effects e.g. due to the fiber-to-chip coupling. For this reason, the discussion is focused on the main coupling lobe around 1550 nm. In such wavelength region, the expected bell-shaped output powers have been retrieved for all the GC.

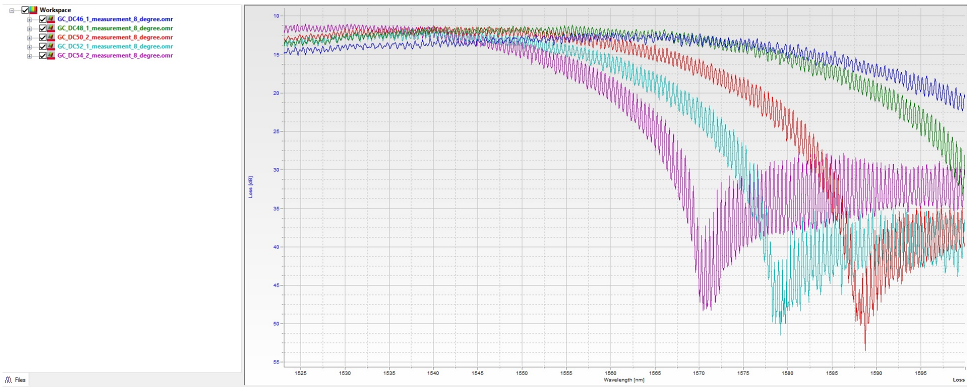

(a)

Figure 3.19: Grating couplers output powers: second round of fabrication, sample 2A.

For the phase-shifters, as shown in Figs. 3.20 and 3.21, unexpected behaviours can be noted. In fact, while the measurements show a stopband structure in the expected spectral region around 1550 nm, an additional notch is observed near the central wavelength. This suggests that the response is affected by additional interference mechanisms and/or fabrication-induced non-uniformities in the grating profile, which result in a more complex spectrum than the ideal two-notch behavior. Eventually, the stopband is not characterized by two clean minima but by multiple closely spaced features.

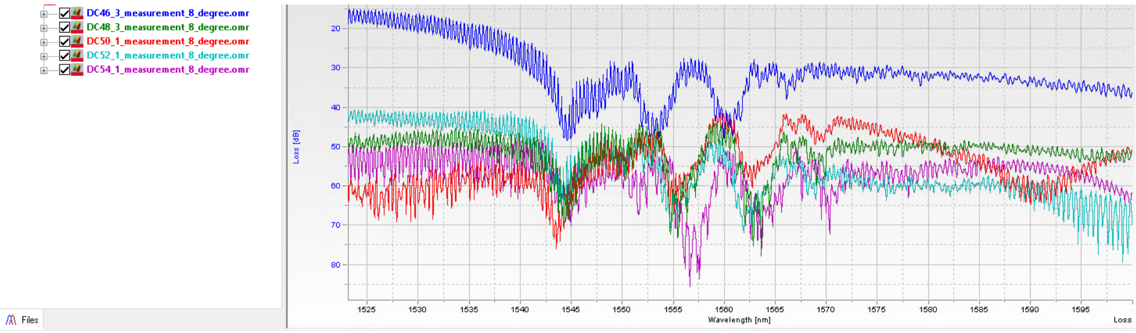

(a)

Figure 3.20: Phase-shifters output powers: second round of fabrication, sample 2A.

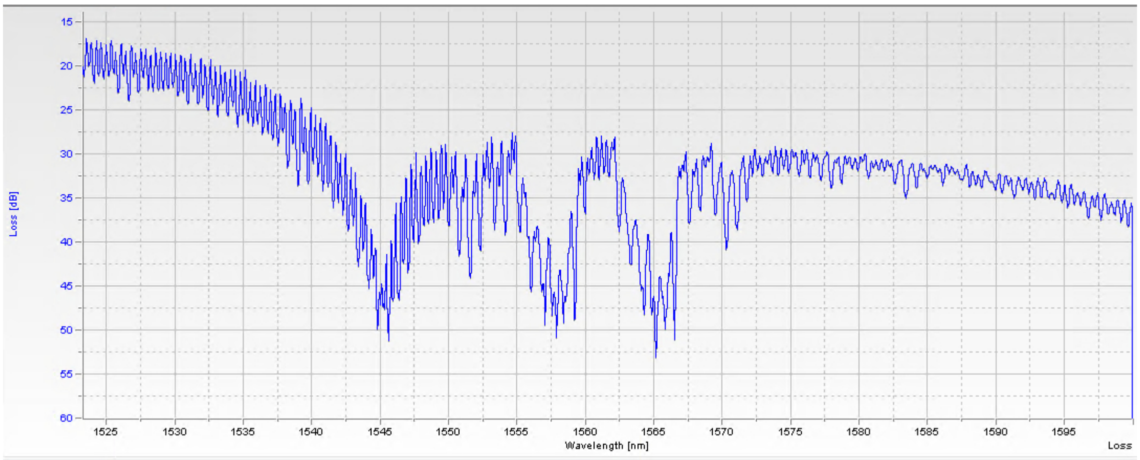

(a)

Figure 3.21: Phase-shifter with short heater output power: second round of fabrication, sample 2A.

Sample 2B On sample 2B, both active and passive measurements on part of the devices on the PIC have been performed with an angle of 8° respect to the normal. In Fig. 3.22 the output powers for the normalization waveguides in sample 2B are reported. It can be noted that from WG3 up to WG5 there is a larger loss compared to the WG1, WG2 and WG6. Moreover, WG5 output is not centered around 1550 nm.

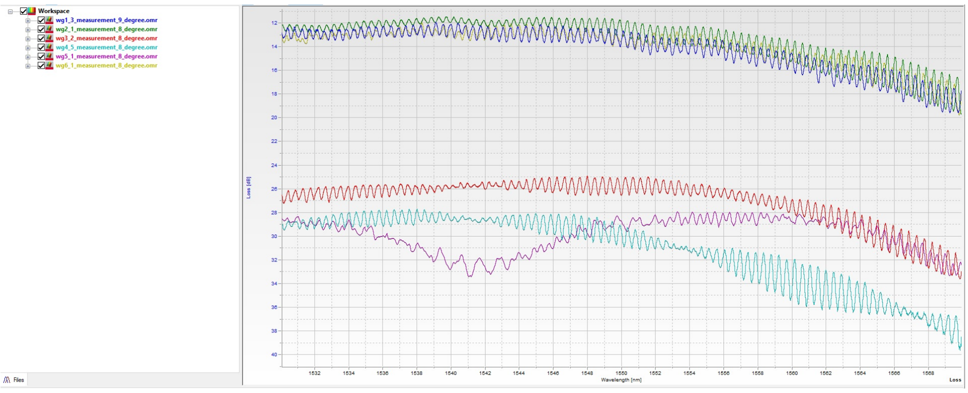

(a)

Figure 3.22: Normalization waveguides: second round of fabrication, sample 2B.

In Fig. 3.23 the measurements concerning the output powers of the short spirals are reported. It can be seen that, as in the previous sample, the outputs do not decrease uniformly with increasing length of the spiral. For example, SS5 has a larger output than SS3 and SS4; moreover, very large losses can be seen for SS4, SS6 and SS7. Similar results have been obtained for long spirals, as shown in Fig. 3.24.

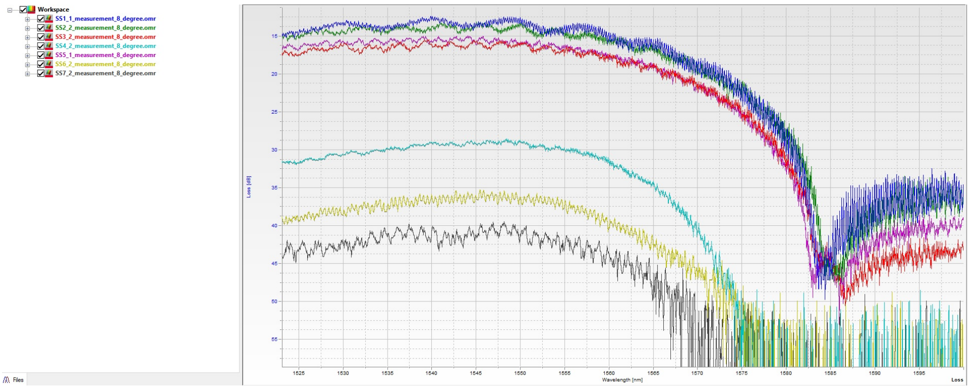

(a)

Figure 3.23: Short spirals output powers: second round of fabrication, sample 2B.

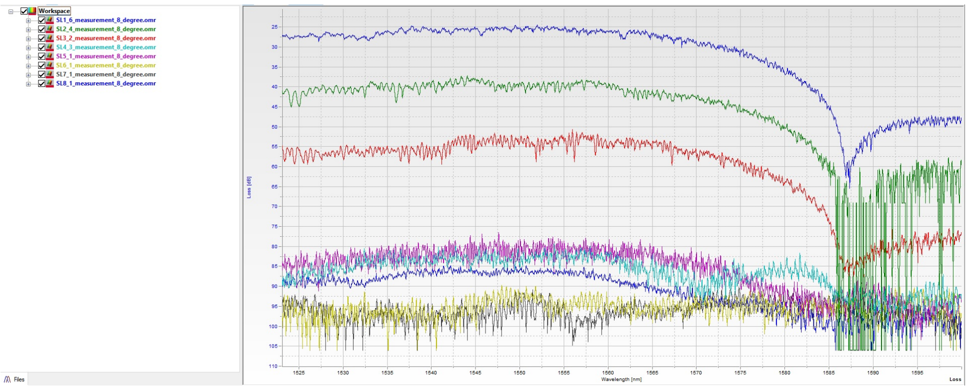

(a)

Figure 3.24: Long spirals output powers: second round of fabrication, sample 2B.

In Fig. 3.25 the output powers measured for the grating couplers are reported. The grating couplers exhibit the expected broadband response around 1550 nm. However, the measures are affected by pronounced ripples and deep notches; they can be attributed to parasitic interference and measurement limitations (alignment/polarization) when the transmitted power approaches the system noise floor. The measured responses do not show a monotonic trend with the duty cycle; this behavious is expected since the coupling efficiency depends in a non-linear way on the grating fill factor through both the coupling strength and the phase-matching condition.For this reason, a quantitative comparison should be performed by extracting the spectral envelope and reporting peak loss, central wavelength, and 3 dB bandwidth as a function of duty cycle.

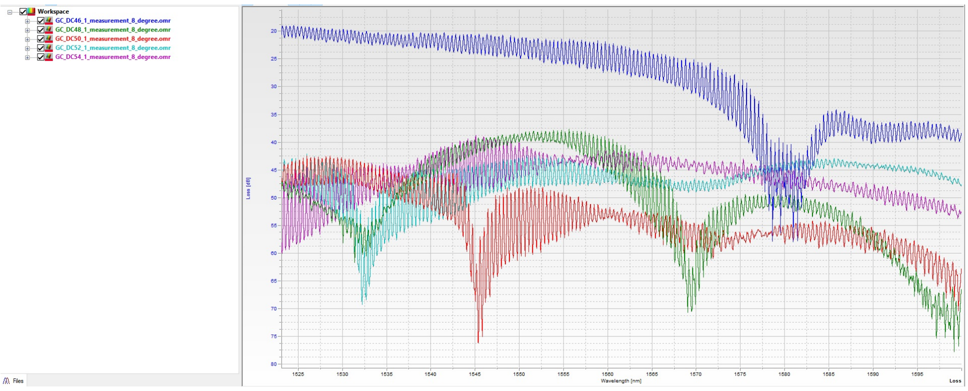

(a)

Figure 3.25: Grating couplers output powers: second round of fabrication, sample 2B.

In Figs. 3.26 and 3.27 the phase-shifter outputs spectra are reported for the different duty cycles. Compared to the previous sample, the response is more consistent with the expected two-notches behavior around 1550 nm: two pronounced minima are clearly visible in the designed spectral region; moreover, their positions and shapes vary systematically across the tested duty cycles. This indicates improved device uniformity and a closer match to the intended non-uniform Bragg-grating response. Outside the designed band, the traces exhibit strong oscillations, which can be attributed to low transmitted power and parasitic interference effects, and are therefore not considered in the performance assessment. The improved agreement suggests that fabrication-induced non-uniformities can strongly impact the spectral response of non-uniform Bragg gratings, leading to sample-to-sample variability.

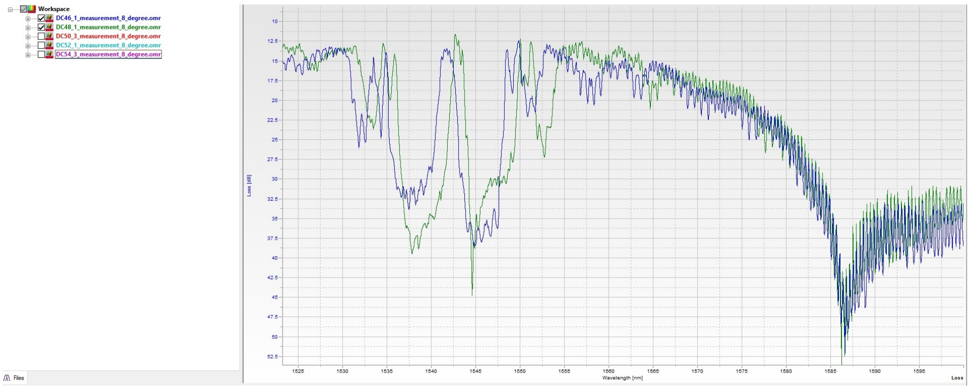

Workspace
☑ DC46_1_measurement_8_degree.omr
☑ DC48_1_measurement_8_degree.omr
☐ DC50_3_measurement_8_degree.omr
☐ DC52_1_measurement_8_degree.omr
☐ DC54_3_measurement_8_degree.omr

(a) Phase-shifters DC 46 to 48.

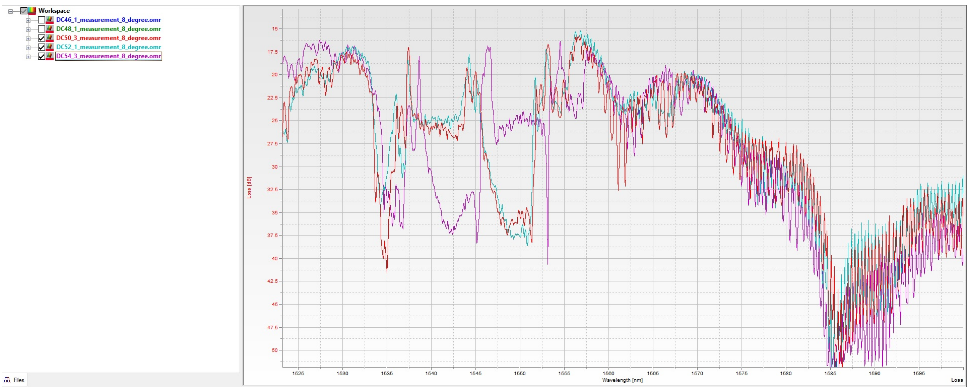

Workspace
☐ DC46_1_measurement_8_degree.omr
☐ DC48_1_measurement_8_degree.omr
☑ DC50_3_measurement_8_degree.omr
☑ DC52_1_measurement_8_degree.omr
☑ DC54_3_measurement_8_degree.omr

(b) Phase-shifters DC 50 to 54.

Figure 3.26: Phase-shifters output powers: second round of fabrication, sample 2B.

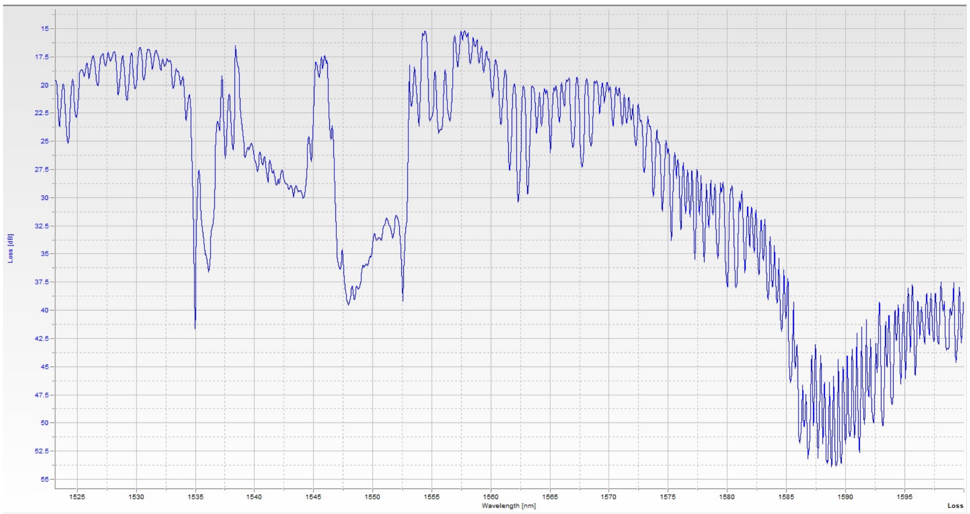

(a)

Figure 3.27: Phase-shifters with short heater output powers: second round of fabrication, sample 2B.

3.2.2 Active measurements

Active measurements have been performed by using DC probes as shown in the setup reported in Fig. 3.28.

(a)

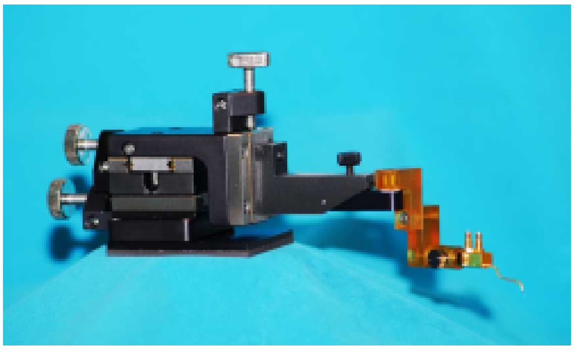

(b)

Figure 3.28: Adopted probes for active measurements.

The device named PS-SH of the copy on the top left quadrant has been tested. The heating elements on the sample are 52 nm TiN; 10 nm Ti layer was deposited as adhesion layer. The contact pads are 200 nm aluminum. The active measurements have been performed using American Probe & Technologies, Inc. probes made of Tungsten (72T Series Tungsten Probes, Fig. 3.28). Some pictures of the setup for active mearusements are reported in Fig. 3.29.

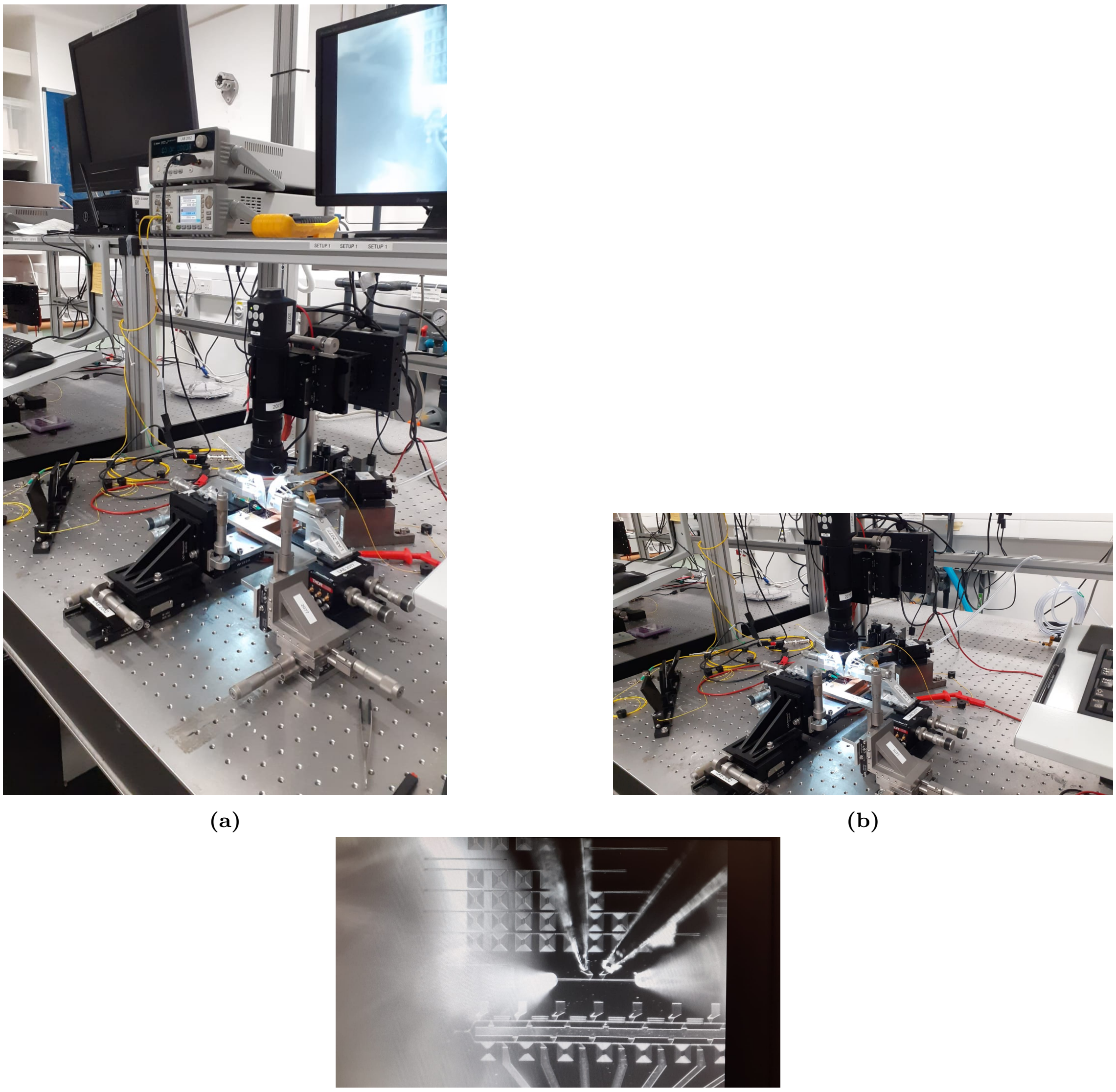

(a)

(b)

(c)

Figure 3.29: Setup view of the active measurements.

In Fig. 3.30 the output powers for different applied voltage on sample 2B on the short heater phase-shifter is reported. It can be appreciated the uniform expected shift of the wavelengths for increasing applied external voltage. In Fig. 3.31 the behaviour of each applied voltage is separately reported for clarity.

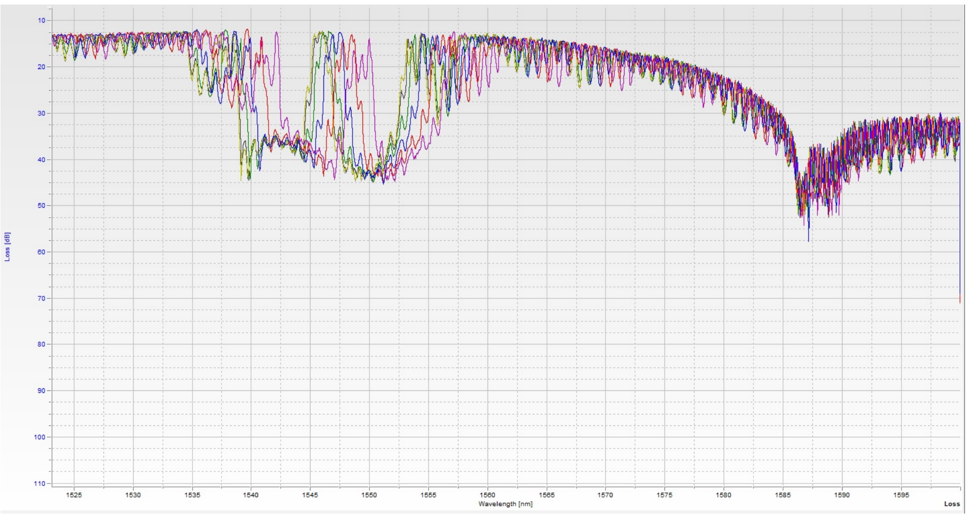

(a)

Figure 3.30: Output power for the phase-shifted WBGR as a function of different applied voltage on sample 2B, second run of fabrication.

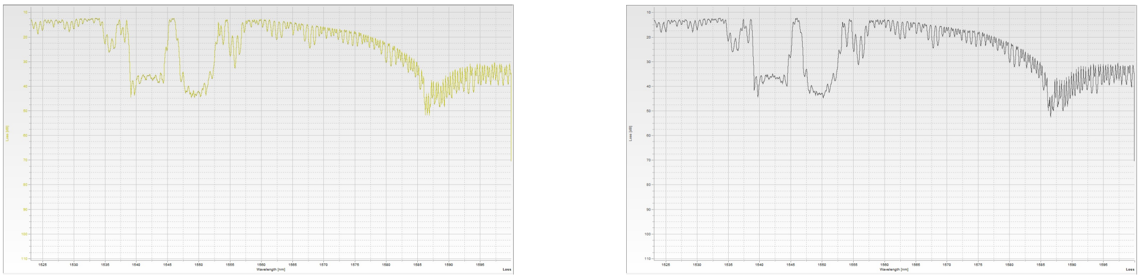

(a) Applied voltage V= 0 V.

(b) Applied voltage V= 1 V.

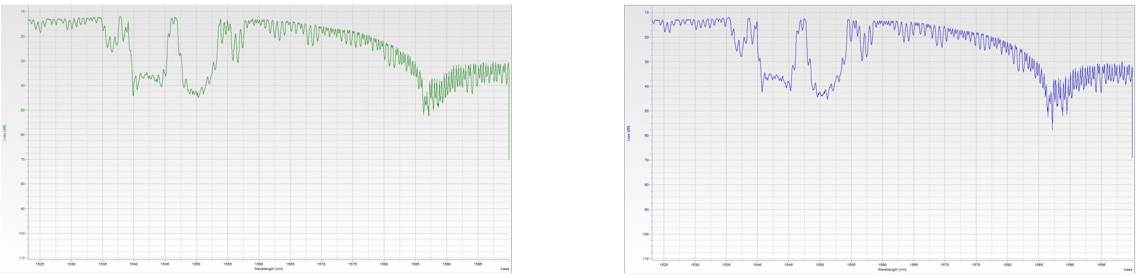

(c) Applied voltage V=2 V.

(d) Applied voltage V= 3 V.

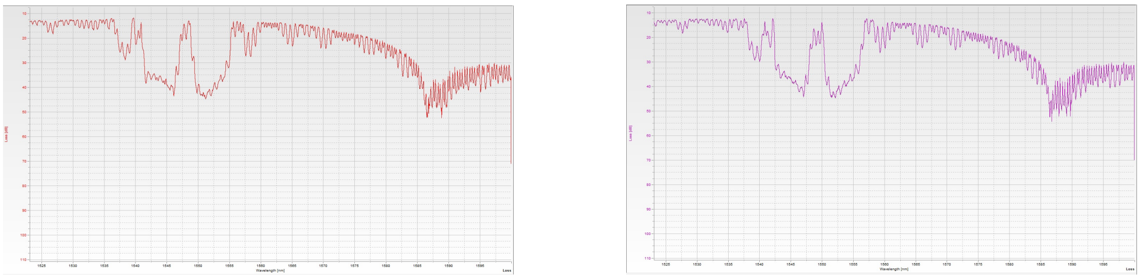

(e) Applied voltage V= 4 V.

(f) Applied voltage V= 5 V.

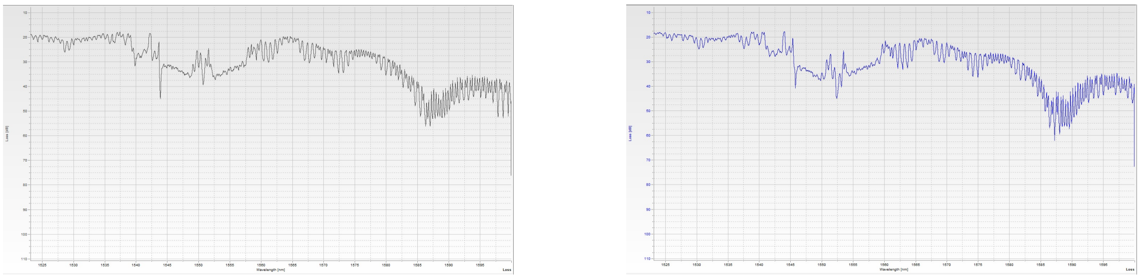

(g) Applied voltage V= 6 V.

(h) Applied voltage V= 7 V.

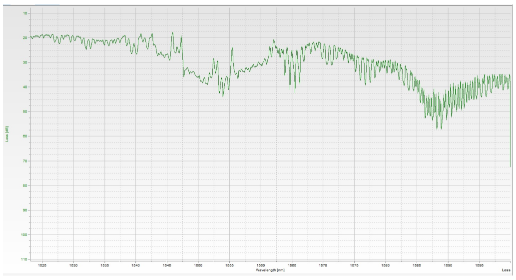

(i) Applied voltage V= 8 V.

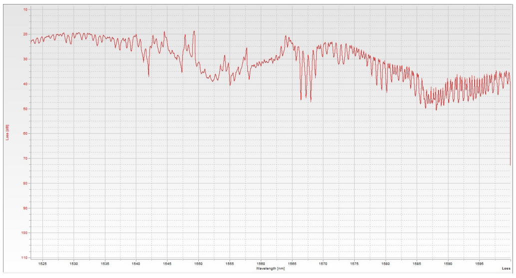

(j) Applied voltage V= 9 V.

Figure 3.31: Phase-shifter with short heater: behaviour of the outputs as a function of the applied voltage.

3.3 Summary on the experimental outcomes

The overall comments on the measurements taken on sample 1, 2 and 3 are here summarized:

1. the deposition of SiO_2 on sample 1 allowed to have the expected behaviours for the phase-shifted WBGR; it decreased the output powers for all the devices on the PIC;
2. the peaks of the output powers for the spirals do not decrease linearly;
3. spirals have unexpected high losses; a better design of their turns might improve the performances;
4. the WBGR show the expected behaviour, i.e. stopband + a reflection notch around the Bragg wavelength;
5. in the active measurements, the applied voltage shifts the notch of the phase-shifted WBGR, as expected from the design.

Chapter 4

Computational spectrometers

Among recently developed integrated spectrometers, an important role has been addressed by the so called *computational* or *reconstructive spectrometers* (RCs).

In this chapter, the basics of these spectrometers will be reviewed. In particular, in Section 4.1 the algorithms adopted to reconstruct the spectrum will be described, and the procedure will be analyzed step-by-step. In Sections 4.4 a different kind of computational spectrometer developed during the PhD research period will be described together with its metrics and performances. It is based on cascaded ring resonators in a similar fashion of the spectrometer described in Chapt. 2. In literature, several cascaded ring resonators computational integrated spectrometers have been suggested. In [188] a computational spectrometer using six optical resonators, each having two tuning states has been experimentally proved, with a reconstruction of 40 pm of resolution within 1525 nm and 1565 nm. Instead, in [189], a computational spectrometer with a footprint of $0.6 \times 0.8\ mm^2$ using eight micro-ring resonators with 20-μm radius.

Among the integrated spectrometers implementing as wavelength discriminating mechanism the filtering properties of ring resonators, several devices have been suggested with interesting metrics [190]–[192]. In this chapter, a very compact architecture is suggested, based on two ring resonators covered by segments of a phase change material (PCM) as in [192]. However, while in [192] the Vernier effect is harnessed in order to design a filter based spectrometer (hence susceptible to calibration procedures), here instead a computational spectrometer is suggested. Less and larger PCM segments are required in order to achieve this purpose. The advantage of using separated segments of PCM to be amorphized, allows for a digital control on the selected filters for the computational spectrometer. This is the reason why, in this context, it is possible to use only two resonators (rather than six [188] or eight [189]), still preserving a digital control on the filter transfer functions, with a Vernier-like configuration.

4.1 Types of computational spectrometers

In order to tackle the problem of the best algorithm to recover the spectrum of a computational spectrometer, it is useful to classify and summarize the main features of computational spectrometers. For this reason, it will be here given a brief classification and description of RCs, following the information reported and cited in [193].

RCs can be classified according to the way in which the spectral encoding is achieved in the device. In particular, it is possible to list three different kinds of spectral encoding, specifically **space-modulated**, **time modulated** and **light source** spectral encoding. These categories can be further distinguished as:

1. space-modulated spectral encoding:
    - speckle-based spectral encoding
    - filter array-based spectral encoding
    - detector array-based spectral enconding
2. time-modulated spectral encoding:
    - tunable filter-based spectral encoding

  - tunable photodetector-based spectral encoding

3. light source spectral encoding

4.2 Mathematical problem and solutions

Integrated spectrometers usually exhibit the limit of not having wavelength-specific filtering systems to recover the power of the input spectrum as a function of wavelength. In principle, the transmittance of a filter can ideally be modelled as Dirac delta functions at specific wavelengths. Moreover, in the ideal case, the transmittance functions of several filters are expected not to overlap with each other. As a consequence, by applying a filter working at a specific wavelength $\tilde{\lambda}$ to the input spectrum, the spectral energy of that specific wavelength $\tilde{\lambda}$ is outputted. By applying multiple filters, the output can be then interpreted as a discretization of the input spectrum.

However, when moving to non-ideal filters, the raw outputs need to be reconstructed in order to recover the input spectrum.

The problem of reconstructing the spectrum of a computational spectrometer can be mathematically formulated as a linear inverse problem. By nature, in most cases, the system of equations is ill-conditioned. In fact, experimental errors, noise and numerical errors influence the output and the reconstructing procedure. For this reason, it is fundamental to implement so-called *regularization* techniques and contrained optimization methods [194].

4.3 Description of the algorithm

The steps to be followed in order to computationally tackle the reconstruction of the spectrum for a computational spectrometer will be here listed and described:

1. the forward model describing the computational spectrometer should be defined:

$$p = A \cdot s \tag{4.1}$$

   being:

   - $p \in \mathbb{R}^M$: output powers for M filter configurations;
   - $s \in \mathbb{R}^N$: discretized spectrum (e.g., N- dimensional array representing the power given for N wavelengths);
   - $A \in \mathbb{R}^{M \times N}$: transmission matrix; each row represents the spectral response of a filter;

2. definition and regularization of the inverse problem. Being typically ill-posed, especially when $M < N$ or because of the ill-conditioned nature of A, the inverse problem:

$$s = A^{-1} \cdot p \tag{4.2}$$

   needs to be solved under the regularization condition:

$$\min_{s \geq 0} ||A \cdot s - p||^2 + \lambda \mathcal{R}(s) \tag{4.3}$$

   being $\mathcal{R}$(s) the **regularization** term and λ the **regularization parameter** or **hyperparameter**. $\mathcal{R}(s)$ is a function encoding prior knowledge or desirable properties in the solution s; it allows to penalize undesirable properties of the solution, e.g. roughness, large values or non-sparsity. The most common choices for the regularization term are:

   - Tikhonov or L2 regularization; it discourages large values:

$$\mathcal{R}(s) = ||s||^2 \text{or} ||\nabla s||^2 \tag{4.4}$$

     It penalizes fast-varying spectra or spectra with high-magnitude values. It is typically a good regularization approach for smooth, slowly-varying and broadband spectra, like blackbody radiation or absorption spectra.

- Lasso (**L**east **A**bsolute **S**hrinkage and **S**election **O**perator[195]) or L1 regularization; it promotes sparsity in the solution:

  $$\mathcal{R}(s) = ||s||_1 \tag{4.5}$$

  L1 regularization promotes sparsity by setting many coefficients equal to zero. In spectrometry, this is particularly useful when only a few wavelengths are expected to be nonzero. For this reason, this regularization procedure is ideal for sparse spectra, (e.g. laser line detection, Raman spectroscopy, systems with known sparse absorption/emission spectra etc);
- total variation regularization; it enforces smoothness in the solution while preserving edges:

  $$\mathcal{R}(s) = ||\nabla s||_1 \tag{4.6}$$

  It is usually adopted in the case of narrowband spectra or spectra consisting of flat regions with sharp peaks, like in the case of Raman or fluorescence signals and emission lines. It enforces sparsity in derivatives.

Instead, the regularization parameter λ is a scalar that determines the weight of the regularization term on the solution s. It controls the trade-off between:

- fitting the data, i.e. minimizing $||A \cdot s - p||^2$;
- enforcing that the solution s satisfies desirable properties via the regularization term $\mathcal{R}(s)$.

The value of λ determines which of these two procedures should be prioritized. Specifically, if λ is small, the data fitting is prioritized; at the limit, for $\lambda = 0$, the solution s fits the data only. This can lead to overfitting or noise amplification. On the contrary, if λ is large, the regularization is prioritized by enforcing, e.g., smoothness and sparsity; at the limit, the solution s may only minimize $\mathcal{R}(s)$ ignoring the data to be fitted. This can lead to deviations from measurements.

The features of A, i.e. the matrix containing the response of each filter, are fundamental to determine how the solution of the inverse problem should be performed. The main characteristics of A are:

1. non-negativity: $A_{ij} \geq 0 \forall i, j$. This feature derives from the fact that a filter transmits light, at the limit it does not allow light to pass, but it cannot generate light;
2. low coherence [196], [197]: each row of the spectral response matrix A should be ideally orthogonal to the others. Mutual coherence is measured as:

   $$\mu(A) = \max_{i \neq j} \frac{|a_i \cdot a_j}{||a_i||||a_j||} \tag{4.7}$$

   The result is in the range [0,1]; in particular, $\mu(A) = 0$ means orthogonal rows while $\mu(A) = 1$ corresponds to identical or fully correlated rows. The former case is ideal for implementing reconstructing algorithms. In practice, values of $\mu(A)$in $[0, 0.3]$ correspond to very low coherence and matrix A would be ideal for reconstruction. Values up to 0.5 are still acceptable in order to have reliable sparse data and regularized spectrum recovery;
3. full rank and well-conditioned: A should have the maximum number of non-linearly dependent rows or columns, and a small variation of its values should correspond to small variations of the solution of the linear system;
4. peak diversity: the central wavelengths of the filters should be well spread across the spectrum to avoid redundancy and improve the conditioning of the filters response matrix [198];
5. bandwidth (FWHM) limits: the FWHM of each peak in each filter should be not too low (narrow peaks) nor to high (wide peaks). This allows the system's ability to distinguish spectral features, to reduce mutual coherence, and to improve the quality of the reconstruction procedure [199];

6. cosine distance: it represents another way to compute the orthogonality between filters. The cosine distance is defined as:
$$d_{\cos} = 1 - \cos(\theta) \tag{4.8}$$
being $\cos\theta = \frac{a \cdot b}{\|\mathbf{a}\|\|\mathbf{b}\|}$, with a and b two vector states representing two filters.

7. smooth and band-limited filters responses: physical filters have smooth profiles (often Lorentzian or Gaussian like shapes); for this reason, abrupt jumps or extremely narrow spikes are not realistic;

8. spectral coverage: the whole manifold of filters should cover the full bandwidth of interest. There should be no large gaps in the wavelengths domain where no filters are sensitive.Controlled overlap between adjacent filters can improve conditioning and robustness; however, excessive overlap can make the response matrix A too redundant and reduce resolution

According to the properties that have been listed above it is possible to populate the filters response matrix. In particular, it is useful to follow different criteria: firstly, it is important to have rows that are orthogonal to each other. Practically, the dot products should be smaller than an orthogonality threshold (e.g. 0.1). Secondly, the L2 norm should not be too low (e.g. 0.001). In fact, this value is related to the energy content for each filter hence the lower the energy the poorer the energy information connected to that filter. Thirdly, a maximum number of rows can be imposed in order to reduce the computing time required for the reconstruction.

4.4 A computational spectrometer based on cascaded ring resonators

Computational spectrometers make use of post-processing algorithms applied to several optical outputs, each acquired at the output of a specific filter (said filters could be either spatially distributed or realized by means of a time-varying single filter) to reconstruct the optical spectrum at the input of the spectrometer. The transfer functions of the filters should realize ideally an orthogonal set in order to maximize the reconstruction capabilities, with a limited number of filters. In this section, we present the same spectrometer architecture shown in Chapter 2 and published in [192] which is adopted here for realizing a computational spectrometer. In detail, two cascaded ring resonators (see Fig. 4.1) realized with a Si_3N_4 wire waveguide, with a series of segments of phase-change material (Sb_2S_3) deposited on top of the $\mathrm{Si_3N_4}$ wire (see Fig. 4.2), separated by SiO_2. Each segment of PCM can be amorphized by means of the activation of the corresponding graphene microheater in each ring resonator. Graphene microheaters are not shown in Fig. 4.2 for clarity reasons, but the principle of the electrical programming of each segment is the same presented in [192]. The two resonators are displaced in a sufficiently distant way, such that the transfer function of the cascaded resonators (that we will refer to as "transmittance function") can be considered the product of the transfer function of each resonator (as in [192]). In the specific example, a limited number of transfer functions of the first and second resonators need to be selected in order to give rise to a set of mutually orthogonal transmittance functions. In this way, the objective will be to find the minimum set of of mutually orthogonal transmittance functions in order to be able to safely reconstruct the input spectrum.

Starting from the architecture described in Chapter 2 it is then possible to design a computational spectrometer. As a matter of fact, indipendent filters working at different wavelength ranges can be obtained by switching on/off PCM segments on the first and on the second ring. The crucial point of this alternative kind spectrometer is the search of configurations of amorphous and crystalline segments on both rings that would allow to span the bandwidth of interest and at the same time reducing the number of PCM segments on each ring.

Among the conditions described above, constraints on the orthogonality of the states and the on their norms (representing their energy contents) have been imposed in the search of the configurations to be implemented in order to have a superposition of reliable filters working at different wavelenghts of the bandwidth. Using the Dirac notation, each state is identified as a ket; hence the orthogonality condition can be written as:
$$\langle\psi_i| |\psi_j\rangle = 0 \forall i \neq j \tag{4.9}$$

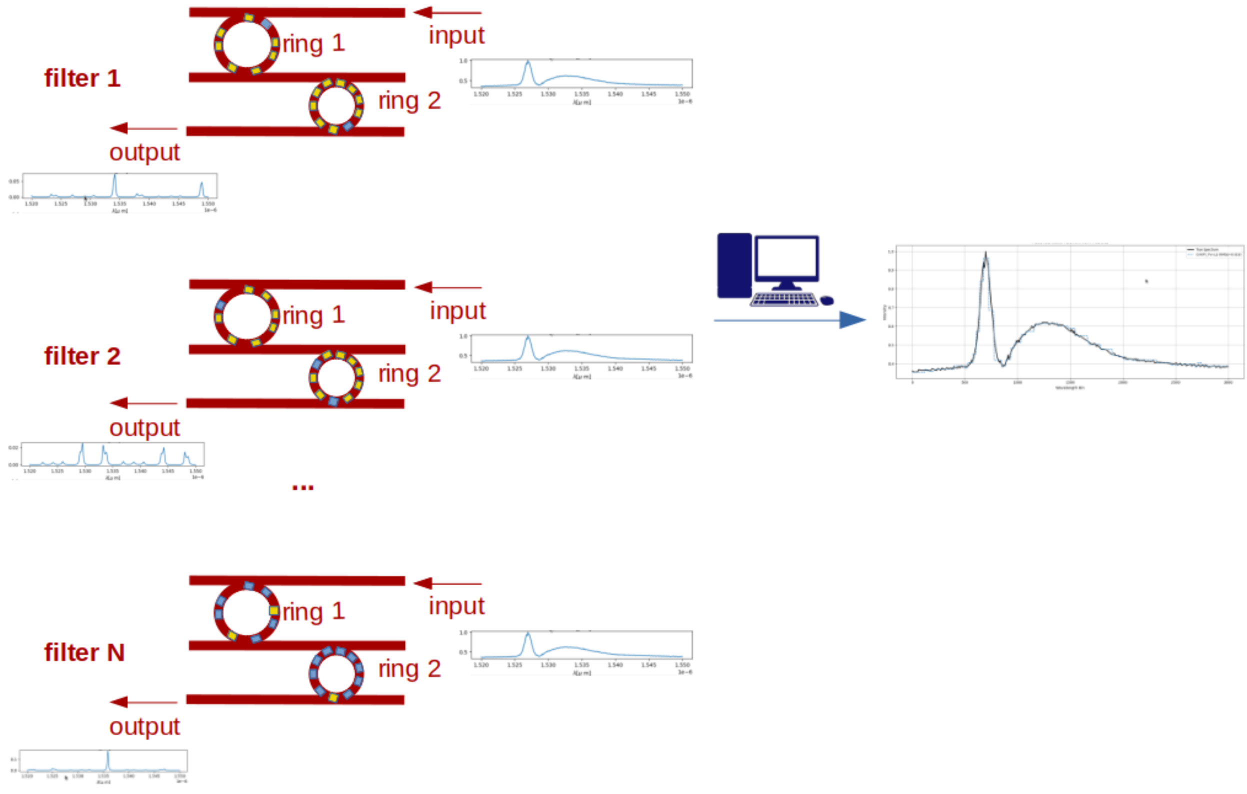

Figure 4.1: Reconstruction procedure and system architecture suggested in the paper.

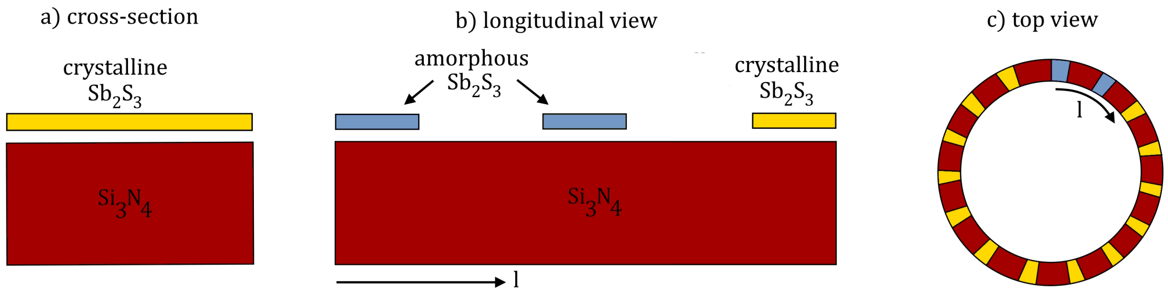

Figure 4.2: (a) Cross section of ring resonator. (b) Longitudinal view along the ring resonator. (c) Top-view of the ring resonator

The suggested architecture has been numerically tested as a computational integrated spectrometer. The ring resonators architecture is shown in Fig. 4.1; the PCM segments are randomly switched on and off in several configurations. The lengths and the materials adopted are the same reported in the architecture of the spectrometer suggested in [192]: m_1=480, m_2=640, resulting in lengths l_1=0.00044 m and l_2=0.00059 m. In order to populate the filters response matrix, it is useful to follow different criteria: firstly, it is important to have rows that are orthogonal to each other. Practically, the dot products should be smaller than an orthogonality threshold (e.g. 0.1). Secondly, the L2 norm should not be too low (e.g. 0.001); in fact, this value is related to the energy content for each filter hence the lower the energy the poorer the energy information connected to that filter. Thirdly, a maximum number of rows can be imposed in order to reduce the computing time required for the reconstruction. For these reasons, the number of segments for each ring resonator has been set to 40. Each segment has a fixed length of 9 μm. The filters response matrix has been populated accepting configurations with: dot product with all the previous configurations equal to 0.3 and energy threshold for each configuration equal to 10^{-3}. These thresholds have been empirically chosen based on matrix conditioning and mutual coherence minimization principles [200], [201]. Moreover, the peak diversity is achieved by implementing a minimum peak separation with the the peaks of the previous filters equal to 5 nm. The minimum and maximum FWHM have been set to 5 nm and 50 nm, respectively; the minimum cosine distance has been set to 0.1.

Simulations have been performed with a minimum length for each PCM segment equal to 9000 nm, both on ring 1 and ring 2. The increased lenght of the PCM segment compared to the one adopted in the previous filter-based version allows to have a lower number of segments for each ring and a higher randomness in the search of the orthogonal configurations to be used in the computational approach. The algorithm implemented in the search for filters is the following:

1. two counters are created to describe the number of PCM segments that undergo phase transition from crystalline to amorphous on ring 1 and ring 2;
2. one segment on each ring is switched on:
    - the l^2-norm of the state representing this first configuration ψ_1 is computed; if the condition:
    $$\|\psi_1\|_2 < 10^{-4} \tag{4.10}$$
    is satisfied, such state is appended to the vector of acceptable solutions;
    - if the previous condition is not satisfied, an additional segment on one ring is switched on; the norm is again computed and if condition 4.10 is satisfied, this configuration is appended as a row of the spectral response matrix A, otherwise an additional segment is switched on.
3. once the first row of the filter of the spectral response matrix is populated, the search for the additional filters to be appended to A is performed both by searching states satisfying the condition reported in Eq. 4.10 and by checking the orthogonality of the candidate state $\langle\psi_i|$with all the filters that have been already appended to A. Numerically, if n_f represents the number of the filters already present in A, this second condition can be written as:
$$\langle\psi_i|\psi_j\rangle < 0.5 \quad \forall j \leq n_f \tag{4.11}$$

The number of PCM segments on each ring is 40, and the length of each segment is 9000 nm.

An input spectrum with both narrow and wide features has been tested, in order to see the performances of the selected filters in capturing a random input spectrum. Indeed, as previously stated, reconstruction algorithms perform differently according to the input spectrum features. Testing a mixed features input allows for a higher confidence on the quality of the selected filters.

Results of the reconstruction procedures are reported in Figs.4.3 and 4.4. It can be seen by Fig.4.3 the orthogonality features of the chosen filters, according to the threshold imposed in the algorithm. The reconstruction of the spectrum is achieved using several solvers; in particular, the algorithm selects the one (or combination of solvers) with the lower root mean square error. Solvers from the PyPI library and from the project TRIPs-Py [202] have been explored. For the specific input spectrum, the better performing algorithms are reported in Fig. 4.4, where both CVXPY and L2 guarantee a very high quality reconstruction.

4.5 Conclusions and perspectives

In this chapter, a computational integrated spectrometer based on two cascaded ring resonators has been described. The digital control of the transfer function of each resonator, enabled by the segmented phase-change-material layer, and the presented reconstruction algorithm allow for the possibility of using only two ring resonators in a Vernier-like configuration to realize a computational spectrometer, working in a bandwidth of 30 nm, with a resolution of 0.1 nm on a footprint of 0.3 × 0.3 mm^2. The digital switch among the configurations (hence filters) is achieved by thermally changing the phase of stibnite segments present in both rings. The reconstruction algorithm is able to computationally reconstruct the input spectrum with a low root mean square error (RMSE=0.009 in the reported example).

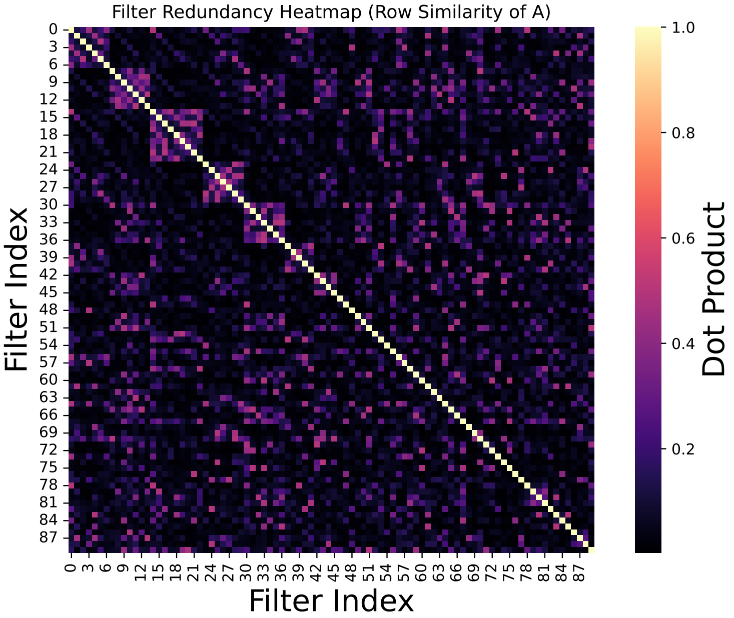

Figure 4.3: Heatmap reporting the orthogonality features among the selected filters. Non-full diagonal response matrix is found because of the chosen values of dot product: a lower value would have implied a scarser reconstruction ability of the algorithms.

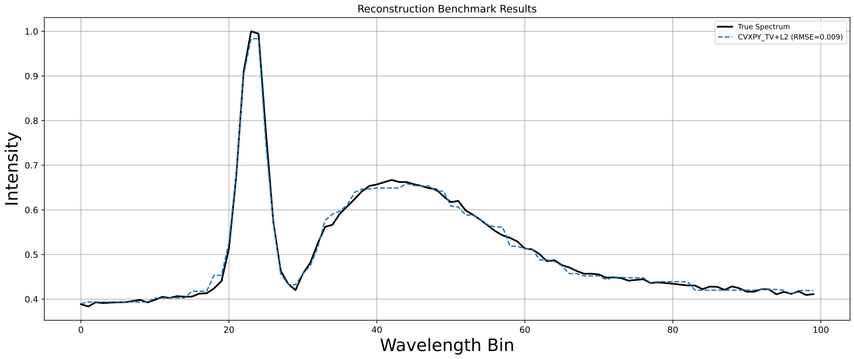

Figure 4.4: Reconstruction results for the suggested integrated spectrometer. A spectrum with mixed features (wide and narrow peaks) have been used as an input in order to test the ability of the reconstruction algorithm to retrieve the input spectrum.

Chapter 5

Quantum optics and single-photon spectrometers

In the description provided so far, the development of integrated spectrometers has been focused to the case of the detection of light as classically described. However, in applications where the incident light is very faint, it is important at the limit to be able to detect single photons. In principle, the same architectures described so far can operate in the photon-starved regime by replacing power readout with photon-counting detection. In this context, the system design principles and reconstruction strategies discussed earlier remain applicable, while the measurement model should be replaced from continuous power measurements to counting statistics. When scarse photon sources are considered as input to the spectrometer, the description is required to move towards very interesting research related to the quantum nature of light. It is then worth introducing the formalism of single photon quantum optics, to deepen the knowledge about the features of this special limit of light, and to link these aspects to the technological challenges related to the detection and description of such states of light. This chapter introduces the minimum formalism required to describe single-photon detection and outlines when a full quantum-optics treatment becomes necessary. A resume of the quantum optics formalism will be presented based on the seminal work by Grynberg, Aspect and Fabre [203] and lessons available on-line by prof. Alain Aspect. The latter have been attended during the PhD course.

5.1 Quantization of Maxwell's equations

5.1.1 Normal modes and classical field energy.

An electromagnetic field is composed of an electric field **E** and a magnetic field **B** that satisfy Maxwell's equations. Such a field can exist even in the absence of charges and currents. In this case we refer to it as *free radiation.* Although a physical source must exist to create the field, when strudying regions far from the source (e.g. sunlight reaching the Earth or a radio wave received kilometers away from an antenna) Maxwell's equations without sources can be used. In the following, the case of free radiation will be analyzed. The case of interest is radiation in a volume without sources. In vacuum, Maxwell's equations (in SI units) read:

$$\nabla \cdot \mathbf{E} = 0, \qquad \nabla \cdot \mathbf{B} = 0, \tag{5.1}$$

$$\nabla \times \mathbf{E} = -\frac{\partial \mathbf{B}}{\partial t}, \qquad \nabla \times \mathbf{B} = \mu_0 \epsilon_0 \frac{\partial \mathbf{E}}{\partial t} = \frac{1}{c^2}\frac{\partial \mathbf{E}}{\partial t}, \tag{5.2}$$

with $c = 1/\sqrt{\mu_0 \epsilon_0}$.

The most elementary solution of Maxwell's equations is called a *mode*, i.e. a field that oscillates at a well defined frequency.

$$\mathbf{E}(\mathbf{r},t) = \hat{\varepsilon}_\ell\, \mathcal{E}_\ell(t)\, e^{i\mathbf{k}_\ell \cdot \mathbf{r}} + \text{c.c.}, \qquad \boldsymbol{\epsilon}_\ell \cdot \mathbf{k}_\ell = 0, \qquad \mathcal{E}_\ell(t) = \mathcal{E}_\ell(0)\, e^{-i\omega_\ell t}, \tag{5.3}$$

with dispersion $\omega_\ell = c|\mathbf{k}_\ell|$ and $\mathbf{B} = \frac{1}{\omega_\ell}\mathbf{k}_\ell \times \mathbf{E}$. c.c. in Eqs. 5.3 means complex conjugate. Since it oscillates, it will be quantized as a harmonic oscillator.

The canonical quantization procedure can be applied to this case; this allows to introduce important observables of quantum optics. There are many different kinds of modes; here, the simplest possible mode will be assumed, i.e. a travelling plane wave, describing a freely propagating field. Equations 5.3 are solutions of Maxwell's equations provided that some conditions are fulfilled. Indeed, the field E is real, and in order for it to satisfy Maxwell's equations, the unique vector, $\boldsymbol{\epsilon}_\ell$, has to be perpendicular to the wave vector, k_l (in order to satisfy $\nabla \cdot \mathbf{E} = 0$):

$$\varepsilon_\ell \perp \boldsymbol{k}_\ell. \tag{5.4}$$

$\hat{\varepsilon}_\ell$ defines a polarization of the field, i.e. a direction of the electric field. Another condition for Eq. 5.3 to be solution of Maxwell's equations is that the complex number $\mathcal{E}_\ell$, characterizing the amplitude of the field, oscillates at an angular frequency, ω_l:

$$\mathcal{E}_\ell(t) = \mathcal{E}_\ell(0) exp^{-i\omega_\ell t}. \tag{5.5}$$

Moreover, the angular frequency, ω_ℓ, must be equal to the speed of light, c, times the modulus of the wave vector k_ℓ:

$$\omega_\ell = c|k_\ell|. \tag{5.6}$$

The equation for the mode can eventually be written as:

$$\mathbf{E}(\mathbf{r},t) = \hat{\varepsilon}_\ell\,\mathcal{E}_\ell(0)\,e^{i\mathbf{k}_\ell\cdot\mathbf{r}-\omega t} + \text{c.c.}. \tag{5.7}$$

The ensemble of the vector k_ℓ that determines the direction of propagation and the frequency of the field with a unit vector $\hat{\varepsilon}_\ell$ perpendicular to k_ℓ, characterizes a mode, referred to as a polarized monochromatic travelling wave. There are other kinds of modes, e.g. standing waves. In general, a mode is an elementary oscillating solution of Maxwell's equation. The characteristics of the mode k_ℓ and ϵ_l only determines the structure of the field; it is also important to know the complex amplitude $\mathcal{E}_\ell$ which characterizes the state of the field in the mode ℓ. The complex number $\mathcal{E}_\ell$ is fully determined by two real variables; for instance, its real and imaginary parts or its modulus and phase. These variables are dynamic variables describing the state of the classical field in the mode ℓ. To fully understand, the case of a pendulum will be used. The mode is characterized by the oscillation frequency and the plane of oscillation; however, the state of the pendulum can be determined by knowing the amplitude and the phase of the oscillation; the latter are given by the modulus and the phase of the complex amplitude of the position. Equivalently, the real and imaginary parts of the complex amplitude are needed. They are the dynamic variables describing the state of the pendulum. In order to identify two dynamic variables of the electromagnetic field, that are canonically conjugate of each other, more details deriving from Maxwell's equations are needed. For simplicity, the formula describing the effect of the differential operator nabla on the mode:

$$\nabla\cdot\mathbf{E}(\mathbf{r},t) = i\,\mathbf{k}_\ell\cdot\hat{\varepsilon}_\ell\;\mathcal{E}_\ell(t)\;\exp\big\{i\,\mathbf{k}_\ell\cdot\mathbf{r}\big\} + \text{c.c.}$$

being:

$$\nabla = \frac{\partial}{\partial x}\,\mathbf{e}_x + \frac{\partial}{\partial y}\,\mathbf{e}_y + \frac{\partial}{\partial z}\,\mathbf{e}_z.$$

Hence, the divergence of E takes a simple algebraic form. $\hat{\varepsilon}_\ell \times \mathcal{E}_\ell$ is a complex vector E_l. The first Maxwell equation then entails that ε_ℓ is perpendicular to k_l. Similarly:

$$\nabla \times \mathbf{E}(\mathbf{r},t) = i\,\mathbf{k}_\ell\times\hat{\varepsilon}_\ell\;\mathcal{E}_\ell(t)\;\exp\big\{i\,\mathbf{k}_\ell\cdot\mathbf{r}\big\} + \text{c.c.}. \tag{5.8}$$

Using the second and the third Maxwell equations, it can be derived that $\hat{E}, \hat{B}$ and $\hat{k}$ are three mutually orthogonal vectors forming a right-handed set. Finally, using the fourth Maxwell equation we find that $\hat{B}$ has a form with the same complex exponential as $\hat{E}$:

$$\mathbf{B}(\mathbf{r},t) = \frac{i}{\omega_\ell^2}\mathbf{k}_\ell \times \hat{\varepsilon}_\ell \frac{\mathcal{E}_\ell(t)}{dt} e^{i\mathbf{k}_\ell\cdot\mathbf{r}} + \text{c.c.}. \tag{5.9}$$

By performing the time derivative of this expression and using the second Maxwell's equation, a second order differential equation for the complex amplitude E_l is retrieved:

$$\frac{d^2\mathcal{E}_\ell(t)}{dt^2} = -\omega_\ell^2\mathcal{E}_\ell(t). \tag{5.10}$$

This is equivalent to two first order equations:

$$\frac{d\mathcal{E}_\ell(t)}{dt} = \pm i\omega_\ell \mathcal{E}_\ell(t) \tag{5.11}$$

with oscillatory solutions:

$$\mathcal{E}_l(t) = \mathcal{E}_\ell(0)\exp(\pm i\omega_\ell t). \tag{5.12}$$

One solution is associated to the wave traveling along k, while the other is traveling against k. In order to have a single mode, one of the solutions should be kept. If we choose the one traveling along k_ℓ, we must take the exponential of $-i\omega_l t$:

$$\frac{d\mathcal{E}_\ell(t)}{dt} = -i\omega_\ell \mathcal{E}_\ell(t). \tag{5.13}$$

An explicit time-depending form for B can also be derived; it shows not only that k, E, and B form a direct tri-orthogonal set, but also that B is in phase with E. More precisely, the complex amplitude B_ℓ is equal to the complex amplitude E_ℓ divided by c:

$$\mathbf{B}(\mathbf{r},t) = \frac{\mathbf{k}_\ell \times \hat{\varepsilon}_\ell}{\omega_e ll}\mathcal{E}_\ell(t)\, e^{i\mathbf{k}_\ell\cdot\mathbf{r}} + \text{c.c.}. \tag{5.14}$$

It can be concluded that, for a travelling electromagnetic wave propagating along k_ℓ, the dynamics is fully determined by:

$$\frac{d\mathcal{E}_\ell}{dt} = -i\omega_l E_l. \tag{5.15}$$

The complex amplitude totally describes the state of the field since it allows to express E as well as B. Its dynamics is given by a first order differential equation. As a complex number, $\mathcal{E}_\ell$ is determined by two real variables (its modulus and its phase or its real and imaginary parts).

It will be now shown that the real and imaginary parts of $\mathcal{E}_\ell$ are canonically conjugated variables within a multipliying factor. Firstly, a so-called *normal variable* α_ℓ should be introduced; it is defined by writing the complex amplitude $\mathcal{E}_\ell$ as:

$$\mathcal{E}_\ell(t) = i\mathcal{E}_\ell^{(1)}\alpha_\ell(t). \tag{5.16}$$

The constant $\mathcal{E}_\ell^{(1)}$ will be the later determined and a clear meaning will be provided. It has the dimension of an electric field so that α_ℓ is dimensionless. In this case, the i factor is arbitrary, but it is a choice made by most authors in quantum optics. The evolution of α_ℓ is the same as the one of the complex amplitude $\mathcal{E}_\ell$:

$$\frac{d\alpha_\ell(t)}{dt} = -i\omega_\ell \alpha_\ell(t). \tag{5.17}$$

This equation fully determines the dynamics of the electromagnetic field in the mode ℓ.

It is worth introducing the real and imaginary parts of α_ℓ within a factor that will make future formulae simpler:

$$\alpha_\ell(t) = \frac{1}{\sqrt{2\hbar}}(Q_\ell + iP_\ell). \tag{5.18}$$

From this definition it can be derived that:

$$Q_\ell = \sqrt{\frac{\hbar}{2}}\,\big(\alpha_\ell(t) + \alpha_\ell^*(t)\big),$$

$$P_\ell = -\,i\sqrt{\frac{\hbar}{2}}\,\big(\alpha_\ell(t) - \alpha_\ell^*(t)\big).$$

Let us now write the energy of the electromagnetic field in the mode, knowing the structure of the mode, and the amplitude E_l. It involves two terms, E squared and cB squared:

$$H_\ell = \frac{\epsilon_0}{2}\int_{V_\ell} d^3r(E^2 + c^2B^2) \tag{5.19}$$

but for a running wave, the expression of B can be used to find that the second term is equal to the first term, hence:

$$H_\ell = \frac{\epsilon_0}{2}\int_{V_\ell}(E^2 + c^2B^2) = \epsilon_0\int_{V_\ell} d^3rE^2. \tag{5.20}$$

Then, a standard calculation allows us to express the integral of E squared as the volume of integration multiplied by two times the square of the modulus of the complex amplitude:

$$H_\ell = 2\epsilon_0 \int_{V_\ell} d^3r |\mathcal{E}_\ell(t)|^2. \tag{5.21}$$

The factor 2 derives from the previous definition of complex amplitude. In fact there is no difference between volume of integration and quantization volume that will be soon defined.

A choice is made on the constant $\mathcal{E}_\ell^{(1)}$: it is the amplitude of a field that has an energy $\hbar\omega_\ell$, in the volume of quantization V_ℓ. Introducing $\hbar\omega_\ell$ in a classical calculation is propaedeutic to quantization and it makes formula simpler. Let $\hbar\omega_\ell$ be the characteristic value of energy in the problem. This corresponds to the energy of a photon (equivalently $h\nu$). The constant, $\mathcal{E}_\ell^{(1)}$, is called the *one-photon amplitude* of the mode ℓ. As previously found, it is proportional to the square root of the inverse of the quantization volume:

$$\mathcal{E}_\ell^{(1)} = \sqrt{\frac{\hbar\omega_\ell}{2\epsilon_0 V_\ell}}. \tag{5.22}$$

Therefore, in this notation, a remarkable expression for the energy can be retrieved: the energy can be written as the energy of a harmonic oscillator:

$$H_\ell = \hbar\omega_\ell |\alpha(t)|^2. \tag{5.23}$$

The canonical quantization of the field in the mode ℓ can then be performed. However, before proceeding, it is fundamental to make some additional comments on the volume of quantization. It is a volume where the radiation is considered to be in. In the case of a cavity, it is a real volume: the volume of the cavity delimitated, e.g. by mirrors. The mirrors impose boundary conditions which in turn impose conditions on the k vector. For this reason, the volume is written with an explicit index ℓ to stress its dependence on the mode.

This raises the question on how a travelling wave of infinite extent should be handled. In such a case, a fictitious volume larger than the volume of interest is defined. For example: let the volume of quantization be a cubic box of size L; hence, the quantization volume is L^3. Since the free wave extends to infinity, the field should be smoothly prolongated beyond the boundaries of the cube. To achieve this, an easy solution is to periodically repeat the wave, being periodic in all directions of space. This condition is known as *periodic boundary conditions.* L becomes an integer number of spatial period of the wave along each axis:

$$k_x \times L = n_x \times 2\pi, k_y \times L = n_y \times 2\pi, k_z \times L = n_z \times 2\pi \tag{5.24}$$

being n_x, n_y and n_z integer numbers; similarly for the other components of k_l. For instance, the field at $x = 0, y = 0$ and $z = L$ is equal to the field at $x = 0, y = 0$ and $z = 0$, similarly for other directions. The integer numbers n_x and n_y and n_z can be negative in order to span all the possible directions of propagation. The extremity of vector k in the k-space cannot lie anywhere; in fact, it has to be on a three dimensional cubic grid with an elementary period of $\frac{2\pi}{L}$ along each axis. Periodic boundary conditions are therefore suitable for the quantization of free waves, although there are other situations where other choices would be more appropriate.

With these considerations, quantization the electromagnetic field can be carried out. From Eq. 5.18 the state of the field of the single mode ℓ is characterized by two dynamic variables, Q_ℓ and P_ℓ and the energy can be written as a function of these two particular variables. In the following, it will be shown that they are canonically conjugate variables; accordingly, quantization can be performed.

It is immediate to check that the Hamilton equations for Q_ℓ and P_ℓ yield an evolution equation for α_ℓ. Indeed, by combining Hamilton equations:

$$\frac{dQ_\ell}{dt} = \frac{\partial H}{\partial P_\ell} = \omega_\ell P_\ell,$$

$$\frac{dP_\ell}{dt} = -\frac{\partial H}{\partial Q_\ell} = -\omega_\ell Q_\ell.$$

the following equations can be derived:

$$\frac{d}{dt}(Q_\ell + i\,P_\ell) = -\,i\,\omega_\ell(Q_\ell + i\,P_\ell)$$

$$\implies \qquad \frac{d\alpha_\ell(t)}{dt} = -\,i\,\omega_\ell\,\alpha_\ell(t).$$

In particular, the last equation is the one obtained from Maxwell's equations applied to the field in the mode ℓ. Therefore, it can be concluded that Q_ℓ and P_ℓ are canonically conjugate variables. The canonical quantization procedure can then be applied by introducing the operators $\hat{Q}$ and $\hat{P}$ with commutator $i\hbar$:

$$\left[\,\hat{Q}_\ell,\ \hat{P}_\ell\,\right] = i\,\hbar.$$

Eventually the Hamiltonian as:

$$\hat{H}_\ell = \frac{\omega_\ell}{2}\,(\hat{Q}_\ell^2 + \hat{P}_\ell^2)$$

i.e. the hamiltonian for a quantum harmonic oscillator.

In order to use Dirac formalism $\hat{a}$ and $\hat{a}^\dagger$ are introduced:

$$\alpha_\ell(t) \to \hat{a}_\ell = \frac{1}{\sqrt{2\hbar}}\big(\hat{Q}_\ell + i\,\hat{P}_\ell\big),$$

$$\alpha_\ell^*(t) \to \hat{a}_\ell^\dagger = \frac{1}{\sqrt{2\hbar}}\big(\hat{Q}_\ell - i\,\hat{P}_\ell\big).$$

Their commutator is equal to 1:

$$\left[\,\hat{a}_\ell,\ \hat{a}_\ell^\dagger\,\right] = 1$$

and the remarkable expression for the hamiltonian is derived:

$$\hat{H}_\ell = \hbar\,\omega_\ell\left(\hat{a}_\ell^\dagger\hat{a}_\ell + \frac{1}{2}\right).$$

5.1.2 Observables in Quantum Optics

In quantum formalism, two different types of objects are typically encountered: states, represented by vectors of a Hilbert space, and observables, which are represented by hermitian operators. In the previous section, the observables $\hat{Q}_\ell$ and $\hat{P}_\ell$, whose commutator equals $i\hbar$, and the operators $\hat{a}$ and $\hat{a}^\dagger$ which are hermitian conjugates of each other have been introduced. $\hat{a}$ and $\hat{a}^\dagger$ are non-hermitian hence they do not correspond to physical observables. However, they play a major role. Their commutator is equal to 1. By inverting the expressions of $\hat{a}$ and $\hat{a}^\dagger$, $\hat{Q}_\ell$ and $\hat{P}_\ell$ as a function of $\hat{a}$ and $\hat{a}^\dagger$ can be recovered:

For the notation, the so-called *normal ordering* is priviledged for calculations; it corresponds to having the operator $\hat{a}$ on the right and the operator $\hat{a}^\dagger$ on the left. The field observables are also expressed as a function of $\hat{a}$ and $\hat{a}^\dagger$. As in the Schroedinger approach to quantum mechanics where the operators do not evolve, the field operators do not depend on time; only the states evolve with time. The state of the field is described by a state of vector $\psi(t)$; once known, the average value of the field can be computed:

$$\big\langle\hat{\mathbf{E}}(\mathbf{r})\big\rangle(t) = \big\langle\psi(t)\,\big|\,\hat{\mathbf{E}}(\mathbf{r})\,\big|\,\psi(t)\big\rangle.$$

This average may evolve with time. Moreover, the fluctuations of the field can be computed by calculating the average of its square, and comparing it to the square of the average. The fluctuations may also depend on time:

$$(\Delta E)^2 = \big\langle\psi(t)\big|\hat{\mathbf{E}}^2(\mathbf{r})\big|\psi(t)\big\rangle - \left[\,\langle\hat{\mathbf{E}}(\mathbf{r})\rangle(t)\,\right]^2.$$

A note should be done on the possibility to measure the field observables. In the domain of radio waves and up to frequencies of hundreds of Gigahertz, the electric or magnetic field can be directly detected using antennas and by processing signals oscillating at these frequencies. However, in the domain of visible light the frequency is $\sim 5 \times 10^{14}$ Hz, so high that no detector exists able to measure directly the electric or the magnetic field. Even the fastest detectors average a signal over a response time much longer than the period of the field and return a null result. Measurements can still be performed; for example, the energy can be measured with a bolometer, that represents an operator that absorbs radiation and the resulting increase of temperature can be measured. In this case the corresponding observable is the Hamiltonian. A photo-detector based on the photoelectric effect can also be used. In this case, a signal proportional to the probability of detection of a photon can be measured; therefore the number of photons can be measured:

$$\hat{N}_\ell = \hat{a}_\ell^\dagger \hat{a}_\ell. \tag{5.25}$$

It should not be confused with a Hamiltonian when there is more than one mode. Photo-detectors allow also to measure the observables $\hat{Q}_\ell$ and $\hat{P}_\ell$ using the so-called homodyne detection technique even for visible light. In fact, this is a good substitute to the direct observation of the field, since one can express a field operator as a function of $\hat{P}_\ell$ and $\hat{Q}_\ell$.

5.1.3 States in Quantum Optics and the concept of photon

States of quantized radiation are usually referred to as *number states of the quantized field.* The concept of photon naturally emerges in this formalism; moreover, there is a particular number state worth to be investigated: vacuum. As usual in Quantum Mechanics, starting from the Hamiltonian of the system it is possible to recover its eigenvalues (corresponding to the quantized energies of the system), and the eigenvectors (whose total set forms a complete basis of the space of states). This approach leads to encounter the notion of photon, the most emblematic concept of quantum optics.

To start, the quantized Hamiltonian describing the electromagnetic field in the mode ℓ should be written:

$$\hat{H}_\ell = \hbar\,\omega_\ell\Big(\hat{a}_\ell^\dagger \hat{a}_\ell + \tfrac{1}{2}\Big)\ \big[\,\hat{a}_\ell, \hat{a}_\ell^\dagger\,\big] = 1.$$

As already reported, this corresponds to the Hamiltonian of a harmonic oscillator. The solution applied to the mode ℓ will now be derived. The eigenequation is:

$$\hat{H}_\ell \left|\varphi_{n_\ell}\right\rangle = E_{n_\ell}\ \left|\varphi_{n_\ell}\right\rangle$$

and its eigenvalues are:

$$E_{n_\ell} = \hbar\,\omega_\ell\left(n_\ell + \tfrac{1}{2}\right) \qquad \text{with } n_\ell = 0, 1, 2, \ldots.$$

n_ℓ is a non negative integer. The eigenstates obey these remarkable relations which connect the various eigenstates to each other:

$$\hat{a}_\ell \left|\varphi_{n_\ell}\right\rangle = \sqrt{n_\ell}\ \left|\varphi_{\,n_\ell - 1}\right\rangle \hat{a}_\ell^\dagger \left|\varphi_{n_\ell}\right\rangle \ = \sqrt{n_\ell + 1}\ \left|\varphi_{\,n_\ell + 1}\right\rangle \qquad \Longrightarrow \qquad \left|\varphi_{n_\ell}\right\rangle = \frac{(\hat{a}_\ell^\dagger)^{n_\ell}}{\sqrt{n_\ell!}}\ \left|\varphi_{\,n_\ell = 0}\right\rangle.$$

A state playing a particular role is associated with $n_\ell = 0$. It corresponds to the state with the lowest energy and it is determined by the equation:

$$\hat{a}_\ell \left|\varphi_{\,n_\ell = 0}\right\rangle = 0$$

where the destruction operator, $\hat{a}$ is used. From the vacuum state all the other states can be generated by applying N times the creation operator and normalization procedures. A complete basis of the state space is thus obtained. It is worth noting that the eigenstates of the Hamiltonian are eigenstates of the number operator N_ℓ. They are often noted as state $|n_\ell >$, and they are called *number states* or *Fock states* from the name of Vladimir Fock, a Russian theorist who developed this representation. These states are well suited to introduce the notion of photon as we see now. The number state $|n_l >$ has a well defined energy which is larger than the lowest possible energy by $n\hbar\omega_e ll$:

$$E_{n_\ell} = \hbar\,\omega_\ell\big(n_\ell + \tfrac{1}{2}\big)\,; \qquad E_0 = \frac{\hbar\,\omega_\ell}{2} E_{n_\ell} - E_0 = n_\ell\,\hbar\,\omega_\ell.$$

The classical electromagnetic field has also momentum, which can be considered responsible for radiation pressure when a beam is absorbed or reflected. As for the energy, it depends on the volume of quantization and it is given by:

$$\mathbf{P}_\ell = \varepsilon_0 \int_{V_\ell} \mathrm{d}^3\mathbf{r}\ (\mathbf{E} \times \mathbf{B}) = \left|\alpha_\ell\right|^2\ \hbar\,\mathbf{k}_\ell.$$

The corresponding quantized observable associated with the momentum in the volume of quantization is:

$$\hat{\mathbf{P}}_\ell = \hbar\,\mathbf{k}_\ell\,\hat{a}^\dagger_\ell\hat{a}_\ell.$$

As for the Hamiltonian, the number state n_ℓ is also an eigenstate of the momentum operator, with eigenvalue $n_\ell\hbar k_\ell$. Finally, the state $|n_\ell >$ has well defined energy $n_\ell\hbar\omega_\ell$, and a well defined momentum, $n_\ell\hbar k_\ell$. It has thus the same energy and momentum as n_ℓ particles, each with energy $\hbar\omega_\ell$ and momentum $\hbar k_\ell$. These particles are called *photons.*

Concerning momentum: firstly, the formula used is valid only for running waves. If you have quantized on other types of modes, for instance, standing waves, this formula does not hold. Secondly, if the rest mass is computed by using the well known relativistic formula:

$$m^2c^4 = E^2 - P^2c^2 = (\hbar\,\omega_\ell)^2 - (\hbar\,k_\ell)^2c^2 = 0$$

hence in special relativity a massless particle travels at the speed of light.

5.1.3.1 Vacuum state and vacuum fluctuations

A special note should be done to the lowest number state associated with zero photon, the so-called *vacuum.* Normally, it is thought as the absence of everything, in particular, the absence of radiation. This is true in classical physics. But in quantum physics, the state with zero photon has a remarkable property that has physical consequences: the electromagnetic field is not null, it has fluctuations. It is possible to calculate the average of the electric field operator E in vacuum state 0:

$$\langle 0_\ell|\hat{\mathbf{E}}(\mathbf{r},t)|0_\ell\rangle$$

with

$$\hat{\mathbf{E}}(\mathbf{r},t) = i\,\vec{\varepsilon}_\ell\,\mathcal{E}^{(1)}_\ell\left(\hat{a}_\ell\,e^{\,i\,\mathbf{k}_\ell\mathbf{r}} - \hat{a}^\dagger_\ell\,e^{-\,i\,\mathbf{k}_\ell\mathbf{r}}\right).$$

The average is found null because $\hat{a}$ applied to $|0_\ell\rangle >$ gives 0 and similarly for $\hat{a}^\dagger$ applied to $\langle 0_\ell|$ on the left::

$$\hat{a}_\ell\,|0_\ell\rangle = 0 \quad \text{and} \quad \langle 0_\ell|\,\hat{a}^\dagger_\ell = 0.$$

However, a null average does not necessarily mean that the quantity is null. It can be spread around 0. To check this possibility, the average of the squared electric field in the vacuum is computed:

$$\langle 0_\ell|\hat{\mathbf{E}}^2|0_\ell\rangle = \left[\mathcal{E}^{(1)}_\ell\right]^2\langle 0_\ell|\hat{a}_\ell\hat{a}^\dagger_\ell|0_\ell\rangle = \left[\mathcal{E}^{(1)}_\ell\right]^2$$

$$\Delta E = \left(\langle 0_\ell|\hat{\mathbf{E}}^2|0_\ell\rangle - \left\|\langle 0_\ell|\hat{\mathbf{E}}|0_\ell\rangle\right\|^2\right)^{1/2} = \mathcal{E}^{(1)}_\ell$$

because

$$\hat{a}_\ell\hat{a}^\dagger_\ell = 1 + \hat{a}^\dagger_\ell\hat{a}_\ell.$$

Therefore, the electric field has a dispersion; the term fluctuations is also used. The root mean square value of the fluctuations has an amplitude $\mathcal{E}^{(1)}$, i.e. the one photon electric field. In fact, as in the case of the material harmonic oscillator, this fluctuation can be linked to the fluctuation of the conjugate canonical observables, Q_ℓ and P_ℓ. As shown here, the electric field can be expressed as a function of Q_ℓ and P_ℓ by expanding the exponentials, $i \cdot k \cdot r$, and using the expression of Q_ℓ and P_ℓ:

$$\hat{\mathbf{E}}(\mathbf{r}) = \vec{\varepsilon}_\ell\,\mathcal{E}^{(1)}_\ell\Big(i(\hat{a}_\ell - \hat{a}^\dagger_\ell)\cos(\mathbf{k}_\ell{\cdot}\mathbf{r}) - (\hat{a}_\ell + \hat{a}^\dagger_\ell)\sin(\mathbf{k}_\ell{\cdot}\mathbf{r})\Big) = \vec{\varepsilon}_\ell\,\mathcal{E}^{(1)}_\ell\sqrt{\frac{2}{\hbar}}\Big(\hat{P}_\ell\cos(\mathbf{k}_\ell{\cdot}\mathbf{r}) - \hat{Q}_\ell\sin(\mathbf{k}_\ell{\cdot}\mathbf{r})\Big).$$

Let us now calculate the fluctuation of Q_ℓ and P_ℓ, whose averages are null in the vacuum:

$$\hat{Q}_\ell = \sqrt{\frac{\hbar}{2}}(\hat{a}_\ell + \hat{a}^\dagger_\ell), \qquad \langle 0_\ell|\hat{Q}_\ell|0_\ell\rangle = 0$$

$$\hat{P}_\ell = -\,i\sqrt{\frac{\hbar}{2}}(\hat{a}_\ell - \hat{a}^\dagger_\ell), \qquad \langle 0_\ell|\hat{P}_\ell|0_\ell\rangle = 0.$$

Eventually, their dispersions are:

$$\Delta Q_\ell = \sqrt{\frac{\hbar}{2}},$$

$$\Delta P_\ell = \sqrt{\frac{\hbar}{2}}.$$

hence their product is:

$$\Delta Q_\ell \, \Delta P_\ell = \frac{\hbar}{2}.$$

i.e. the minimum value permitted by the Heisenberg relation. The vacuum is thus a minimum dispersion state.

Alternatively, the vacuum is the state in which the fluctuations have the minimum value compatible with the Heisenberg relation. The fact that the electromagnetic field has fluctuations in the vacuum has remarkable consequences emblematic of quantum physics. First, the vacuum fluctuations are responsible of the fact that an atom in a level that is not the ground state will eventually decay by spontaneous emission. Even in the vacuum, the atom is not isolated. It is coupled to the quantized field and its fluctuations. Vacuum fluctuations have also an effect on the position of the energy levels of the atom, which are slightly modified compared to what is calculated in the absence of the coupling to the quantized electromagnetic field. This slight modification is called the Lamb shift, from the name of Willis Lamb, who measured that shift in the hydrogen atom with his collaborator Retherford. This measurement was a masterpiece of experimental physics, just after World War II. The result remarkably agreed well with the calculation based on quantum electrodynamics theory just developed by Feynman, Schwinger, and Tomonaga. Nowadays, more and more precise measurement of the Lamb shift of various level of the hydrogen atom are still one of the best benchmark of QED, the quantum electrodynamics theory. Other effects due to vacuum fluctuations are the Casimir effect i.e. the attraction between two metallic plates close to each other or a small anomaly in the magnetic moment of the electron linked to the spin 1/2 of this particle.

5.1.3.2 One-photon state

As another special state the one-photon state will be now analyzed. The average value of the electric field in the one-photon state:

$$|1_\ell\rangle = |\, n_\ell = 1\, \rangle$$

is

$$\big\langle 1_\ell | \hat{\mathbf{E}}(\mathbf{r}) | 1_\ell \big\rangle = 0$$

being

$$\hat{\mathbf{E}}(\mathbf{r}) = i\, \vec{\varepsilon}_\ell \, \mathcal{E}_\ell^{(1)} \left(\hat{a}_\ell \, e^{i\,\mathbf{k}_\ell \mathbf{r}} - \hat{a}_\ell^\dagger \, e^{-i\,\mathbf{k}_\ell \mathbf{r}} \right).$$

In fact, $\hat{a}$ applied to the one-photon state yields an orthogonal state so the average of $\hat{a}$ in the one-photon state is null:

$$\hat{a}_\ell \, |1_\ell\rangle = |0_\ell\rangle \quad \text{and} \quad \langle 1_\ell | 0_\ell \rangle = 0 \implies \langle 1_\ell |\, \hat{a}_\ell \, | 1_\ell \rangle = 0.$$

Similarly, the average of $\hat{a}^\dagger$ in state one is null:

$$\big\langle 1_\ell | \hat{a}_\ell^\dagger | 1_\ell \big\rangle = 0.$$

A null result would also be obtained as the average value of any quadrature component. The question raises if the field is null in a one-photon state. As in the case of vacuum, in order to answer this question the average of the square of the electric field should be computed:

$$\langle 1_\ell | \hat{\mathbf{E}}^2 | 1_\ell \rangle = \big[\mathcal{E}_\ell^{(1)}\big]^2 \big\langle 1_\ell | \hat{a}_\ell^2 + (\hat{a}_\ell^\dagger)^2 + \hat{a}_\ell \hat{a}_\ell^\dagger + \hat{a}_\ell^\dagger \hat{a}_\ell | 1_\ell \big\rangle = \big[\mathcal{E}_\ell^{(1)}\big]^2 \big\langle 1_\ell | \hat{a}_\ell \hat{a}_\ell^\dagger + \hat{a}_\ell^\dagger \hat{a}_\ell | 1_\ell \big\rangle.$$

When electric field operator is squared, a term $\hat{a}^\dagger$ squared is obtained, which gives the state $n = 3$, orthogonal to the state $n = 1$; therefore its contribution is null. Similarly, the term $\hat{a}$ squared has a null average. We are thus left with the average of $\hat{a}^\dagger \hat{a} + \hat{a}\hat{a}^\dagger$. Using the commutator:

$$\hat{a}_\ell \hat{a}_\ell^\dagger = 1 + \hat{a}_\ell^\dagger \hat{a}_\ell$$

the average can be written as:

$$\langle 1_\ell|\hat{\mathbf{E}}^2|1_\ell\rangle = \left[\mathcal{E}_\ell^{(1)}\right]^2\langle 1_\ell|1 + 2\,\hat{a}_\ell^\dagger\hat{a}_\ell|1_\ell\rangle = 3\left[\mathcal{E}_\ell^{(1)}\right]^2$$

i.e. 3 times the square of the one-photon amplitude. The electric field can then be thought as a fluctuating quantity and its fluctuations have magnitude of $\mathcal{E}^{(\infty)}$ times $\sqrt{3}$.

It is useful now to add information to the observables $\hat{Q}_\ell$ and $\hat{P}_\ell$. They are analogous to the position and momentum of a harmonic oscillator within multiplying constants. The average value is also null in a one photon state because the average of $\hat{a}$ or $\hat{a}^\dagger$ is null in a number state:

$$\hat{Q}_\ell = \sqrt{\frac{\hbar}{2}}(\hat{a}_\ell + \hat{a}_\ell^\dagger) \qquad \langle 0_\ell|\hat{Q}_\ell|0_\ell\rangle = 0 \qquad \Delta Q_\ell = \sqrt{3}\sqrt{\frac{\hbar}{2}}$$

$$\hat{P}_\ell = -\,i\sqrt{\frac{\hbar}{2}}(\hat{a}_\ell - \hat{a}_\ell^\dagger) \qquad \langle 0_\ell|\hat{P}_\ell|0_\ell\rangle = 0 \qquad \Delta P_\ell = \sqrt{3}\sqrt{\frac{\hbar}{2}}$$

hence:

$$\Delta Q_\ell\,\Delta P_\ell = \frac{3\,\hbar}{2}.$$

Hence, the one-photon state is not a minimum dispersion state. This is true for any number state except for vacuum.

It is important to underline a potential problem, i.e. the fact that $\mathcal{E}^{(\infty)}$ seems to depend on the arbitrary volume of quantization:

$$\mathcal{E}_\ell^{(1)} = \sqrt{\frac{\hbar\,\omega_\ell}{2\,\varepsilon_0\,V_\ell}}$$

In a real experiment, it is possible, at least in principle, to measure the average of E squared and this measurement will give a well defined result. So the result of the calculation should not depend on the arbitrary value of the volume of quantization. The solution of this paradox lies on the fact that real one-photon states come in wave packets of finite extension. For instance, when a single atom in an excited state emits one photon, the emitted radiation is not stationary. It has a time dependence. It is null before the emission starts and decays to zero exponentially after the start of the emission. It involves several modes of the radiation associated with several different frequencies. It is a similar situation as the Fourier transform of a time varying function involving several frequencies. So in principle, to study one-photon state, the formalism of multimode radiation states should be introduced. It is useful to introduce first a simplified model of a single mode one-photon state. This model is not entirely rigorous but it captures the quantum features useful at this stage. The model is the following: firstly, a traveling plane wave that has a limited transverse S determined by the experimental setup is introduced (Fig. 5.1). For instance, almost all light emitted by a single atom is collected by using a parabolic mirror with the atom at its focus. If S is much larger than the square of the wavelengths of light, diffraction is negligible and it is not a bad approximation to think of a plane wave with a constant transverse section. For instance, yellow-orange visible light has a wavelength of $0.6\mu m$ a beam with a section of one squared centimeter has negligible diffraction over hundreds of meters of propagation. An additional assumption is constant amplitude in the transverse section; this is not very realistic but it significantly simplifies the calculation without modifying the physics.

$$S_\ell \gg \lambda^2\,; \quad \lambda \sim 0.6\,\mu\text{m}.$$

Secondly, we think of a traveling plane wave with a limited temporal duration T which evokes, for instance, a finite lifetime of the emitting excited level. The amplitude slowly rises to its steady-state value and it slowly falls to zero after a duration T. This allows for the frequency spread to be negligible compared to the radiation frequency, provided that the rise and fall times are long compared to the period of the oscillating field. This is possible if the duration T is very large compared to the period of oscillation. Let us take again the example of a single atom emitting visible light at frequency $\sim 5\times10^{14}$ hertz. The duration of the emission of the one-photon wave packet is always larger than a few nano seconds, more than one million of oscillation periods. The wave packet has a length:

$$L = cT_\ell$$

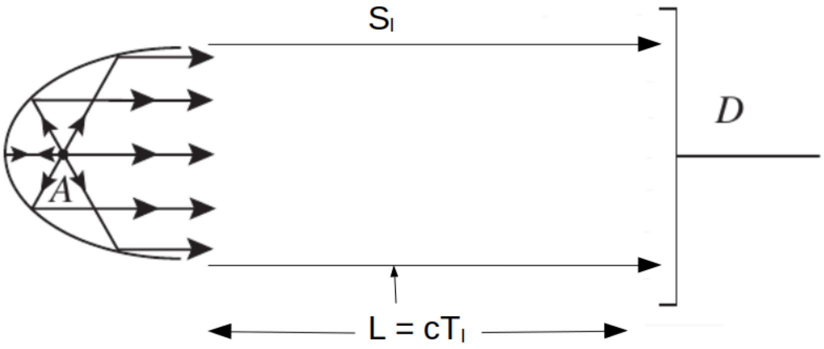

Figure 5.1: Quantization volume: experimental setup. A single atom A is placed at the focus of a parabolic mirror. It emits a collimated one-photon wave packet, fully detected by D. Figure adapted from [203].

being c the speed of light. For instance, if $T = 10$ ns light travels only for three meters, that is significantly less than the distance after which diffraction becomes significant (hundreds of meters in the example given above). The mode ℓ has then a quantization volume $S_\ell c T_\ell$ that has a physical meaning.

The number of photons in that mode is well defined and it can be measured in principle with the detector D wider than S_ℓ, integrating the signal over a period of time longer than the wave packet duration T. The infinitesimal probability to measure a one-photon wave packet can be expressed as:

$$dP(\mathbf{r},t) = w^{(1)}(\mathbf{r},t)\, dS\, dt.$$

5.2 Photo-detection signals and Glauber's photodetection formulae

In the 1960s Roy Glauber established the formalism of quantum optics. Among the most important features of this formalism, the formulae to express photo-detection signals for any state of the quantized radiation should be mentioned. In the following, these equations will be listed and described, and the outcome of applying these formulae to the case of one photon wave packet will be given. Glauber established the expressions of the photo-electric detection signals, with quantized radiation by using the expression of the interaction Hamiltonian between quantized radiation and a quantized detector. That is to say an atom with a series of discrete levels and a continuum of ionized states. This interaction Hamiltonian resembles the semi-classical one. But in fact, it dramatically differs. Both quantities are quantized, not only the atom, but also the electric field represented here by the operator $\hat{E}$. Clearly, the physical effect is the same, it does not change when different mathematical tools are used to describe it. Indeed, under the effect of the interaction, a bound electron is excited to the continuum leaving the atom. With an electron multiplier we can then obtain a detectable electric pulse for each released electron. Glauber's formulae read:

$$w^{(1)}(\mathbf{r},t) = s \left\langle \psi(t) \right| \hat{\mathbf{E}}^{(-)}(\mathbf{r})\, \hat{\mathbf{E}}^{(+)}(\mathbf{r}) \left| \psi(t) \right\rangle$$

with:

$$\hat{\mathbf{E}}^{(+)}(\mathbf{r}) = i \sum_{\ell} \vec{\varepsilon}_\ell\, \mathcal{E}_\ell^{(1)}\, \hat{a}_\ell\, e^{i\,\mathbf{k}_\ell \mathbf{r}}$$

$$\hat{\mathbf{E}}^{(-)}(\mathbf{r}) = -\,i \sum_{\ell} \vec{\varepsilon}_\ell\, \mathcal{E}_\ell^{(1)}\, \hat{a}_\ell^{\dagger}\, e^{-\,i\,\mathbf{k}_\ell \mathbf{r}}.$$

$\hat{\mathbf{E}^{(+)}}$ is the part of the electric field operator involving the destruction operators $\hat{a}_\ell$. The operator $\hat{\mathbf{E}^{(-)}}$ is its hermitian conjugate involving the creation operators $\hat{a}_\ell^{\dagger}$. The electric field operator is split as:

$$\hat{\mathbf{E}}(\mathbf{r},t) = \hat{\mathbf{E}}^{(+)}(\mathbf{r},t) + \hat{\mathbf{E}}^{(-)}(\mathbf{r},t), \tag{5.26}$$

where the superscripts refer to time dependence ($^{-i\omega t}$ vs."$^{+i\omega t}$), *not* to creation/annihilation per se. For a plane-wave mode ℓ:

$$\hat{\mathbf{E}}^{(+)}(\mathbf{r},t) = i\sqrt{\frac{\hbar\omega_\ell}{2\epsilon_0 V_\ell}}\,\boldsymbol{\epsilon}_\ell\,\hat{a}_\ell\,e^{i(\mathbf{k}_\ell\cdot\mathbf{r}-\omega_\ell t)}, \tag{5.27}$$

$$\hat{\mathbf{E}}^{(-)}(\mathbf{r},t) = -i\sqrt{\frac{\hbar\omega_\ell}{2\epsilon_0 V_\ell}}\,\boldsymbol{\epsilon}_\ell^*\,\hat{a}_\ell^\dagger\,e^{-i(\mathbf{k}_\ell\cdot\mathbf{r}-\omega_\ell t)}. \tag{5.28}$$

Thus, $\hat{\mathbf{E}}^{(+)}$ *contains the annihilation operator* and $\hat{\mathbf{E}}^{(-)}$ *the creation operator*. This notation has been introduced by Glauber himself. The coefficient s is the sensitivity of the detector and its value can be obtained by a full calculation, provided the exact expressions of the electronic states in the detector are known.

In order to recover the value of s for an ideal detector, an insight should be proveded on the single and double probability of detection. $w^{(1)}$ can be written as:

$$w^{(1)}(\mathbf{r},t) = s\,\big\|\,\hat{\mathbf{E}}^{(+)}(\mathbf{r})\;|\psi(t)\rangle\,\big\|^2.$$

This expression may evoke its semiclassical version. A very important formula giving the rate of double detections around (r,t) and around (r',t) will be now introduced:

$$d^2P(\mathbf{r},t;\mathbf{r}',t') = w^{(2)}(\mathbf{r},t;\mathbf{r}',t')\,dS\,dt\,dS'\,dt'$$

with:

$$w^{(2)}(\mathbf{r},t;\mathbf{r}',t') = s^2\,\big\langle\psi(t)\big|\hat{\mathbf{E}}^{(-)}(\mathbf{r})\,\hat{\mathbf{E}}^{(-)}(\mathbf{r}')\,\hat{\mathbf{E}}^{(+)}(\mathbf{r}')\,\hat{\mathbf{E}}^{(+)}(\mathbf{r})\big|\psi(t)\big\rangle.$$

It is important to underline the order in which the electric field operators appear; one way to remember the ordering is to write this equation as the square modulus of $\mathbf{E}^{(+)}(r') \times \mathbf{E}^(+)(r)$ applied to the state $|\psi\rangle$:

$$w^{(2)}(\mathbf{r},t;\mathbf{r}',t) = s^2\,\big\|\,\hat{\mathbf{E}}^{(+)}(\mathbf{r}')\,\hat{\mathbf{E}}^{(+)}(\mathbf{r})\;|\psi(t)\rangle\,\big\|^2 = s^2\,\langle\psi(t)|\,\hat{\mathbf{E}}^{(-)}(\mathbf{r})\,\hat{\mathbf{E}}^{(-)}(\mathbf{r}')\,\hat{\mathbf{E}}^{(+)}(\mathbf{r}')\,\hat{\mathbf{E}}^{(+)}(\mathbf{r})\,|\psi(t)\rangle\,.$$

In contrast to the semi-classical formula, $w^{(2)}(\mathbf{r},\mathbf{r}')$ is not equal to the product of $w^{(1)}(\mathbf{r})$ and $w^{(1)}(\mathbf{r}')$:

$$w^{(2)}(\mathbf{r},t;\mathbf{r}',t) \neq w^{(1)}(\mathbf{r},t)\,w^{(1)}(\mathbf{r}',t).$$

The reason is that the first photo-detection destroys a photon, and thus changes the state of radiation before the second photon is detected. This is in contrast to classical physics, where it is implicitly assumed that the measurement can be gentle enough not to perturb the system to be observed.

An important piece of information can be obtained by applying these formulae to the case of one-photon state. The calculation is straightforward, since one mode only is involved:

$$w^{(1)}(\mathbf{r},t) = s\,\big\langle 1_\ell(t)\big|\,\hat{\mathbf{E}}^{(-)}(\mathbf{r})\,\hat{\mathbf{E}}^{(+)}(\mathbf{r})\,\big|1_\ell(t)\big\rangle$$

with

$$\hat{\mathbf{E}}^{(+)}(\mathbf{r}) = i\,\vec{\varepsilon}_\ell\,\mathcal{E}_\ell^{(1)}\,\hat{a}_\ell\,e^{i\,\mathbf{k}_\ell\mathbf{r}}$$

and

$$|1_\ell(t)\rangle = |1_\ell(t)\rangle\;e^{-i\omega_\ell t}.$$

The same result would have been obtained in the semi-classical model with the classical field of amplitude $E^{(1)}$. Remembering the expression of the one-photon amplitude:

$$w^{(1)}(\mathbf{r},t) = s\,\big[\mathcal{E}_\ell^{(1)}\big]^2\,\langle 1_\ell|\,\hat{a}_\ell^\dagger\hat{a}_\ell\,|1_\ell\rangle = s\,\big[\mathcal{E}_\ell^{(1)}\big]^2$$

$$w^{(1)}(\mathbf{r},t) = s\,\frac{\hbar\,\omega_\ell}{2\,\varepsilon_0\,V_\ell} = s\,\frac{\hbar\,\omega_\ell}{2\,\varepsilon_0\,S_\ell\,c\,T_\ell}$$

in which the quantization volume is involved. By integrating over the whole transverse section of the beam the probability photo-detection probability per unit-time $\frac{dP}{dt}$ photo-detection can be derived, with the detector covering the whole beam:

$$\frac{dP}{dt} = \iint_S dS\,w^{(1)}(\mathbf{r},t) = s\,\frac{\hbar\,\omega_\ell}{2\,\varepsilon_0\,c\,T_\ell}.$$

By integrating the differential probability over the whole duration T_ℓ of one-photon wave packet, the total probability to get one count over the whole one-photon wave packet can be recovered:

$$\int_{T_\ell} dt\,\frac{dP}{dt} = s\,\frac{\hbar\,\omega_\ell}{2\,\varepsilon_0\,c}.$$

For an ideal detector, this probability would be exactly one. An expression for the sensitivity of an ideal detector can be derived:

$$S_{\text{perfect}} = \frac{2\,\varepsilon_0\,c}{\hbar\,\omega_\ell}.$$

Non-ideal detectors have sensitivities smaller by a factor η called *quantum efficiency*:

$$\eta = \frac{s}{S_{\text{perfect}}} \leq 1$$

The rate of detection per unit time and unit of surface can then be re-written as:

$$w^{(1)}(\mathbf{r},t) = \eta\,\frac{1}{S_\ell\,T_\ell}.$$

Returning to the formula about single photo-detection signals $w^{(1)}$ there is something quite disappointing. All the results are exactly the same as with the classical wave packet of section S and duration T_ℓ, with the classical electric field amplitude $\mathcal{E}^{(1)}$ equal to the so-called one-photon amplitude:

- One photon wave packet

$$V_\ell = S_\ell\,c\,T_\ell \qquad \mathcal{E}_\ell^{(1)} = \sqrt{\frac{\hbar\,\omega_\ell}{2\,\varepsilon_0\,V_\ell}}$$

$$w^{(1)}(\mathbf{r},t) = s\,\langle 1_\ell(t)|\hat{\mathbf{E}}^{(-)}(\mathbf{r})\hat{\mathbf{E}}^{(+)}(\mathbf{r})|1_\ell(t)\rangle = s\,[\mathcal{E}_\ell^{(1)}]^2\,\langle 1_\ell|\hat{a}_\ell^\dagger\hat{a}_\ell|1_\ell\rangle = s\,[\mathcal{E}_\ell^{(1)}]^2$$

$$\mathcal{P} = \int_{T_\ell} dt \iint_S dS\,w^{(1)}(\mathbf{r},t) = \frac{V_\ell}{c}\,s\,[\mathcal{E}_\ell^{(1)}]^2 = s\,\frac{\hbar\,\omega_\ell}{2\,\varepsilon_0\,c} = \eta$$

- Classical wave packet

$$\mathbf{E}_\ell^{(+)}(\mathbf{r},t) = \vec{\varepsilon}_\ell\,\mathcal{E}_\ell^{(1)}\,\exp\{i(\mathbf{k}_\ell\cdot\mathbf{r} - \omega_\ell t)\} \,:\, S_\ell,\,T_\ell$$

$$w^{(1)}(\mathbf{r},t) = s\,\left|\mathbf{E}_\ell^{(+)}(\mathbf{r},t)\right|^2 = s\,[\mathcal{E}_\ell^{(1)}]^2 \implies \mathcal{P} = \eta$$

Hence, when modelling single-photon detection, a fully quantum-optical formalism is not strictly required. However, a full quantum description must be used when addressing non-classical states and higher-order correlations (e.g., in the case of coincidence measurements of photons and multi-photon interference), as described in the following section.

5.3 A fully quantum behaviour: double photo-detection signal for a one-photon state

Till 1970s, no evidence was claiming for the necessity to use a full quantum optics formalism; until a double photo-detection signal was detected for a one-photon state. The starting point is the formula for double detection applied to the case of a one-photon state in a single mode ℓ:

$$w^{(2)}(\mathbf{r},t;\mathbf{r}',t) = s^2\,\left\|\,\hat{\mathbf{E}}_\ell^{(+)}(\mathbf{r}')\,\hat{\mathbf{E}}_\ell^{(+)}(\mathbf{r})\,|1_\ell\rangle\,\right\|^2.$$

Being a number state a stationary state, it evolves as a complex exponential of time, which disappears when taking the square modulus: The same happens for the complex exponentials associated

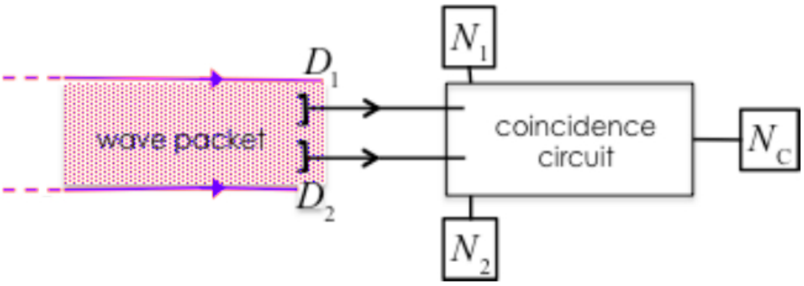

Figure 5.2: Experimental setup to measure single and double photo-detection signals. Figure adapted from the course by Alain Aspect.

with the positions $\mathbf{r}$ and $\mathbf{r}'$ where the electric field operators are taken. So the rate of double detection neither depends on time nor on position. It is constant in the volume of the wave packet. Indeed, this is a result of the model being a uniform wave packet in the volume ScT. Expressing the operator $\hat{\mathbf{E}}^{(+)}$ as a function of the destruction operator $\hat{a}$, it comes out that the result is obtained by applying twice the annihilation operator to the one-photon state vector.

$$w^{(2)}(\mathbf{r},t;\mathbf{r}',t) = s^2\,[\mathcal{E}_\ell^{(1)}]^2 \left\| \hat{a}_\ell \hat{a}_\ell \left|1_\ell\right\rangle \right\|^2$$

$$\hat{a}_\ell \left|1_\ell\right\rangle = \left|0_\ell\right\rangle, \qquad \hat{a}_\ell \left|0_\ell\right\rangle = 0$$

$$w^{(2)}(\mathbf{r},t;\mathbf{r}',t) = s^2 \left\| \hat{\mathbf{E}}_\ell^{(+)}(\mathbf{r}')\hat{\mathbf{E}}_\ell^{(+)}(\mathbf{r}) \left|1_\ell\right\rangle \right\|^2 = 0.$$

$\hat{a}$ applied to one returns a vacuum state, that is a number state associated with zero photon. A perfectly legitimate state whose modulus is one. However, when applying another time $\hat{a}$ to the zero photon state, the number 0 is returned as result. Therefore, the probability of a double detection is null.

It is possible to measure single and double photo-detection signals as shown in Fig. 5.2. Two detectors positioned in the light beam are connected to an electronic circuit that monitors and counts the pulses. It also registers coincidences: they occur when the two detectors D_1 and D_2 click simultaneously (i.e. during the same time window which can be chosen at will). In this case, a coincidence window equal to the duration of the wave packet is chosen, so that the coincidence counter registers an event if the two detectors click during the same wave packet. The experiment is repeated for a large number of times. N_{wp} indicated the number of wave packets "flowing" during the experiment. The number of counts N_1 on the first detector D_1 can be expressed as:

$$N_1 = w^{(1)}\, S_1\, T_\ell\, N_{\mathrm{wp}},$$

i.e. the toatl number of counts on detector D_1 is given as the product among the average number of detections $w^{(1)}$, the area of the detector S_1, the duration of the wave packet T_ℓ and the number of wave packets. Similarly, the number of counts N_2 on the second detector D_2 can be expressed as:

$$N_2 = w^{(1)}\, S_2\, T_\ell\, N_{\mathrm{wp}}.$$

The number of coincidences during a wave packet is:

$$N_C = w^{(2)}\, S_1 S_2\, T_\ell^2\, N_{\mathrm{wp}}.$$

For a one-photon wave packet, the expressions for $w^{(1)}$ and $w^{(2)}$ have been previously recovered:

$$\text{One photon state: } w^{(2)} = 0$$

$$N_1 = \eta\,\frac{S_1}{S_\ell}\,N_{\mathrm{wp}} \qquad N_2 = \eta\,\frac{S_2}{S_\ell}\,N_{\mathrm{wp}} \qquad N_C = 0.$$

Summarizing:

$$N_C = 0\ ;\ N_1 \neq 0\ ;\ N_2 \neq 0.$$

$w^{(2)}$ is then null, since one cannot detect twice a single photon; the number of coincidences is null.

This result of a null coincidence rate is surprising from the point of view of traditional optics. Indeed, the prediction of the semi-classical model for a classical wave packet is different. In particular, in the semi-classical case, $w^{(2)}$ equals $(w^{(1)})^2$:

$$w^{(2)} = \left[w^{(1)}\right]^2.$$

With a constant amplitude over the wave-packet volume, the formulae of the semi-classical model give constant rates of single and double photo-detections:

$$N_1 = w^{(1)} S_1 T_\ell N_{\mathrm{wp}} \qquad N_2 = w^{(1)} S_2 T_\ell N_{\mathrm{wp}}$$

After integration over the size S_1 and S_2 of the detectors and over the whole duration of the wave-packet, the total number of single counts and of coincidences during each wave-packet can be obtained multiplying by the number of wave-packets:

$$N_C = w^{(2)} S_1 S_2 T_\ell^2 N_{\mathrm{wp}} = \frac{N_1 N_2}{N_{\mathrm{wp}}} \neq 0.$$

The single counts expression closely resembles the ones obtained with the semi-classical model. But the result is dramatically different when it comes to the coincidences, since it is not null. In particular, this result is independent of the amplitude of the classical field and remains unchanged, even with extremely weak classical wave-packets. These calculations show that there are situations where quantum optics must be used.

The absence of double photo-detection in the case a one-photon wave-packet is an emblematic example of a fully quantum phenomeno.

For this peculiar feature, this fully quantum property can be used in one of the simplest examples of quantum technology: quantum cryptography with one-photon wave packets. A quantum technology is a technology enabled by the fundamental laws of quantum physics, and it would fail if nature was described by classical physics. The simplest scheme was invented by Charles Bennett and Giles Brassard in 1984 [204]. However, it took a long time before it was recognized as an interesting and useful scheme. This happened in 1991 when Artur Ekert published another quantum cryptography scheme based on entanglement [205] drawing attention onto the initial scheme by Bennet and Brassard, now known as *BB84*. Quantum cryptography is nowadays available as commercial devices, and it has already been used in official tasks such as transmitting the results of votes for political elections in Switzerland.

5.4 Operational principle of the on-chip single-photon spectrometer

An integrated single-photon spectrometer has been recently fabricated and published in Nature [82]. It consists of a fully integrated on-chip spectrometer covering the visible and infrared spectral range (600 nm – 2000 nm). Spectral separation (dispersion) is achieved by an integrated echelle grating fabricated in a dielectric material (Si_3N_4), which spatially separates photons according to their wavelength. Photon detection is performed by a single superconducting nanowire (Superconducting Nanowire Single-Photon Detector - SNSPD), which simultaneously acts as a single-photon detector and as a very slow microstrip delay line (see Fig. 5.4). In normal operating conditions, a DC current called *bias current* I_{bias} flows uniformly along the superconducting nanowire. This current is set right below the *critical current* I_c, i.e. the maximum current that can be sustained while preserving the superconducting state. When a photon is absorbed in such a superconductive device, its energy breaks Cooper pairs and creates a localized resistive hotspot. This interrupts superconductivity in a small segment of the nanowire, forcing the bias current to redistribute. The resulting electromagnetic trìggers the propagation of *two counter-propagating voltage pulses* along the nanowire.

The nanowire behaves as a transmission line characterized by a distributed kinetic inductance L_k and capacitance per unit length C'. The propagation speed of the pulses is

$$v = \frac{1}{\sqrt{L_k C'}} \ll c. \tag{5.29}$$

Let L be the nanowire length and x the photon absorption point measured from end A (Fig. 5.3). The two arrival times at the readout ends are then:

$$t_A = \frac{x}{v}, \qquad t_B = \frac{L - x}{v}, \tag{5.30}$$

leading to the measurable arrival-time difference:

$$\Delta t = t_A - t_B = \frac{2x - L}{v}, \qquad \Longrightarrow \qquad x = \frac{v}{2}\Delta t + \frac{L}{2}. \tag{5.31}$$

Because the on-chip dispersive grating maps each wavelength to a specific absorption position,

$$x = x(\lambda), \tag{5.32}$$

a calibration function f allows direct wavelength estimation from timing:

$$\lambda = f(x) = f\left(\frac{v}{2}\Delta t + \frac{L}{2}\right). \tag{5.33}$$

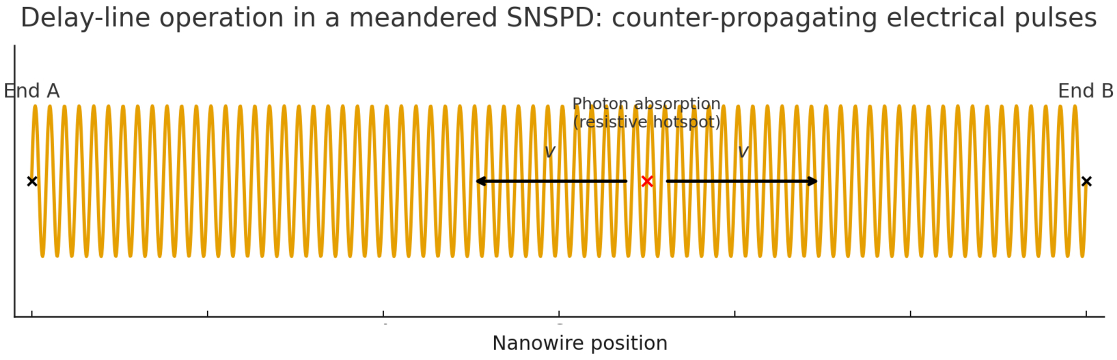

Figure 5.3: Conceptual scheme of time-encoded wavelength discrimination.

This delay-line encoding scheme forms the basis of integrated single-photon spectrometers with temporal multiplexing, allowing each detection event to yield both a photon *click* and a wavelength measurement.

This configuration allows encoding the photon wavelength into the detection time or detection position along the nanowire. The operational principle can be summarized as follows: photons enter the device, they are dispersed by the grating (so that different wavelengths propagate to different positions on the chip), the nanowire registers the detection event, and the timing/position of the click (one-photon detection) is used to infer the wavelength of the detected single photon.

Thus, the device combines two key elements: on one hand, single-photon detection (otherwise referred to as discrete "clicks") is ensured by the quantization of the electromagnetic field. On the other hand, modal/spatial encoding of the field enables discrimination of wavelength based on detection position or arrival time.

In this integrated spectrometer, a trade-off occurs: increasing L improves spectral resolution but increases detector dead time and timing jitter sensitivity.

5.4.1 Room-temperature perspective: SPAD-based single-photon readout

The single-photon spectrometer concept discussed in the previous section relies on superconducting nanowire single-photon detectors (SNSPDs). While this option provides excellent timing performance, the drawback relies on the necessity to have cryogenic operation condition [206]. The question arises whether a room-temperature single-photon detector could enable a similar spectroscopic functionality. In this direction, single-photon avalanche diodes (SPADs) might be promising devices to be included in integrated spectrometers in order to achieve this aim. Recent progress in waveguide-integrated single-photon avalanche diodes (SPADs), including Ge/Si devices compatible with silicon photonics platforms, motivates exploring room-temperature alternatives [207], [208].

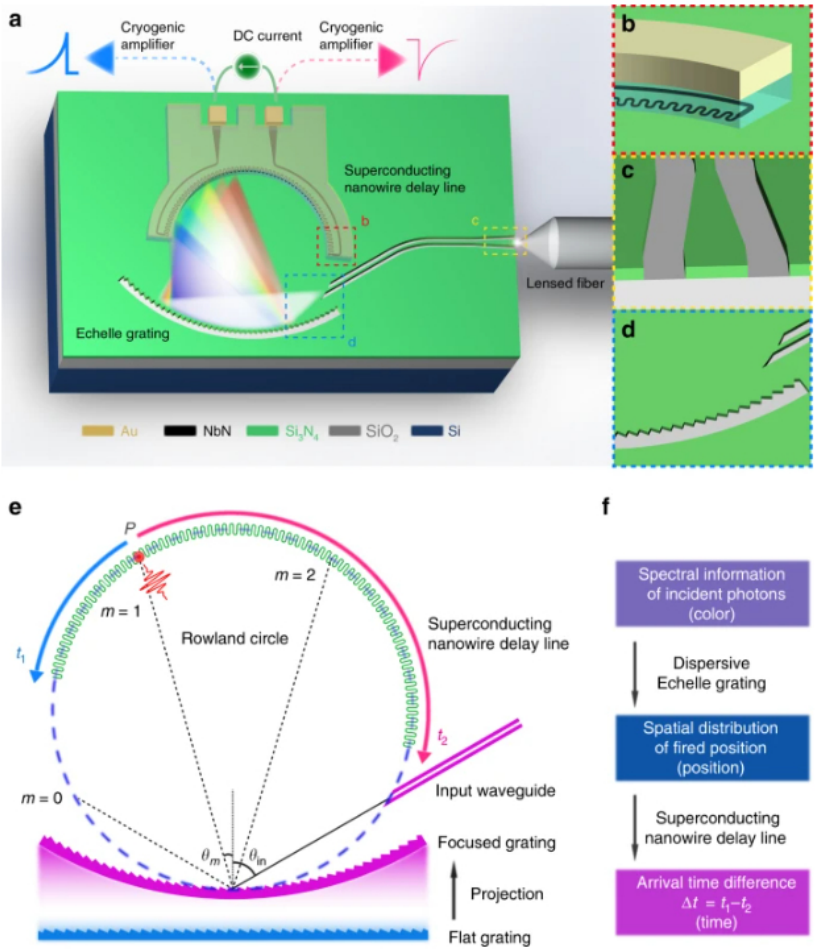

Figure 5.4: On-chip spectrometer by Cheng et al. [82]. It is based on an Echelle grating and a Rowland circle, together with a Superconducting Nanowire Single-Photon Detector (SNSPD). The latter allows for single-photon detection and delay line. The meandered layout increases the nanowire length while keeping a small footprint, enabling high spectral resolution within a compact area. The propagation speed of the pulses v is engineered to be much slower than c through the nanowire kinetic inductance and dielectric environment, enabling precise time discrimination. A single detector element thus enables multi-channel single-photon spectroscopy. Figure from [82].

It is important to note that the SNSPD-based architecture considered above exploits a distributed detection mechanism that can be interpreted as a “detector-delay-line” readout: the absorption position is inferred from timing information and eventually the wavelength is derived after including a dispersive mapping. On the other hand, a waveguide-integrated single photon avalanche diode (SPAD) is typically a point-like detector that provides photon-count events; for this reason, it does not give a direct access to a continuous position coordinate. Therefore, a room-temperature version of the single-photon spectrometer previously described would require a different readout strategy.

In the context of this thesis, a particularly suitable room-temperature route is to combine SPAD photon counting with a digitally scanned integrated spectrometer. Specifically, the Vernier-based cascaded-ring architecture discussed in Chapter 2 can be used in the photon-counting regime by replacing power measurements with photon-count acquisition for each discrete tuning [192]. For a given digital state s and integration time T, the measured photon counts follow Poisson statistics; hence, it depends on the signal count rate transmitted by the Vernier filter in state s and on the SPAD dark count rate. In this scanning approach, the wavelength information is encoded by the filter state (i.e., by the spectral window selected by the Vernier tuning), while the SPAD provides a direct estimate of the transmitted photon flux through the measured count rate.

The key features allowing for the feasibility and the performance of such a room-temperature approach rely on the overall optical throughput of the chip and by detector parameters (e.g. photon detection efficiency (PDE), dark counts, dead time). In particular, when the signal count rate transmitted by the filter is comparable to or below the SPAD dark count rate, the system requires longer integration times in order to achieve a target signal-to-noise ratio below the counting noise. Conversely, for sufficiently high throughput and PDE, the SPAD-based readout can provide a practical alternative route to single-photon spectrometry without cryogenic operation. A quantitative assessment of these trade-offs, including the expected insertion losses of the scanned filter, is left as a promising direction for future work.

The SPAD-based room-temperature option does not necessarily require a full quantum-optics treatment. In order to assess the feasibility of a digitally scanned (Vernier/ring-based) SPAD coupled spectrometer, the photonic circuit can be modelled with its classical transfer function and the detector output can be described through photon-counting (Poisson) statistics including dark counts and dead time. On the other hand, a fully quantum-optical formalism is required when the input field is in a purely non-classical state or when higher-order correlations (e.g., coincidence measurements) must be predicted.

Conclusions

In this PhD work the topic of integrated optical spectrometers has been addressed, with a particular focus on the miniaturization of optical spectrometers. In Chapter 1, a unified overview of the solutions reported in the literature was presented, organized both by operating principle (dispersive, interferometric/FTS, and reconstructive spectrometers) and by technology platform (silicon photonics, hybrid approaches, reconfigurable materials). This framework was used to place the devices proposed in the following chapters within a consistent context. In addition, a collaborative project to collect performance metrics of integrated spectrometers and detectors was suggested: `https://github.com/carlamariacoppola/iPHAOS`.

The first original contribution of this work is described in Chapter 2, where a Vernier on-chip spectrometer is proposed. Starting from the idea of using two cascaded ring resonators with slightly different free spectral ranges, the device achieves an effective increase in spectral resolution without a proportional increase in footprint. This is obtained with a layout that can be fabricated on standard silicon-photonics platforms (i.e. foundry-compatible). The Vernier algorithm is described in detail and all the relevant equations are derived analytically. The chapter also discusses the sensitivity to fabrication tolerances and thermal drifts, and identifies the conditions under which the Vernier operation remains valid.

Chapter 4 presents the second original contribution of the thesis, namely a reconstructive spectrometer in which the spectral response of the chip is intentionally designed to be numerically inverted. Although the architecture is reminiscent of the Vernier spectrometer, the underlying operating principle is different. Simulations show which combinations of integrated building blocks (resonators, paths with different optical path difference, thermally tunable elements) yield a filter matrix that is closer to the ideal one. Moreover, several reconstruction methods have been analysed in order to select the most robust under realistic conditions (noise, drift, need for calibration). This is where the added value of this contribution lies with respect to purely theoretical treatments.

A key role is played by Chapter 3, which reports the experimental measurements carried out at the University of Southampton. These measurements were performed on a Fourier-transform spectrometer previously designed by the research group within which this PhD work was conducted. Both passive and active measurements were carried out on several samples. This made it possible to demonstrate that phase-shifted Bragg gratings can be effectively used as tunable elements in on-chip spectrometers, while also showing that a better design of the spiral section is required in order to reduce the experimentally observed losses.

Finally, the thesis discusses the more demanding case of an on-chip single-photon spectrometer, for which a short introduction to the main concepts and phenomena of quantum optics is provided in order to clarify the operating principles of these edge-case spectrometers.

Acknowledgments

This PhD research period came about somewhat by chance. I was actually in the process of stepping away from academia, after completing my first PhD in 2010 and spending a long time as a fixed-term researcher.

By chance I came across an announcement for PhD positions at the Polytechnic University of Bari, in a post by Prof. Francesco Dell'Olio. In just one night I decided to embark on this new academic path. I would therefore like to thank Prof. Dell'Olio for encouraging me to apply for the PhD programme and for introducing me to the research group of Prof. Passaro, supervisor of this thesis. It was truly exciting for me to go back to studying physical phenomena and their concrete applications in devices that can also advance other research areas (such as astrophysics, which is my original field). I thank Prof. Passaro for proposing such a fascinating project and for creating stimulating and productive moments of discussion and in-depth analysis. I also thank Prof. Francesco De Leonardis, co-supervisor of this thesis, for always being available, from the very beginning, and for patiently and calmly explaining to me the basic concepts of integrated photonics. A special thank-you goes to Dr. Martino De Carlo, a brilliant researcher who, day by day, helped me along this path with clarity, simplicity, and enthusiasm.

I would also like to express my heartfelt thanks to Prof. Goran Mashanovich of the University of Southampton and to his research group for welcoming me during my research stay abroad. I found a dynamic, productive, and stimulating environment, and at the same time one that was truly welcoming on a human level.

I would like to thank Prof. Mario Carpentieri, coordinator of the Doctoral Research Program in Electrical and Information Engineering (DRIEI), for his support and prompt availability throughout this research experience.

I wish to thank Prof. Andrea Melloni and Prof. Richard Soref for agreeing to review my thesis; I thank them in advance for any suggestions they may wish to offer to improve it.

Finally, I am grateful for the financial support under Italian Ministerial Decree no. 351/2022, investment area National Recovery and Resilience Plan (PNRR), Mission 4.

List of publications

During the PhD research period, the following publications have been published:

- Coppola, C. M., De Carlo, M., De Leonardis, F., Passaro, V. M. N. “i-PHAOS: An Overview with an Open-Source Collaborative Database on Miniaturized Integrated Spectrometers.”. Sensors (Basel), 2024, 24(20):6715. doi: 10.3390/s24206715;
- Coppola, C. M., De Carlo, M., De Leonardis, F. and Passaro, V. M. N. “A new integrated optical spectrometer based on a Vernier-like configuration”. 25th Anniversary International Conference on Transparent Optical Networks (ICTON), Barcelona, Spain, 2025, pp. 1-4, doi: 10.1109/ICTON67126.2025.11125160;
- Coppola, C. M., De Carlo, M., De Leonardis, F. and Passaro, V. M. N. “High-Resolution On-Chip Digitally Tunable Spectrometer Based on Double-Cascaded Ring Resonators”. Adv. Photonics Res., 2025, 6: 2500021. https://doi.org/10.1002/adpr.202500021

Based on the results shown in Chapter 4, a paper is in preparation.

Appendix A

Appendices

A.1 Fourier transform spectrometer: derivation of the basic equations.

We derive here the relationship between the interferogram $I(p)$ and the spectral intensity (or spectral power distribution) of the light source, $I(\bar{\nu})$. The first is a function of the optical path difference p between the paths of the two arms of the interferometer. It is the output of a Fourier-transform spectrometer. The second is given as a function of the wavenumber $\bar{\nu}$, otherwise referred to as spatial frequency. In fact, it is the inverse of the wavelength:

$$\bar{\nu} = \frac{1}{\lambda}[\mathrm{cm}^{-1}]$$

The interferogram can be expressed as the sum of a constant term and the cosine transform fo the spectral intensity distribution $I(\bar{\nu})$:

$$\begin{aligned}
I(p) &= \int_0^{\infty} I(p,\bar{\nu}) \cdot \bar{\nu} = \int_0^{\infty} I(\bar{\nu}) \cdot [1 + \cos(2\pi\bar{\nu}p)] d\bar{\nu} = \\
&= \int_0^{\infty} I(\bar{\nu}) \cdot \bar{\nu} + \int_0^{\infty} I(\bar{\nu}) \cdot \cos(2\pi\bar{\nu}p) \cdot d\bar{\nu} = \\
&= \int_0^{\infty} I(\bar{\nu}) \cdot \cos(2\pi\bar{\nu} \cdot 0) d\bar{\nu} + \int_0^{\infty} I(\bar{\nu}) \cdot \cos(2\pi\bar{\nu}p) \cdot d\bar{\nu} = \\
&= \frac{1}{2}\int_{-\infty}^{+\infty} I(\bar{\nu}) \cdot \cos(2\pi\bar{\nu} \cdot 0) d\bar{\nu} + \frac{1}{2}\int_{-\infty}^{+\infty} I(\bar{\nu}) \cdot \cos(2\pi\bar{\nu}p) \cdot d\bar{\nu} = \\
&= \frac{1}{2} I(p=0) + \frac{1}{2}\int_{-\infty}^{+\infty} I(\bar{\nu}) \cdot \cos(2\pi\bar{\nu}p) \cdot d\bar{\nu} \qquad \text{(A.1)}
\end{aligned}$$

This equation describes how the detected output signal in a Fourier transform spectrometer (the interferogram) arises from the interference of all spectral components of the input spectrum.

The second term in the last equation represents a cosine Fourier transform; Eq. A.1 can be re-written as:

$$\int_{-\infty}^{+\infty} I(\bar{\nu}) \cdot \cos(2\pi\bar{\nu}p) \cdot d\bar{\nu} = 2\left[I(p) - \frac{1}{2} \cdot I(p=0)\right] \qquad \text{(A.2)}$$

This relation represents the connection between the interferogram and the spectral intensity; in particular, the cosine transform of the spectrum yields twice the difference of the interferogram from its zero-path value. It represents the mathematical Fourier reciprocity between the spatial domain (described by the optical path difference p in the interferogram) and the spectral domain (expressed in wavenumber $\bar{\nu}$ in the spectral intensity). p and $\bar{\nu}$ are hence Fourier-conjugate variables, since the interferogram $I(p)$ and the spectral intensity $I(\bar{\nu})$ form a Fourier-transform pair.

It is now possible to recover the spectral intensity $I(\bar{\nu})$ as:

$$\begin{aligned} I(\bar{\nu}) &= \int_{-\infty}^{+\infty} 2\left[I(p) - \frac{1}{2}\cdot I(p=0)\right]\cdot\cos(2\pi\bar{\nu}p)\cdot\bar{\nu} = \\ &= 2\int_{0}^{+\infty} 2\left[I(p) - \frac{1}{2}\cdot I(p=0)\right]\cdot\cos(2\pi\bar{\nu})\cdot d\bar{\nu} = \\ &= 4\int_{0}^{\infty}\left[I(p) - \frac{1}{2}\cdot I(p=0)\right]\cdot\cos(2\pi\bar{\nu}p)\cdot d\bar{\nu} \end{aligned}$$

A.2 Compressing algorithms: math behind them

In reconstructive spectrometers, compressed sensing is implemented; this technique aims in reconstructing a signal via a limited number of measurements. The basic assumption behind compressed sensing is that the target signal has a sparse representation in a certain domain (for example, in its Fourier components or wavelet decomposition). In this perspective, the signal can be efficiently represented by combining few elements with non-null amplitude from an appropriate basis set in a transformed domain.

Reconstructive algorithms are implemented in order to retrieve the spectrum starting from a certain number of compressed measurements. [48], [56], [58]. The measurement column vector y (M components) can be written as:

$$y = Sx \tag{A.3}$$

with S representing the matrix containing the sensing responses of the physical optical structures adopted in the spectrometer while x is a column vector (N components) that represents the spectrum of the light source. Typically $M < N$, hence the linear system is underdetermined; eventually, it is necessary to move towards a transformed domain through a transformation matrix T, so that x can be represented as:

$$x = Ta \tag{A.4}$$

with a transformed vector with few non-zero components in the transformation domain. The linear system in such a domain can then be re-written as:

$$y = STa \tag{A.5}$$

It has been proven by [56] that, for underdetermined systems, it is possible to retrieve the solution with the higher sparsity by finding the solution of the system under the condition of minimal norm l_1 $|a|_{l_1}$. In other words, the complete dataset y can be retrieved once the solution of Eq.A.5 under the condition of minimizing $|a|_{l_1} = \sum_{r=1}^{n}$ is found. An additional condition to fullfill concerns the matrix S: measurements stored in S should be uncorrelated and random with respect to the transformation basis in order to have an incoherent sampling.

In integrated spectroscopy an alternative approach is suggested in order to overcome the problem of under-determined system and to reconstruct the signal; indeed, instead of implementing compressive algorithms in order to reconstruct the signal, the usage of filter arrays allows for a very fast method to reconstruct the signal. The additional benefits of having filter arrays rely on their physical properties of being deterministic objects that need to be calibrated once.

A.3 Experimental procedures for calibration and measurements

Although apparently trivial, it is worth describing the procedure that has been adopted in order to calibrate the measuring instrumentation. In fact, it depends on the available tools and best experimental practices that the operator decides to adopt. Experience is essential to develop proficiency in calibration.

The experimental setup that has been used is the so-called 1550 nm setup (setup 1) of Lab 2077 in University of Southampton, II floor. The setup consists of:

- laser module (8163B Light wave multimeter) by Agilent, consisting of a tunable laser (81940A, input channel, channel 1) and a power sensor (8163B, output channel, channel 2);
- input and output optic fibers (Thorlabs, type SMF-28 Ultra 1260 nm -1625 nm 213084N and SMF-28e+ 1260 nm-1620 nm 191257A);
- chip holder (Newport);
- goniometers for both input and output optic fibers;
- optic fibers holders (Thorlabs)
- polarizer (Thorlabs, FPC562)
- GXCAM (BFL - Back Focal Length 11.6 mm-36 mm) microscope and camera
- camera holder (Newport)

The goniometers are used to measure the angle with which the optic fibers reach the PICs. The usage of an inclinometer allows to measure the angle; in the setup used to perform the measurements, the optic fibers holders are such that the angle at which the optic fibers reach the PIC's plane can be computed as 30° minus the value read on the inclinometer. As a convention, the angles reported in the rest of the discussion will be the ones read on the inclinometer, unless otherwise stated. In principle, the choice of the angle allows to shift the peak of the expected bell-shaped function for a fibre-grating coupler's output to the maximum wavelength at which the waveguides have been designed. Eventually, the first step in the calibration procedure consists in deciding the angles for the optic fibres; this is performed by using the normalization waveguides and tuning the angles in order to have the output bell-shaped power curves centered at the expected wavelengths. Considering that the chip has been fabricated in SOI technology and that the measurements are performed at 1550 nm, an expected angle of 20° (read on the inclinometer, 10° respect to the normal) should be expected in order to have the bell-shaped curve centered around 1550 nm. On fabricated chips it is usual practice to insert devices (e.g. normalization waveguides), that do not belong to the photonic circuit itself but they are provided as testing units useful as zeroing references.

The output power is checked and "eyeballed" while moving the fibre holders in order to reach a reasonably high (i.e. few hundreds mmW) value. Once fixed the angles, the measurements can be performed. In the power measuring unit, it is possible to work in "Local" mode, where it is possible to select "Manual" and "Auto". When Local/Manual is activated, it is possible to edit details for the channels. In our setup, Channel 1 and Channel 2 represent the input and output powers, respectively. When editing Channel 1's details, the wavelength is set to 1550 nm; this is achieved by using the arrows buttons available on the device interface. The power is automatically set to 6 dBm and it is left as such. After introducing this changes, the button "OK" can be pressed in order to approve them. By pressing "Overview" and scrolling to Channel 2, the output channel's features can be edited. Specifically, "AvTime" can be selected and set to 200 μs; once again, pressing "Ok" commits the changes. By selecting "Change mode", editing it into "Auto" and pressing "OK" the changes are saved and it is possible to proceed with the measurements. By pressing "Overview" it is possible to go to the description of the general information of channels 1 and 2.

An additional step in the calibration process concerns the change in the polarization of the input light, achieved by means of polarizers (see Fig. A.1).

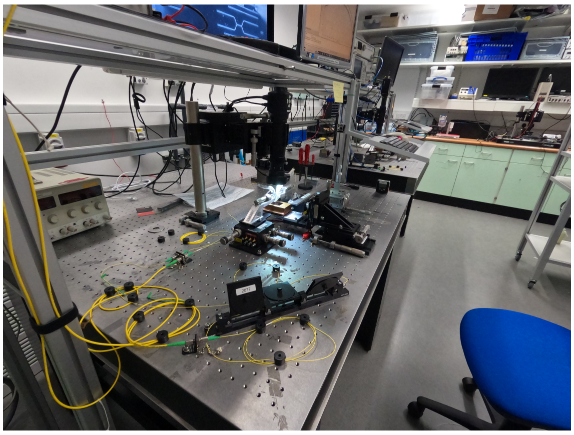

Figure A.1: Polarizer in the setup 1550 nm in the University of Southampton.

Input and output powers are detected shown on the screen of a computer by means of the Software PAS Photonic Application Suites, Insertion Loss (IL Engine Client); it is reached via PAS Launch Pad.

Changes in the polarization can change the maximum of the curve because the response of the grating coupler is polarization dependent. In fact, grating couplers are designed to maximize the output for TE polarized light. Polarizers are used and the output power is considered acceptable if the ripples in the curves are less than 1 dB.

10 dB expected setup losses (if not more) max 13 dB (that would mean to half the initial power because it would be 13-10 = 3dB)

For SL3 the maximum obtained before the oxide deposit was 30 dB; in these updated tests, the maximum that can be achieved is around 33 dB, that means a difference of around 3 dB, assuming that the losses between the two setups are the same. In fact, when the first set of tests have been performed with this setup, the calibration procedures (optic fibres and chip cleaning etc) have been optimized in order to have around 10 dB losses on a reference PIC (that is a very good value for a setup).

When pressing “run single” the value of the power is usually halved because it is the value of the power at the wavelength at which the sweep in lambda starts (that is usually 3 dB lower than the maximum, or more)

Comments on the detector’s range: if measurements are taken out of range, they will have lots of “noise”. To avoid this, one can explicitly set the initial powermeter to 0 dBm and perform dynamic range scan by fixing the number of scans (e.g. dynamic scan range = 2) to be performed and the value of the decrement (e.g. decrement [dB] = 30).

A.4 Practical adopted procedure

As a reference on the practices that have been adopted, a list of the steps that have been followed is here reported

- place the chip and the optic fibers close by, being careful not to break the optic fibers;
- place the optic fibers as input and output of the system (waveguide, grating couplers etc) to be measured;
- once the x and y coordinates of the optic fibers are close to the input and output, lower the optical fiber holders down along z; this operation should be carefully performed not to scratch the chip and to break the optic fibers. As an operational suggestion, one knob of the optical fiber holder should be quickly moved in opposite direction while lowering the z coordinate. As soon as the fiber touches the chip one stops and eventually raise the fiber a little bit from the chip xy plane;
- check that the optic fiber does not touch the chip while scanning along light propagation of the structure to perform the measurements on;

- scan along the structure in order to find the maximum transmitted output power; this step is performed both on for the input and output optic fibers;
- once the maximum is found, it is possible to fine tune by lowering the optic fibers along z to get even closer to the structure to be measured;
- if there are large LINES going downwards or upwards, perform additional measurements changing the initial powermeter range; it is by default put to 0 dBm but if there are measured values that are small, this value should be reduced to -10 dBm or less, otherwise it would be increased (max value that can be set is 10 dBm).
- in case the measured curve shows lots of wiggling, it is possible to reduce them by changing the polarization of the light; this is achieved by moving the three pads of the polarizer.

Bibliography

[1] J Kulakowski and B d'Humières, "Chip-size spectrometers drive spectroscopy towards consumer and medical applications," in *Proc. SPIE 11693, Photonic Instrumentation Engineering VIII*, 2021, 116931A. DOI: `10.1117/12.2591048`.

[2] R. Wolffenbuttel, "State-of-the-art in integrated optical microspectrometers," *IEEE Trans. Instrum. Meas.*, vol. 53, no. 1, pp. 197–202, 2004. DOI: `10.1109/TIM.2004.831484`.

[3] D. Goldman, P. White, and N. Anheier, "Miniaturized spectrometer employing planar waveguides and grating couplers for chemical analysis," *Appl. Opt.*, vol. 29, no. 31, pp. 4583–4589, 1990. DOI: `10.1364/AO.29.004583`.

[4] Z Yang, T Albrow-Owen, W Cai, and T Hasan, "Miniaturization of optical spectrometers," *Science*, vol. 371, eabe0722, 2021. DOI: `10.1126/science.abe0722`.

[5] A Li, C Yao, J Xia, *et al.*, "Advances in cost-effective integrated spectrometers," *Light Sci. Appl.*, vol. 11, p. 174, 2022. DOI: `10.1038/s41377-022-00844-w`.

[6] Y Qiu, X Zhou, X Tang, Q Hao, and M Chen, "Micro spectrometers based on materials nanoarchitectonics," *Materials*, vol. 16, no. 6, p. 2253, 2023. DOI: `10.3390/ma16062253`.

[7] J Wang, B Zheng, and X Wang, "Strategies for high performance and scalable on-chip spectrometers," *J. Phys.: Photonics*, vol. 3, no. 1, p. 012 006, 2020. DOI: `10.1088/2515-7647/ab916a`.

[8] R. Jones, "Phenomenological description of the response and detecting ability of radiation detectors," *Proc. IRE*, vol. 47, no. 9, pp. 1495–1502, 1959. DOI: `10.1109/JRPROC.1959.287047`.

[9] J Liu, *Photonic Devices.* Cambridge University Press, 2005. DOI: `10.1017/CBO9780511614255`.

[10] M Czerny and A. Turner, ""Uber den astigmatismus bei spiegelspektrometern," *Zeitschrift f"ur Physik*, vol. 61, no. 11-12, pp. 792–797, 1930. DOI: `10.1007/BF01397321`.

[11] H. Ebert, "Zwei formen von spectrographen," *Annalen der Physik*, vol. 274, pp. 489–493, 1889. DOI: `10.1002/andp.18892741113`.

[12] W. Fastie, "A small plane grating monochromator," *J. Opt. Soc. Am.*, vol. 42, pp. 641–647, 1952. DOI: `10.1364/JOSA.42.000641`.

[13] H. Rowland, "On concave gratings for optical purposes," *Philosophical Magazine Series 5*, vol. 16, pp. 197–210, 1883.

[14] T. Namioka, "Diffraction gratings," in *Vacuum Ultraviolet Spectroscopy.* Academic Press, 2000, pp. 347–377. DOI: `10.1016/B978-012617560-8/50018-9`.

[15] K. Otsuka and K. Imai, "Fabrication of silicon reflection-type arrayed-waveguide gratings with distributed bragg reflectors," *Opt. Lett.*, vol. 38, pp. 3530–3533, 2013. DOI: `10.1364/OL.38.003530`.

[16] S. Pathak, P. Dumon, D. Van Thourhout, and W. Bogaerts, "Comparison of awgs and echelle gratings for wavelength division multiplexing on silicon-on-insulator," *IEEE Photonics Journal*, vol. 6, no. 5, pp. 1–9, 2014. DOI: `10.1109/JPHOT.2014.2362698`.

[17] J. Carmo, R. Rocha, M. Bartek, G. de Graaf, R. Wolffenbuttel, and J. Correia, "A review of visible-range fabry-perot microspectrometers in silicon for the industry," *Optics & Laser Technology*, vol. 44, no. 7, pp. 2312–2320, 2012. DOI: `10.1016/j.optlastec.2012.01.026`.

[18] A. Emadi, H. Wu, G. de Graaf, and R. Wolffenbuttel, "Design and implementation of a sub-nm resolution microspectrometer based on a linear-variable optical filter," *Opt. Express*, vol. 20, pp. 489–507, 2012. DOI: `10.1364/OE.20.000489`.

[19] A. Liapis, B. Gao, M. Siddiqui, Z. Shi, and R. Boyd, "On-chip spectroscopy with thermally tuned high-q photonic crystal cavities," *Appl. Phys. Lett.*, vol. 108, p. 021 105, 2016. DOI: `10.1063/1.4939986`.

[20] N. Sharma, G. Kumar, V. Rakesh, G. Mote, and S. Gupta, "Reconstructive spectrometer using a photonic crystal cavity," *Opt. Express*, vol. 29, pp. 26 645–26 657, 2021. DOI: `10.1364/OE.435672`.

[21] S. Zheng, H. Cai, Y. Gu, L. Chin, and A. Liu, "High-resolution on-chip spectrometer with a tunable micro-ring resonator filter," in *Conference on Lasers and Electro-Optics, OSA Technical Digest (online)*, Optica Publishing Group, 2016. DOI: `10.1364/CLEO_AT.2016.AM1J.2`.

[22] S. Zheng, H. Cai, J. Song, *et al.*, "A single-chip integrated spectrometer via tunable microring resonator array," *IEEE Photonics Journal*, vol. 11, no. 5, 2019. DOI: `10.1109/JPHOT.2019.2939580`.

[23] X. Chen, X. Gan, Y. Zhu, and J. Zhang, "On-chip micro-ring resonator array spectrum detection system based on convex optimization algorithm," *Nanophotonics*, vol. 12, no. 4, pp. 715–724, 2023.

[24] H. Zhu, S. Zheng, J. Zou, H. Cai, Z. Li, and A. Liu, "A high-resolution integrated spectrometer based on cascaded a ring resonator and an awg," in *Conference on Lasers and Electro-Optics, OSA Technical Digest (online)*, Optica Publishing Group, 2020. DOI: `10.1364/CLEO_AT.2020.JTu2G.32`.

[25] Z. Zhang, Y. Wang, J. Wang, *et al.*, "Integrated scanning spectrometer with a tunable micro-ring resonator and an arrayed waveguide grating," *Photonics Research*, vol. 10, A74–A81, 2022.

[26] Y. Horie, A. Arbabi, S. Han, and A. Faraon, "High resolution on-chip optical filter array based on double subwavelength grating reflectors," *Optics Express*, vol. 23, pp. 29 848–29 854, 2015.

[27] N. Alshamrani, A. Grieco, B. Hong, and Y. Fainman, "Miniaturized integrated spectrometer using a silicon ring-grating design," *Optics Express*, vol. 29, pp. 15 279–15 287, 2021. DOI: `10.1364/OE.424443`.

[28] W. Bogaerts, S. Pathak, A. Ruocco, and S. Dwivedi, "Silicon photonics non-resonant wavelength filters: Comparison between awgs, echelle gratings, and cascaded mach-zehnder filters," in *Proc. SPIE 9365, Integrated Optics: Devices, Materials, and Technologies XIX*, 2015. DOI: `10.1117/12.2082785`.

[29] J. Bates, "Fourier transform spectroscopy," *Computers & Mathematics with Applications*, vol. 4, pp. 73–84, 1978. DOI: `10.1016/0898-1221(78)90020-2`.

[30] P. Fellgett, "Theory of infrared sensitivities and its application to investigations of stellar radiation in the near infrared," Ph.D. dissertation, Cambridge University, UK, 1951.

[31] J. Connes and P. Connes, "Near-infrared planetary spectra by fourier spectroscopy. i. instruments and results," *J. Opt. Soc. Am.*, vol. 56, pp. 896–910, 1966. DOI: `10.1364/JOSA.56.000896`.

[32] L. Zhang, J. Chen, C. Ma, W. Li, Z. Qi, and N. Xue, "Research progress on on-chip fourier transform spectrometer," *Laser & Photonics Reviews*, vol. 15, p. 2 100 016, 2021.

[33] E. le Coarer, S. Blaize, P. Benech, *et al.*, "Wavelength-scale stationary-wave integrated fourier-transform spectrometry," *Nature Photon*, vol. 1, pp. 473–478, 2007.

[34] E. le Coarer, L. Venancio, P. Kern, *et al.*, "Swifts: On-chip very high spectral resolution spectrometer," in *Proc. SPIE 10565, International Conference on Space Optics - ICSO 2010*, 2010. DOI: `10.1117/12.2309259`.

[35] P. Cavalier, J. Villègier, P. Feautrier, C. Constancias, and A. Morand, "Light interference detection on-chip by integrated snspd counters," *AIP Advances*, vol. 1, no. 4, 2011.

[36] D. Pohl, M. Reig Escalè, M. Madi, *et al.*, "An integrated broadband spectrometer on thin-film lithium niobate," *Nature Photonics*, vol. 14, no. 1, pp. 24–29, 2019.

[37] E. Heidari, X. Xu, C. Chung, and R. Chen, "On-chip fourier transform spectrometer on silicon-on-sapphire," *Optics Letters*, vol. 44, pp. 2883–2886, 2019.

[38] S. Zheng, J. Zou, H. Cai, *et al.*, "Microring resonator-assisted fourier transform spectrometer with enhanced resolution and large bandwidth in single chip solution," *Nature Communications*, vol. 10, p. 2349, 2019.

[39] H. Xu, Y. Qin, G. Hu, and H. K. Tsang, "Scalable integrated two-dimensional fourier-transform spectrometry," *Nature Communications*, vol. 15, no. 1, p. 436, 2024, ISSN: 2041-1723. DOI: `10.1038/s41467-023-44518-y`. [Online]. Available: `https://doi.org/10.1038/s41467-023-44518-y`.

[40] A. Li, Y. Wu, C. Wang, F. Bao, Z. Yang, and S. Pan, "An inversely designed integrated spectrometer with reconfigurable performance and ultra-low power consumption," *Opto-Electronic Advances*, vol. 7, no. 8, p. 240 099, 2024, ISSN: 2096-4579. DOI: `10.29026/oea.2024.240099`. [Online]. Available: `https://www.oejournal.org/article/id/6697890a99d8810470c29dee`.

[41] M. Yu, Y. Okawachi, A. G. Griffith, N. Picqué, M. Lipson, and A. L. Gaeta, "Silicon-chip-based mid-infrared dual-comb spectroscopy," *Nature Communications*, vol. 9, no. 1, p. 1869, 2018. DOI: `10.1038/s41467-018-04350-1`.

[42] C. Bao, Z. Yuan, L. Wu, *et al.*, "Architecture for microcomb-based ghz-mid-infrared dual-comb spectroscopy," *Nature Communications*, vol. 12, no. 1, p. 6573, 2021. DOI: `10.1038/s41467-021-26958-6`.

[43] A. Dutt, C. Joshi, X. Ji, *et al.*, "On-chip dual-comb source for spectroscopy," *Science Advances*, vol. 4, no. 3, e1701858, 2018. DOI: `10.1126/sciadv.1701858`.

[44] Z. Wang and Z. Yu, "Spectral analysis based on compressive sensing in nanophotonic structures," *Opt. Express*, vol. 22, pp. 25 608–25 614, 2014.

[45] H. Cao, "Perspective on speckle spectrometers," *Journal of Optics*, vol. 19, no. 6, p. 060 402, 2017.

[46] Y. Wan, X. Fan, and Z. He, "Review on speckle-based spectrum analyzer," *Photonic Sensors*, vol. 11, no. 2, pp. 187–202, 2021.

[47] H. Cao and Y. Eliezer, "Harnessing disorder for photonic device applications," *Applied Physics Reviews*, vol. 9, no. 1, p. 011 309, 2022.

[48] A. Boschetti, L. Pattelli, R. Torre, and D. Wiersma, "Perspectives and recent advances in super-resolution spectroscopy: Stochastic and disordered-based approaches," *Applied Physics Letters*, vol. 120, no. 25, p. 250 502, 2022.

[49] J. Bao and M. Bawendi, "A colloidal quantum dot spectrometer," *Nature*, vol. 523, pp. 67–70, 2015.

[50] Z. Wang, S. Yi, A. Chen, *et al.*, "Single-shot on-chip spectral sensors based on photonic crystal slabs," *Nature Communications*, vol. 10, p. 1020, 2019.

[51] Q. Liu, Z. Xuan, Z. Wang, *et al.*, "Low-cost micro-spectrometer based on a nano-imprint and spectral-feature reconstruction algorithm," *Optics Letters*, vol. 47, pp. 2923–2926, 2022.

[52] C. Sun, Z. Chen, Y. Ye, *et al.*, "Integrated microring spectrometer with in-hardware compressed sensing to break the resolution-bandwidth limit for general continuous spectrum analysis," *Laser Photonics Rev*, p. 2 300 291, 2023.

[53] S. Kabanikhin, "Definitions and examples of inverse and ill-posed problems," *Journal of Inverse and Ill-posed Problems*, vol. 16, no. 4, pp. 317–357, 2008.

[54] D. Brady, M. Gehm, N. Pitsianis, and X. Sun, "Compressive sampling strategies for integrated microspectrometers," in *SPIE Proceedings*, 2016. DOI: `10.1117/12.666124`.

[55] J. Zhao, M. Lakatos-Tóth, M. Westerham, Z. Zhang, A. Moskoff, and F. Ren, "Openics: Open image compressive sensing toolbox and benchmark," *Software Impacts*, vol. 9, p. 100 081, 2021.

[56] E. Candès and J. Romberg, "Sparsity and incoherence in compressive sampling," *Inverse Problems*, vol. 23, p. 969, 2007.

[57] A. Mondal and K. Debnath, "Design of resolution-tunable neural network-based integrated reconstructive spectrometer," *Sensors Journal*, vol. 22, no. 3, pp. 2630–2636, 2022.

[58] B. Redding and H. Cao, "Using a multimode fiber as a high-resolution, low-loss spectrometer," *Optics Letters*, vol. 37, pp. 3384–3386, 2012.

[59] J. Meng, J. Cadusch, and K. Crozier, "Detector-only spectrometer based on structurally colored silicon nanowires and a reconstruction algorithm," *Nano Letters*, vol. 20, no. 1, pp. 320–328, 2019.

[60] Z. Yang, T. Albrow-Owen, H. Cui, *et al.*, "Single-nanowire spectrometers," *Science*, vol. 365, no. 6457, pp. 1017–1020, 2019.

[61] S. Yuan, D. Naveh, K. Watanabe, *et al.*, "A wavelength-scale black phosphorus spectrometer," *Nature Photonics*, vol. 15, pp. 601–607, 2021.

[62] L. Guo, H. Sun, M. Wang, *et al.*, "A single-dot perovskite spectrometer," *Advanced Materials*, vol. 34, no. 33, 2022.

[63] L. Kong, Q. Zhao, H. Wang, *et al.*, "Single-detector spectrometer using a superconducting nanowire," *Nano Letters*, vol. 21, no. 22, pp. 9625–9632, 2021.

[64] H. Yoon, H. Fernandez, F. Nigmatulin, W. Cai, Z. Yang, *et al.*, "Miniaturized spectrometers with a tunable van der waals junction," *Science*, vol. 378, pp. 296–299, 2022.

[65] D. Deng, Z. Zheng, J. Li, R. Zhou, *et al.*, "Electrically tunable two-dimensional heterojunctions for miniaturized near-infrared spectrometers," *Nature Communications*, vol. 13, p. 4627, 2022.

[66] J. Oliver, W. Lee, S. Park, and H. Lee, "Improving resolution of miniature spectrometers by exploiting sparse nature of signals," *Optics Express*, vol. 20, pp. 2613–2625, 2012.

[67] J. Oliver, W. Lee, and H. Lee, "Filters with random transmittance for improving resolution in filter-array-based spectrometers," *Optics Express*, vol. 21, pp. 3969–3989, 2013.

[68] Y. Zhang, X. Guo, T. Albrow-Owen, Z. Zhao, *et al.*, "Miniaturized computational photonic molecule spectrometer," *arXiv preprint arXiv:2308.07764*, 2023.

[69] H. Xu, Y. Qin, G. Hu, *et al.*, "Breaking the resolution-bandwidth limit of chip-scale spectrometry by harnessing a dispersion-engineered photonic molecule," *Light Science & Applications*, vol. 12, p. 64, 2023.

[70] C. Yao, M. Chen, T. Yan, *et al.*, "Broadband picometer-scale resolution on-chip spectrometer with reconfigurable photonics," *Light Science & Applications*, vol. 12, p. 156, 2023.

[71] C. Yao, K. Xu, W. Zhang, *et al.*, "Integrated reconstructive spectrometer with programmable photonic circuits," *Nature Communications*, vol. 14, p. 6376, 2023.

[72] Y. Kwak, S. Park, Z. Ku, *et al.*, "A pearl spectrometer," *Nano Letters*, vol. 21, no. 2, pp. 921–930, 2020.

[73] Q. Guan, Z. Lim, H. Sun, *et al.*, "Review of miniaturized computational spectrometers," *Sensors*, vol. 23, no. 21, p. 8768, 2023.

[74] O. Katsunari and I. Kenzo, "Fabrication of silicon reflection-type arrayed-waveguide gratings with distributed bragg reflectors," *Optics Letters*, vol. 38, pp. 3530–3533, 2013.

[75] A. Li and Y. Fainman, "Integrated silicon fourier transform spectrometer with broad bandwidth and ultra-high resolution," *Laser & Photonics Reviews*, vol. 15, p. 2 000 358, 2021.

[76] A. Li, J. Davis, A. Grieco, N. Alshamrani, and Y. Fainman, "Fabrication-tolerant fourier transform spectrometer on silicon with broad bandwidth and high resolution," *Photonics Research*, vol. 8, p. 219, 2020.

[77] M. Souza, A. Grieco, N. Frateschi, *et al.*, "Fourier transform spectrometer on silicon with thermo-optic non-linearity and dispersion correction," *Nature Communications*, vol. 9, p. 665, 2018.

[78] A. Li and Y. Fainman, "On-chip spectrometers using stratified waveguide filters," *Nature Communications*, vol. 12, p. 2704, 2021.

[79] G. Micó, B. Gargallo, D. Pastor, and P. Muñoz, "Integrated optic sensing spectrometer: Concept and design," *Sensors*, vol. 19, no. 5, 2019.

[80] R. Soref, F. De Leonardis, V. Passaro, and Y. Fainman, "On-chip digital fourier-transform spectrometer using a thermo-optical michelson grating interferometer," *Journal of Lightwave Technology*, vol. 36, no. 22, pp. 5160–5167, 2018.

[81] M. Smit, X. Leijtens, H. Ambrosius, E. Bente, J. van der Tol, *et al.*, "An introduction to inp-based generic integration technology," *Semiconductor Science and Technology*, vol. 29, p. 083 001, 2014.

[82] R. Cheng, C. Zou, X. Guo, *et al.*, "Broadband on-chip single-photon spectrometer," *Nature Communications*, vol. 10, p. 4104, 2019.

[83] A. Rahim *et al.*, "Expanding the silicon photonics portfolio with silicon nitride photonic integrated circuits," *Journal of Lightwave Technology*, vol. 35, no. 4, pp. 639–649, 2017.

[84] H. Ghorbani, R. Tewari, M. Rad, E. Bernier, and T. Hall, "Design and simulation of a si3n4 sub-ghz resolution integrated micro-spectrometer," in *2019 International Conference on Numerical Simulation of Optoelectronic Devices (NUSOD)*, 2019. DOI: `10.1109/NUSOD.2019.8806837`.

[85] M. Hasan, G. Hasan, H. Ghorbani, *et al.*, "Broadband high-resolution integrated spectrometer architecture & data processing method (version 1)," *arXiv*, 2023. DOI: `10.48550/arXiv.2301.06653`.

[86] X. Nie, E. Ryckeboer, G. Roelkens, and R. Baets, "Cmos-compatible broadband co-propagative stationary fourier transform spectrometer integrated on a silicon nitride photonics platform," *Optics Express*, vol. 25, A409–A418, 2017.

[87] A. Subramanian, E. Ryckeboer, A. Dhakal, *et al.*, "Silicon and silicon nitride photonic circuits for spectroscopic sensing on-a-chip," *Photonics Research*, vol. 3, B47–B59, 2015.

[88] P. Kaur, A. Boes, G. Ren, T. Nguyen, G. Roelkens, and A. Mitchell, "Hybrid and heterogeneous photonic integration," *APL Photonics*, vol. 6, no. 6, p. 061 102, 2021.

[89] R. Wang, A. Vasiliev, M. Muneeb, *et al.*, "Iii-v-on-silicon photonic integrated circuits for spectroscopic sensing in the 2-4 μm wavelength range," *Sensors (Basel)*, vol. 17, no. 8, p. 1788, 2017.

[90] M. Muneeb, A. Vasiliev, A. Ruocco, *et al.*, "Iii-v-on-silicon integrated micro-spectrometer for the 3 μm wavelength range," *Optics Express*, vol. 24, no. 9, p. 9465, 2016.

[91] G. Roelkens, U. Dave, A. Gassenq, *et al.*, "Mid-ir heterogeneous silicon photonics," in *SPIE Proceedings*, 2013. DOI: `10.1117/12.2041226`.

[92] J. Mohr, B. Anderer, and W. Ehrfeld, "Fabrication of a planar grating spectrograph by deep-etch lithography with synchrotron radiation," *Sensors and Actuators A*, vol. 25, pp. 571–575, 1991.

[93] A. Armin, R. Jansen-van Vuuren, N. Kopidakis, P. Burn, and P. Meredith, "Narrowband light detection via internal quantum efficiency manipulation of organic photodiodes," *Nature Communications*, vol. 6, p. 6343, 2015.

[94] S. Xing, V. Nikolis, J. Kublitski, *et al.*, "Miniaturized vis-nir spectrometers based on narrowband and tunable transmission cavity organic photodetectors with ultrahigh specific detectivity above 1014 jones," *Advanced Materials*, vol. 33, p. 2 102 967, 2021.

[95] Y. Wang, J. Kublitski, S. Xing, *et al.*, "Narrowband organic photodetectors–towards miniaturized, spectroscopic sensing," *Materials Horizons*, vol. 9, pp. 220–251, 2022.

[96] T. Li, G. Hu, L. Tao, *et al.*, "Sensitive photodetection below silicon bandgap using quinoid-capped organic semiconductors," *Science Advances*, vol. 9, eadf6152, 2023.

[97] K. Fan, R. Averitt, and W. Padilla, "Active and tunable nanophotonic metamaterials," *Nanophotonics*, vol. 11, no. 17, pp. 3769–3803, 2022.

[98] Y. Li, X. Jiang, Y. Chen, *et al.*, "A platform for integrated spectrometers based on solution-processable semiconductors," *Light Science & Applications*, vol. 12, p. 184, 2023.

[99] S. Khan, A. Khan, J. Azadmanjiri, *et al.*, "2d heterostructures for highly efficient photodetectors: From advanced synthesis to characterizations, mechanisms, and device applications," *Advanced Photonics Research*, vol. 3, p. 2 100 342, 2022.

[100] A. Chaves, J. Azadani, H. Alsalman, *et al.*, "Bandgap engineering of two-dimensional semiconductor materials," *npj 2D Materials and Applications*, vol. 4, p. 29, 2020.

[101] H. Shabbir and M. Wojnicki, "Recent progress of non-cadmium and organic quantum dots for optoelectronic applications with a focus on photodetector devices," *Electronics*, vol. 12, no. 6, p. 1327, 2023.

[102] H. Liu, M Gao, J McCaffrey, Z. Wasilewski, and S Fafard, “Quantum dot infrared photodetectors,” *Applied Physics Letters*, vol. 78, no. 1, pp. 79–81, 2001.

[103] S Keuleyan, E Lhuillier, V Brajuskovic, and P Guyot-Sionnest, “Mid-infrared hgte colloidal quantum dot photodetectors,” *Nature Photonics*, vol. 5, pp. 489–493, 2011.

[104] M. Grotevent, S Yakunin, D Bachmann, *et al.*, “Integrated photodetectors for compact fourier-transform waveguide spectrometers,” *Nature Photonics*, vol. 17, pp. 59–64, 2023.

[105] H. Li, L. Bian, K Gu, *et al.*, “A near-infrared miniature quantum dot spectrometer,” *Advanced Optical Materials*, vol. 9, p. 2 100 376, 2021.

[106] C Wen, X Zhao, G Mu, M Chen, and X Tang, “Simulation and design of hgse colloidal quantum-dot microspectrometers,” *Coatings*, vol. 12, no. 7, p. 888, 2022.

[107] V. Shrestha, B Craig, J Meng, *et al.*, “Mid- to long-wave infrared computational spectroscopy with a graphene metasurface modulator,” *Scientific Reports*, vol. 10, p. 5377, 2020.

[108] P. Pham, T. Mai, H. Do, V. Ponnusamy, and F. Chuang, “Integrated graphene heterostructures in optical sensing,” *Micromachines*, vol. 14, no. 5, p. 1060, 2023.

[109] G. Bhimanapati, Z Lin, V Meunier, *et al.*, “Recent advances in two-dimensional materials beyond graphene,” *ACS Nano*, vol. 9, no. 12, pp. 11 509–11 539, 2015.

[110] J. Luque-González, A. Sánchez-Postigo, A. Hadij-ElHouati, *et al.*, “A review of silicon subwavelength gratings: Building break-through devices with anisotropic metamaterials,” *Nanophotonics*, vol. 10, no. 11, 2021.

[111] Y Park, U. Kim, S Lee, *et al.*, “On-chip raman spectrometers using narrow band filter array combined with cmos image sensors,” *Sensors and Actuators B: Chemical*, vol. 381, 2023.

[112] C. Chang and H. Lee, “On the estimation of target spectrum for filter-array based spectrometers,” *Optics Express*, vol. 16, no. 2, p. 1056, 2008.

[113] S Keuleyan, E Lhuillier, and P Guyot-Sionnest, “Synthesis of colloidal hgte quantum dots for narrow mid-ir emission and detection,” *Journal of the American Chemical Society*, vol. 133, no. 41, pp. 16 422–16 424, 2011.

[114] X Gong, M Tong, Y Xia, *et al.*, “High-detectivity polymer photodetectors with spectral response from 300 nm to 1450 nm,” *Science*, vol. 325, no. 5948, pp. 1665–1667, 2009.

[115] E Saracco, B Bouthinon, J Verilhac, *et al.*, “Work function tuning for high-performance solution-processed organic photodetectors with inverted structure,” *Advanced Materials*, vol. 25, no. 45, pp. 6534–6538, 2013.

[116] F Guo, Z Xiao, and J Huang, “Fullerene photodetectors with a linear dynamic range of 90 db enabled by a cross-linkable buffer layer,” *Advanced Optical Materials*, vol. 1, no. 4, pp. 289–294, 2013.

[117] A Armin, M Hambsch, I. Kim, P. Burn, P Meredith, and E. Namdas, “Thick junction broadband organic photodiodes,” *Laser & Photonics Reviews*, vol. 8, no. 6, pp. 924–932, 2014.

[118] A Pierre, I Deckman, P. Lechêne, and A. Arias, “High detectivity all-printed organic photodiodes,” *Advanced Materials*, vol. 27, no. 41, pp. 6411–6417, 2015.

[119] X Zhou, D Yang, and D Ma, “Extremely low dark current, high responsivity, all-polymer photodetectors with spectral response from 300 nm to 1000 nm,” *Advanced Optical Materials*, vol. 3, no. 11, pp. 1570–1576, 2015.

[120] H Zhang, S Jenatsch, J De Jonghe, *et al.*, “Transparent organic photodetector using a near-infrared absorbing cyanine dye,” *Scientific Reports*, vol. 5, p. 1, 2015.

[121] M Kielar, O Dhez, G Pecastaings, A Curutchet, and L Hirsch, “Long-term stable organic photodetectors with ultra low dark currents for high detectivity applications,” *Scientific Reports*, vol. 6, p. 1, 2016.

[122] L Shen, Y Fang, H Wei, Y Yuan, and J Huang, “A highly sensitive narrowband nanocomposite photodetector with gain,” *Advanced Materials*, vol. 28, no. 10, pp. 2043–2048, 2016.

[123] W Wang, F Zhang, M Du, *et al.*, “Highly narrowband photomultiplication type organic photodetectors,” *Nano Letters*, vol. 17, no. 3, pp. 1995–2002, 2017.

[124] Z Tang, Z Ma, A Sánchez-Díaz, *et al.*, "Polymer:fullerene bimolecular crystals for near-infrared spectroscopic photodetectors," *Advanced Materials*, vol. 29, no. 33, 2017.

[125] B Siegmund, A Mischok, J Benduhn, *et al.*, "Organic narrowband near-infrared photodetectors based on intermolecular charge-transfer absorption," *Nature Communications*, vol. 8, no. 1, 2017.

[126] Y Wei, Z Ren, A Zhang, *et al.*, "Hybrid organic/pbs quantum dot bilayer photodetector with low dark current and high detectivity," *Advanced Functional Materials*, vol. 28, no. 11, 2018.

[127] L Xiao, S Chen, X Chen, X Peng, Y Cao, and X Zhu, "High-detectivity panchromatic photodetectors for the near infrared region based on a dimeric porphyrin small molecule," *Journal of Materials Chemistry C*, vol. 6, no. 13, pp. 3341–3345, 2018.

[128] W Wang, M Du, M Zhang, J Miao, Y Fang, and F Zhang, "Organic photodetectors with gain and broadband/narrowband response under top/bottom illumination conditions," *Advanced Optical Materials*, vol. 6, no. 16, 2018.

[129] X Zhang, E Zheng, M. Esopi, C Cai, and Q Yu, "Flexible narrowband ultraviolet photodetectors with photomultiplication based on wide band gap conjugated polymer and inorganic nanoparticles," *ACS Applied Materials & Interfaces*, vol. 10, no. 28, pp. 24 064–24 074, 2018.

[130] Z Zhong, K Li, J Zhang, *et al.*, "High-performance all-polymer photodetectors via a thick photoactive layer strategy," *ACS Applied Materials & Interfaces*, vol. 11, no. 15, pp. 14 208–14 214, 2019.

[131] A Liess, A Arjona-Esteban, A Kudzus, *et al.*, "Ultranarrow bandwidth organic photodiodes by exchange narrowing in merocyanine h- and j-aggregate excitonic systems," *Advanced Functional Materials*, vol. 29, no. 21, 2018.

[132] J. Wang, S. Ullbrich, J. Hou, *et al.*, "Organic cavity photodetectors based on nanometer-thick active layers for tunable monochromatic spectral response," *ACS Photonics*, vol. 6, no. 6, pp. 1393–1399, 2019.

[133] C Kaiser, K. Schellhammer, J Benduhn, *et al.*, "Manipulating the charge transfer absorption for narrowband light detection in the near-infrared," *Chemistry of Materials*, vol. 31, no. 22, pp. 9325–9330, 2019.

[134] C Lee, R Estrada, Y Li, *et al.*, "Vacuum-processed small molecule organic photodetectors with low dark current density and strong response to near-infrared wavelength," *Advanced Optical Materials*, vol. 8, no. 17, 2020.

[135] S Xing, X Wang, E Guo, H Kleemann, and K Leo, "Organic thin-film red-light photodiodes with tunable spectral response via selective exciton activation," *ACS Applied Materials & Interfaces*, vol. 12, no. 11, pp. 13 061–13 067, 2020.

[136] B Xie, R Xie, K Zhang, *et al.*, "Self-filtering narrowband high performance organic photodetectors enabled by manipulating localized frenkel exciton dissociation," *Nature Communications*, vol. 11, no. 1, 2020.

[137] Z Lan, Y. Lau, Y Wang, *et al.*, "Filter-free band-selective organic photodetectors," *Advanced Optical Materials*, vol. 8, no. 24, 2020.

[138] Y Wang, B Siegmund, Z Tang, *et al.*, "Stacked dual-wavelength near-infrared organic photodetectors," *Advanced Optical Materials*, vol. 9, no. 6, 2020.

[139] Z Huang, Z Zhong, F Peng, *et al.*, "Copper thiocyanate as an anode interfacial layer for efficient near-infrared organic photodetector," *ACS Applied Materials & Interfaces*, vol. 13, no. 1, pp. 1027–1034, 2020.

[140] M Liu, J Wang, Z Zhao, *et al.*, "Ultra-narrow-band nir photomultiplication organic photodetectors based on charge injection narrowing," *The Journal of Physical Chemistry Letters*, vol. 12, no. 11, pp. 2937–2943, 2021.

[141] J Yang, J Huang, R Li, *et al.*, "Cavity-enhanced near-infrared organic photodetectors based on a conjugated polymer containing [1,2,5]selenadiazolo[3,4-c]pyridine," *Chemistry of Materials*, vol. 33, no. 13, pp. 5147–5155, 2021.

[142] J Kublitski, A Fischer, S Xing, *et al.*, "Enhancing sub-bandgap external quantum efficiency by photomultiplication for narrowband organic near-infrared photodetectors," *Nature Communications*, vol. 12, no. 1, 2021.

[143] Z Deng, K. Jeong, and P Guyot-Sionnest, "Colloidal quantum dots intraband photodetectors," *ACS Nano*, vol. 8, no. 11, pp. 11 707–11 714, 2014.

[144] J Kim, S. Kwon, Y. Kang, *et al.*, "A skin-like two-dimensionally pixelized full-color quantum dot photodetector," *Science Advances*, vol. 5, no. 11, 2019.

[145] I Ramiro, O Özdemir, S Christodoulou, *et al.*, "Mid- and long-wave infrared optoelectronics via intraband transitions in pbs colloidal quantum dots," *Nano Letters*, vol. 20, no. 2, pp. 1003–1008, 2020.

[146] J. Jimenez, L. Fonseca, D. Brady, J. Leburton, D. Wohlert, and K. Cheng, "The quantum dot spectrometer," *Applied Physics Letters*, vol. 71, no. 24, pp. 3558–3560, 1997.

[147] X Zhu, L Bian, H Fu, *et al.*, "Broadband perovskite quantum dot spectrometer beyond human visual resolution," *Light: Science & Applications*, vol. 9, p. 73, 2020.

[148] B Zheng, J. Wang, T Huang, X Su, Y Shi, and X Wang, "Single-detector black phosphorus monolithic spectrometer with high spectral and temporal resolution," *Applied Physics Letters*, vol. 120, no. 25, p. 251 102, 2022.

[149] J Zheng, Y Xiao, M Hu, *et al.*, "Photon counting reconstructive spectrometer combining metasurfaces and superconducting nanowire single-photon detectors," *Photonics Research*, vol. 11, pp. 234–244, 2023.

[150] P Cheben, J. Schmid, A Delâge, *et al.*, "A high-resolution silicon-on-insulator arrayed waveguide grating microspectrometer with sub-micrometer aperture waveguides," *Optics Express*, vol. 15, pp. 2299–2306, 2007.

[151] Z Xia, A Asghar Eftekhar, M Soltani, *et al.*, "High resolution on-chip spectroscopy based on miniaturized microdonut resonators," *Optics Express*, vol. 19, pp. 12 356–12 364, 2011.

[152] L Zhang, M Zhang, T. Chen, D. Liu, S. Hong, *et al.*, "Ultrahigh-resolution on-chip spectrometer with silicon photonic resonators," *Opto-Electronic Advances*, vol. 5, p. 210 100, 2022.

[153] A. Velasco, B Cheben, P. Bock, *et al.*, "High-resolution fourier-transform spectrometer chip with microphotonic silicon spiral waveguides," *Optics Letters*, vol. 38, pp. 706–708, 2013.

[154] J Loridat *et al.*, "All integrated lithium niobate standing wave fourier transform electro-optic spectrometer," *Journal of Lightwave Technology*, vol. 36, no. 20, pp. 4900–4907, 2018.

[155] X Kang, J Li, S Yang, H Chen, and M Chen, "High-performance on-chip spectrometer based on micro-rings resonator," in *Proc. SPIE 11608, Optics Frontiers Online 2020: Micro and Nanophotonics (OFO-4 2020)*, 2020, p. 1 160 808.

[156] D. Kita, B Miranda, D Favela, *et al.*, "High-performance and scalable on-chip digital fourier transform spectroscopy," *Nature Communications*, vol. 9, p. 4405, 2018.

[157] Z. Zheng, S. Zhu, Y Chen, H. Chen, and J. Chen, "Towards integrated mode-division demultiplexing spectrometer by deep learning," *Opto-Electronic Science*, vol. 1, p. 220 012, 2022.

[158] C Chen, X Li, G Yang, *et al.*, "Computational hyperspectral devices based on quasi-random metasurface supercells," *Nanoscale*, vol. 15, pp. 8854–8862, 2023.

[159] J Brouckaert, W Bogaerts, P Dumon, D Van Thourhout, and R Baets, "Planar concave grating demultiplexer fabricated on a nanophotonic silicon-on-insulator platform," *Journal of Lightwave Technology*, vol. 25, no. 5, pp. 1269–1275, 2007.

[160] P Pottier, M. Strain, and M Packirisamy, "Integrated microspectrometer with elliptical bragg mirror enhanced diffraction grating on silicon on insulator," *ACS Photonics*, vol. 1, no. 5, pp. 430–436, 2014.

[161] B Momeni *et al.*, "An on-chip silicon grating spectrometer using a photonic crystal reflector," *Journal of Optics*, vol. 12, p. 035 501, 2010.

[162] M Muneeb, X Chen, P Verheyen, *et al.*, "Demonstration of silicon-on-insulator mid-infrared spectrometers operating at 3.8μm," *Optics Express*, vol. 21, no. 10, pp. 11 659–11 669, 2013.

[163] J Brouckaert, W Bogaerts, S Selvaraja, P Dumon, R Baets, and D Van Thourhout, "Planar concave grating demultiplexer with high reflective bragg reflector facets," *IEEE Photonics Technology Letters*, vol. 20, no. 4, pp. 309–311, 2008.

[164] R. A. Soref, F. De Leonardis, and V. M. N. Passaro, "Scanning spectrometer-on-a-chip using thermo-optical spike-filters or vernier-comb filters," *Journal of Lightwave Technology*, vol. 37, no. 13, pp. 3192–3200, 2019. DOI: `10.1109/JLT.2019.2912725`.

[165] Z. Lin, H. Wang, S. Bélanger-de Villers, Q. Li, and W. Shi, "Silicon channeled spectropolarimeter for on-chip single-detector stokes spectroscopy," *Advanced Photonics Research*, vol. 3, no. 2, p. 2 100 212, 2022. DOI: `https://doi.org/10.1002/adpr.202100212`. eprint: `https://advanced.onlinelibrary.wiley.com/doi/pdf/10.1002/adpr.202100212`. [Online]. Available: `https://advanced.onlinelibrary.wiley.com/doi/abs/10.1002/adpr.202100212`.

[166] Z. Gong, F. Yang, L. Wang, *et al.*, "Phase change materials in photonic devices," *Journal of Applied Physics*, vol. 129, no. 3, p. 030 902, Jan. 2021, ISSN: 0021-8979. DOI: `10.1063/5.0027868`. eprint: `https://pubs.aip.org/aip/jap/article-pdf/doi/10.1063/5.0027868/20018317/030902\_1\_5.0027868.pdf`. [Online]. Available: `https://doi.org/10.1063/5.0027868`.

[167] P. Prabhathan, K. V. Sreekanth, J. Teng, *et al.*, "Roadmap for phase change materials in photonics and beyond," *iScience*, vol. 26, no. 10, 2023, ISSN: 2589-0042. DOI: `10.1016/j.isci.2023.107946`. [Online]. Available: `https://doi.org/10.1016/j.isci.2023.107946`.

[168] S. Abdollahramezani, O. Hemmatyar, H. Taghinejad, *et al.*, "Tunable nanophotonics enabled by chalcogenide phase-change materials," *Nanophotonics*, vol. 9, no. 5, pp. 1189–1241, 2020. DOI: `10.1515/nanoph-2020-0039`. [Online]. Available: `https://doi.org/10.1515/nanoph-2020-0039`.

[169] Y. Gutiérrez, A. P. Ovvyan, G. Santos, *et al.*, "Interlaboratory study on sb2s3 interplay between structure, dielectric function, and amorphous-to-crystalline phase change for photonics," *iScience*, vol. 25, no. 6, p. 104 377, 2022, ISSN: 2589-0042. DOI: `10.1016/j.isci.2022.104377`. [Online]. Available: `https://www.sciencedirect.com/science/article/pii/S2589004222006484`.

[170] Z. Cui, K. Bu, Y. Zhuang, *et al.*, "Phase transition mechanism and bandgap engineering of sb2s3 at gigapascal pressures," *Communications Chemistry*, vol. 4, no. 1, p. 125, 2021, ISSN: 2399-3669. DOI: `10.1038/s42004-021-00565-4`. [Online]. Available: `https://doi.org/10.1038/s42004-021-00565-4`.

[171] T. Ben Nasr, H. Maghraoui-Meherzi, H. Ben Abdallah, and R. Bennaceur, "Electronic structure and optical properties of sb2s3 crystal," *Physica B: Condensed Matter*, vol. 406, no. 2, pp. 287–292, 2011, ISSN: 0921-4526. DOI: `10.1016/j.physb.2010.10.026`. [Online]. Available: `https://www.sciencedirect.com/science/article/pii/S0921452610010264`.

[172] M. Grado-Caffaro and M. Grado-Caffaro, "A theorem on refractive index as a function of wavelength," *Optik*, vol. 122, no. 7, pp. 652–653, 2011, ISSN: 0030-4026. DOI: `10.1016/j.ijleo.2010.03.021`. [Online]. Available: `https://www.sciencedirect.com/science/article/pii/S0030402610001671`.

[173] Ansys Lumerical - Optics, *Lumerical inc.* DOI: `NO-DOI-AVAILABLE`. [Online]. Available: `https://optics.ansys.com/hc/en-us`.

[174] A. D. Gomes, H. Bartelt, and O. Frazao, "Optical vernier effect: Recent advances and developments," *Laser & Photonics Reviews*, vol. 15, no. 7, p. 2 000 588, 2021. DOI: `10.1002/lpor.202000588`. eprint: `https://onlinelibrary.wiley.com/doi/pdf/10.1002/lpor.202000588`. [Online]. Available: `https://onlinelibrary.wiley.com/doi/abs/10.1002/lpor.202000588`.

[175] T. Claes, W. Bogaerts, and P. Bienstman, "Experimental characterization of a silicon photonic biosensor consisting of two cascaded ring resonators based on the vernier-effect and introduction of a curve fitting method for an improved detection limit," *Opt. Express*, vol. 18, no. 22, pp. 22 747–22 761, 2010. DOI: `10.1364/OE.18.022747`. [Online]. Available: `https://opg.optica.org/oe/abstract.cfm?URI=oe-18-22-22747`.

[176] V. M. Passaro, B. Troia, and F. De Leonardis, "A generalized approach for design of photonic gas sensors based on vernier-effect in mid-ir," *Sensors and Actuators B: Chemical*, vol. 168, pp. 402–420, 2012, ISSN: 0925-4005. DOI: `10.1016/j.snb.2012.04.044`. [Online]. Available: `https://www.sciencedirect.com/science/article/pii/S0925400512003930`.

[177] M.-J. Ye, R. G. Bikbaev, P. S. Pankin, *et al.*, "Lossless phase change materials for adjustable tamm plasmon polaritons in the near-infrared," *Advanced Optical Materials*, vol. 13, no. 9, p. 2 402 889, 2025. DOI: `https://doi.org/10.1002/adom.202402889`. eprint: `https://advanced.onlinelibrary.wiley.com/doi/pdf/10.1002/adom.202402889`. [Online]. Available: `https://advanced.onlinelibrary.wiley.com/doi/abs/10.1002/adom.202402889`.

[178] W. Bogaerts, P. De Heyn, T. Van Vaerenbergh, *et al.*, "Silicon microring resonators," *Laser & Photonics Reviews*, vol. 6, no. 1, pp. 47–73, 2012. DOI: `10.1002/lpor.201100017`. eprint: `https://onlinelibrary.wiley.com/doi/pdf/10.1002/lpor.201100017`. [Online]. Available: `https://onlinelibrary.wiley.com/doi/abs/10.1002/lpor.201100017`.

[179] A. Fathy, Y. M. Sabry, S. Nazeer, T. Bourouina, and D. Khalil, "On-chip parallel fourier transform spectrometer for broadband selective infrared spectral sensing," *Microsystems & Nanoengineering*, vol. 6, p. 3, 2020. DOI: `10.1038/s41378-019-0111-0`.

[180] B. I. Akca, "Design of a compact and ultrahigh-resolution fourier-transform spectrometer," *Optics Express*, vol. 25, no. 2, pp. 1487–1494, 2017. DOI: `10.1364/OE.25.001487`.

[181] J. Shen, D. Donnelly, A. Perera, and S. Chakravarty, "Phase-change-material integrated, phase-error corrected, resolution-enhanced michelson interferometer fourier transform spectrometer," in *CLEO: Science and Innovations 2024, Technical Digest*, Optica Publishing Group, 2024, SF2A.6. DOI: `10.1364/CLEO_SI.2024.STh4H.8`.

[182] D. M. Kita, H. Lin, A. Agarwal, *et al.*, "On-chip infrared spectroscopic sensing: Redefining the benefits of scaling," *IEEE Journal of Selected Topics in Quantum Electronics*, vol. 23, no. 2, pp. 340–349, 2017. DOI: `10.1109/JSTQE.2016.2631139`.

[183] M. Harwit and N. J. Sloane, "Chapter 4 - noise or when to multiplex and when to avoid it," in *Hadamard Transform Optics*, M. Harwit and N. J. Sloane, Eds., Academic Press, 1979, pp. 96–108, ISBN: 978-0-12-330050-8. DOI: `10.1016/B978-0-12-328560-1.50010-6`. [Online]. Available: `https://www.sciencedirect.com/science/article/pii/B9780123300508500081`.

[184] O. Bryngdahl, "Image formation using self-imaging techniques∗," *J. Opt. Soc. Am.*, vol. 63, no. 4, pp. 416–419, 1973. DOI: `10.1364/JOSA.63.000416`. [Online]. Available: `https://opg.optica.org/abstract.cfm?URI=josa-63-4-416`.

[185] L. Soldano and E. Pennings, "Optical multi-mode interference devices based on self-imaging: Principles and applications," *Journal of Lightwave Technology*, vol. 13, no. 4, pp. 615–627, 1995. DOI: `10.1109/50.372474`.

[186] L. Chrostowski and M. Hochberg, *Silicon photonics design: from devices to systems.* Cambridge University Press, 2015.

[187] G. Son, S. Han, J. Park, K. Kwon, and K. Yu, "High-efficiency broadband light coupling between optical fibers and photonic integrated circuits," *Nanophotonics*, vol. 7, no. 12, pp. 1845–1864, 2018. DOI: `10.1515/nanoph-2018-0075`. [Online]. Available: `https://doi.org/10.1515/nanoph-2018-0075`.

[188] K. Wang, Z. She, H. Tan, T. Zhang, and L. Zhang, "Integrated computational spectrometer with 40 pm resolution using tunable micro-ring resonators," *Chinese Optics Letters*, vol. 24, no. 11, p. 011 301, Jan. 2026. [Online]. Available: `https://www.researching.cn/articles/OJ5b489d08715ec196`.

[189] X. Liu, H. Jia, Y. Yu, and S. Yang, "A compact on-chip computational spectrometer using reconfigurable silicon micro-ring optical filtering network," *Optics Communications*, vol. 592, p. 132 227, 2025, ISSN: 0030-4018. DOI: `https://doi.org/10.1016/j.optcom.2025.132227`. [Online]. Available: `https://www.sciencedirect.com/science/article/pii/S0030401825007552`.

[190] C. Yao, W. Zhang, P. Bao, *et al.*, "Chip-scale sensor for spectroscopic metrology," *Nature Communications*, vol. 15, no. 1, p. 10 305, 2024, ISSN: 2041-1723. DOI: `10.1038/s41467-024-54708-x`. [Online]. Available: `https://doi.org/10.1038/s41467-024-54708-x`.

[191] Z. Zhang, B. Huang, Z. Zhang, and H. Chen, "On-chip reconstructive spectrometer based on parallel cascaded micro-ring resonators," *Applied Sciences*, vol. 14, no. 11, 2024, ISSN: 2076-3417. DOI: `10.3390/app14114886`. [Online]. Available: `https://www.mdpi.com/2076-3417/14/11/4886`.

[192] C. M. Coppola, M. De Carlo, F. De Leonardis, and V. M. N. Passaro, "High-resolution on-chip digitally tunable spectrometer based on double-cascaded ring resonators," *Advanced Photonics Research*, vol. 6, no. 9, p. 2 500 021, 2025. DOI: `https://doi.org/10.1002/adpr.202500021`. eprint: `https://advanced.onlinelibrary.wiley.com/doi/pdf/10.1002/adpr.202500021`. [Online]. Available: `https://advanced.onlinelibrary.wiley.com/doi/abs/10.1002/adpr.202500021`.

[193] Q. Xue, Y. Yang, W. Ma, *et al.*, "Advances in miniaturized computational spectrometers," *Advanced Science*, vol. 11, no. 47, p. 2 404 448, 2024. DOI: `10.1002/advs.202404448`. eprint: `https://advanced.onlinelibrary.wiley.com/doi/pdf/10.1002/advs.202404448`. [Online]. Available: `https://advanced.onlinelibrary.wiley.com/doi/abs/10.1002/advs.202404448`.

[194] U. Kurokawa, B. I. Choi, and C.-C. Chang, "Filter-based miniature spectrometers: Spectrum reconstruction using adaptive regularization," *IEEE Sensors Journal*, vol. 11, no. 7, pp. 1556–1563, 2011. DOI: `10.1109/JSEN.2010.2103054`.

[195] R. Tibshirani, "Regression shrinkage and selection via the lasso," *Journal of the Royal Statistical Society. Series B (Methodological)*, vol. 58, no. 1, pp. 267–288, 1996, ISSN: 00359246. DOI: `10.1111/j.2517-6161.1996.tb02080.x`. [Online]. Available: `http://www.jstor.org/stable/2346178` (visited on 05/05/2025).

[196] E. J. Candes and M. B. Wakin, "An introduction to compressive sampling," *IEEE Signal Processing Magazine*, vol. 25, no. 2, pp. 21–30, 2008. DOI: `10.1109/MSP.2007.914731`.

[197] G. R. Arce, D. J. Brady, L. Carin, H. Arguello, and D. S. Kittle, "Compressive coded aperture spectral imaging: An introduction," *IEEE Signal Processing Magazine*, vol. 31, no. 1, pp. 105–115, 2014. DOI: `10.1109/MSP.2013.2278763`.

[198] T. T. Georgiou, M. Lipson, and A. P. Tzannes, "Optimal filter sets for integrated spectrometers," *IEEE Transactions on Signal Processing*, vol. 69, pp. 5047–5056, 2021. DOI: `10.1109/TSP.2021.3103872`.

[199] L. Shao, X. Wang, T. Liu, *et al.*, "Recent progress in computational spectrometers: A review," *Frontiers of Optoelectronics*, vol. 15, pp. 1–29, 2022. DOI: `10.1007/s12200-022-00036-w`.

[200] E. J. Candès, J. Romberg, and T. Tao, "Robust uncertainty principles: Exact signal reconstruction from highly incomplete frequency information," *IEEE Transactions on Information Theory*, vol. 52, no. 2, pp. 489–509, 2006. DOI: `10.1109/TIT.2005.862083`.

[201] A. Mahalanobis, B. V. K. V. Kumar, S. Song, S. R. F. Sims, and J. F. Epperson, "Unconstrained correlation filters," *Appl. Opt.*, vol. 33, no. 17, pp. 3751–3759, 1994. DOI: `10.1364/AO.33.003751`. [Online]. Available: `https://opg.optica.org/ao/abstract.cfm?URI=ao-33-17-3751`.

[202] M. Pasha, S. Gazzola, C. Sanderford, and U. O. Ugwu, "Trips-py: Techniques for regularization of inverse problems in python," *Numerical Algorithms*, vol. 99, no. 1, pp. 285–322, 2025, ISSN: 1572-9265. DOI: `10.1007/s11075-024-01878-w`. [Online]. Available: `https://doi.org/10.1007/s11075-024-01878-w`.

[203] G. Grynberg, A. Aspect, and C. Fabre, *Introduction to Quantum Optics: From the Semi-classical Approach to Quantized Light*. Cambridge University Press, 2010. DOI: `10.1017/CBO9780511778261`.

[204] C. H. Bennett and G. Brassard, "Quantum cryptography: Public key distribution and coin tossing," *Theoretical Computer Science*, vol. 560, pp. 7–11, 2014, ISSN: 0304-3975. DOI: `10.1016/j.tcs.2014.05.025`. [Online]. Available: `http://dx.doi.org/10.1016/j.tcs.2014.05.025`.

[205] A. K. Ekert, "Quantum cryptography based on bell's theorem," *Phys. Rev. Lett.*, vol. 67, pp. 661–663, 6 1991. DOI: `10.1103/PhysRevLett.67.661`. [Online]. Available: `https://link.aps.org/doi/10.1103/PhysRevLett.67.661`.

[206] I. E. Zadeh *et al.*, “Superconducting nanowire single-photon detectors: A perspective on evolution, state-of-the-art, future developments, and applications,” *Applied Physics Letters*, 2021.

[207] N. J. D. Martinez *et al.*, “Single photon detection in a waveguide-coupled ge-on-si single-photon avalanche diode,” *Optics Express*, 2017.

[208] N. Na, C.-Y. Hsu, E. Chen, and R. Soref, “Room-temperature photonic quantum computing in integrated silicon photonics with germanium-silicon single-photon avalanche diodes,” *arXiv preprint arXiv:2405.04763*, 2024.